Selective reflection spectroscopy of alkali vapors confined in nanocells and emerging sensing applications

Emmanuel Klinger

UNIVERSITÉ BOURGOGNE FRANCHE-COMTÉ
Laboratoire Interdisciplinaire Carnot de Bourgogne – UMR CNRS 6303

NATIONAL ACADEMY OF SCIENCES OF ARMENIA
Institute for Physical Research

SELECTIVE REFLECTION SPECTROSCOPY OF ALKALI VAPORS CONFINED IN NANOCELLS AND EMERGING SENSING APPLICATIONS

by

Emmanuel Klinger

A Thesis in Physics
Submitted for the Degree of Doctor of Philosophy

Date of defense: September 18 2019

Jury

Mr Dmitry Budker	Professor Mainz, HIM – JGU	Referee
Mr Emilio Mariotti	Professor Siena, US	Referee
Mr Claude Leroy	Professor Dijon, ICB – UBFC	Supervisor
Mr Aram Papoyan	Professor, Director of IPR Ashtarak, IPR – NAS	Supervisor
Mrs Yevgenyan Pashayan-Leroy	Doctor of Physics Besançon, UBFC	Examiner
Mr Tigran Vartanyan	Professor St. Petersburg, ITMO	Examiner
Mr David Sarkisyan	Professor Ashtarak, IPR – NAS	Examiner - Président du Jury

Laboratoire Interdisciplinaire Carnot de Bourgogne – UMR CNRS 6303, Université Bourgogne Franche-Comté, 9 Avenue A. Savary 21078 Dijon, France

Institute for Physical Research – National Academy of Sciences of Armenia, 0203 Ashtarak-2, Armenia

Acknowledgments

My deepest gratitude goes to my thesis supervisors, Profs. Claude Leroy and Aram Papoyan without who this thesis would not have been possible. I am thankful to them for their pedagogy, patience and moral support whether related to science of personal life throughout these last three years; and of course, for sharing their wine tasting experience!

I cannot forget Prof. David Sarkisyan and Dr. Armen Sargsyan who manufacture the best cells in the world. I am particularly thankful for their nanocells which are the core of this thesis experimental work. I thank them for sharing their knowledge and allowing me to perform my own designed experiments with nanocells. I also thank Dr. Hrayr Azizbekyan for his precious help and time in the development of the magnetometer driving programs. For his patience and trust, I thank Dr. Kamal Hammani who was supporting me for my first teaching experience.

This thesis work main financial support came from the Centre National de la Recherche Scientifique which I heavily thank. I would also like to acknowledge financial supports from the Foundation for Armenian Science and Technology (FAST, travel grant for collaborative research), from Ecole Doctoral Carnot Pasteur and Laboratoire Interdisciplinaire Carnot de Bourgogne – CNRS which have founded most of my participations to international conferences. Part of the work presented in this thesis was conducted in the scope of the International Associated Laboratory IRMAS (CNRS France & SCS Armenia).

Finally, I am thankful to my family for all kind of support and encouragements they have provided me during my PhD studies. Particularly, I am deeply thankful to Armine, Hasmik, Azniv, Arevik and our son Jean for their precious help and lovely support before and during the thesis writing process.

Abstract

Selective Reflection Spectroscopy of Alkali Vapors Confined in Nanocells and Emerging Sensing Applications

This thesis is aimed at studying the resonant interaction of a laser radiation with an atomic alkali vapor layer of wavelength-scale thickness confined in an optical nanocell; and emerging sensing applications.

We focus our attention on the selective reflection arising at the interface between a dielectric window and a resonant alkali vapor, and show that the derivative of selective reflection spectra exhibit narrow resonances whose maxima are located exactly at atomic resonance frequencies. These resonances are observed with a spectral linewidth up to fifteen times smaller than the Doppler linewidth of the medium and their amplitudes scale linearly with respect to the transitions ones. Owing to these properties and the possibility to probe thin atomic layers, we investigate atom-surface interaction and measure the C_3 coefficient of the van der Waals interaction.

We present a theoretical model describing the interaction of near-resonant laser light with alkali vapor-filled nanocell in the presence of an external static magnetic field. We show an excellent agreement between recorded and calculated spectra in a wide range of magnetic fields spanning from Zeeman to Paschen-Back regimes. Following these results, we propose a concept for a nanocell-based optical magnetometer. A proof of feasibility is presented and a performance analysis reveals a coefficient of variation for the magnetic field measurements less than 5% in the range 0.4 – 2 kG.

Résumé

Spectroscopie par Réflexion Sélective de Vapeurs Alcalines Confinées dans des Nanocellules et Applications de Détection Émergentes

Cette thèse vise à étudier l'interaction résonante d'un rayonnement laser avec une couche mince d'épaisseur sub-longueur d'onde de vapeur alcaline atomique confinée en nanocellule ; et les applications de détection qui en émergent.

Nous nous concentrons sur la réflexion sélective se produisant à l'interface entre une fenêtre diélectrique et une vapeur résonante, et montrons que la dérivée des spectres de réflexion sélective est composée de résonances étroites dont les maximua correspondent aux positions des transitions atomiques. Ces résonances sont observées avec une largeur spectrale jusqu'à quinze fois plus fine que la largeur Doppler du milieu, et leurs amplitudes évoluent de façon linéaire avec celles des transitions. Grâce à ces propriétés et aux faibles épaisseurs de cellule pouvant être sondées, nous examinons les interactions atome-surface et mesurons le coefficient C_3 de l'interaction de van der Waals.

Nous présentons un modèle théorique décrivant l'interaction entre lumière quasi-résonante et nanocellule remplie d'une vapeur alcaline sous champ magnétique statique. Ce modèle se montre en excellent accord avec les résultats expérimentaux pour une large gamme de champs magnétiques depuis le régime Zeeman jusqu'au régime Paschen-Back. Au vu de ces résultats, nous proposons un concept de magnétomètre optique basé sur les nanocellules. Une preuve de faisabilité est présentée et une analyse en performance révèle un coefficient de variation des mesures de champs magnétiques inférieur à 5 % dans la gamme 0,4 – 2 kG.

Contents

List of Figures

Chapter 1

General Introduction

Contents

Introduction

The creation of the first laser by T.H. Maiman in 1960 [1] has open the door to new fields of physics and applications. Indeed, this new source of coherent light has not only enabled the development of numerous applications in diverse areas such as industry, engineering, medicine or telecommunications but also stimulated various field of research, particularly spectroscopy allowing to shed light on light-matter interaction, pushing much further our knowledge on atomic and molecular structure.

In the past decades, laser spectroscopy of atoms has established as the core of high precision measurements [2], finding a large variety of applications ranging from testing of the fundamental symmetries of nature to the detection of magnetic field from the heart and the brain. Resonant interactions of laser radiation with atomic vapor have been used for development of optical insulators [3], narrow-band optical filters [4], stabilization of laser radiation frequency [5], determination of fundamental constants [6], etc. Among the important applications emerging from atomic spectroscopy are atom-based sensing, which is now used in metrology (atomic clocks) [7], nuclear magnetic resonance gyroscopes, interferometers [8], and optical magnetometers [9]. Most of atomic sensors do not require cryogenic cooling, which is advantageous for integration in measurement systems and their miniaturization [10].

Atomic vapors of alkali metals (Li, Na, K, Rb, Cs, Fr) are widely used in various areas of physics due notably to their fairly simple electronic structure, after the hydrogen atom, composed by a single valence electron which allows one to perform extremely precise measurements and accurate theoretical predictions. They were for example used in the first experimental realizations of Bose-Einstein condensates in 1995 [11, 12]. Atomic clocks use Cs atoms to perform extremely precise and stable time measurements; which is the reason the second has been redefined by the International Committee for Weights and Measures in 1967 to a number of cycles of an hyperfine transition of ^{133}Cs ground state. Other applications of alkali atoms include investigations of Rydberg states [13, 14], dipole-dipole and cooperative interactions [15, 16, 17], atom-surface interactions [18], formation and studies of dimers [19, 20], investigations of non-linear reponse [21, 22], slow and fast light experiments [23, 24].

In this introductory chapter, we review particular properties of alkali vapors. We show that due to a large Doppler broadening, alkali D line hyperfine electronic transitions are partially masked under the Doppler profile. We thus make a non-exhaustive review of sub-Doppler spectroscopic techniques, addressing their advantages and drawbacks. We finish by presenting the motivation of the present thesis and giving an overview of the following chapters and appendices.

1.1 Thermal alkali vapors

Thermal alkali vapors (room temperature to several hundreds of Celsius degrees) have been the key core of a considerable number of atomic physics experiments over the past decades, especially noting their relatively cost-efficiency as compared with other techniques such as cold atom experiments or high energy physics. Investigation of transitions between the atomic states $n^2S_{1/2} \rightarrow n^2P_{1/2}$ (D_1 line) and $n^2S_{1/2} \rightarrow n^2P_{3/2}$ (D_2 line), are very convenient due *inter alia* to their strong optical transitions in a spectral region where a large variety of laser sources

exists. We list here-after some properties of alkali vapors and show that to perform precise laser spectroscopy of their hyperfine electronic transitions one has to implement a sub-Doppler technique.

1.1.1 Physical and optical properties

The behavior of alkali metal vapors at thermal equilibrium in the low-pressure limit can be approximated by the Ideal Gas Law, that is

$$P_v V = \mathcal{N} k_B \Theta, \tag{1.1}$$

where P_v is the vapor pressure in Torr (1 Torr = 133,322 Pa), V is the volume (m^3), n is the matter quantity (mol), Θ is the temperature (K), $\mathcal{N}$ is the number of atoms, and k_B is the Boltzmann constant. The vapor pressure inside the cell can be approximated by

$$\log_{10} P_v = a - \frac{b}{\Theta}, \tag{1.2}$$

with a and b constants depending on the atom and phase considered [25], see table 1.1 for values in the liquid phase. The number density for a given temperature can then be expressed as

$$N \equiv \frac{\mathcal{N}}{V} = \frac{P_v}{k_B \Theta}. \tag{1.3}$$

The evolution of the number density as a function of the temperature is shown in Fig. 1.1(a) in the case of K, Rb and Cs vapors.

Atoms move with a mean velocity $\bar{v} = \sqrt{8 k_B \Theta / \pi m_a}$ (m_a is the atomic mass in kg), typically about 270 m s^{-1} for Rb atoms at room temperature. Their motion leads to the well-known Doppler effect such that the incident laser frequency ω_L seen by the atom is $\omega = \omega_L - \mathbf{k} \cdot \mathbf{v}$ and atomic transition frequencies are shifted according to

$$\Delta_D = -\mathbf{k} \cdot \mathbf{v} = \mp k v_z \tag{1.4}$$

whether the atom move with a positive or negative velocity projection v_z on the propagation axis. In the previous relation, $\mathbf{k}$ is the wave vector of the incident monochromatic light propagating along the $+z$ direction. In a given atomic sample, atoms move with different velocity projections which follow, in one dimension, the Maxwell-Boltzmann distribution

$$M(v) = \frac{1}{u\sqrt{\pi}} \exp\left(-\frac{v^2}{u^2}\right), \tag{1.5}$$

where $u = \sqrt{2 k_B \Theta / m}$ is the most probable velocity. It results a (inhomogeneous) Doppler broadening of the transition line, whose linewidth is given by [26]

$$\Gamma_D = \omega_0 \sqrt{\frac{8 \ln(2) k_B \Theta}{m_a c^2}} \tag{1.6}$$

where $\omega_0 = 2\pi\nu_0$ is the central angular frequency of a given transition (Hz) and c is the speed of light (m s^{-1}). The evolution of the Doppler broadening as a function of the temperature is shown in Fig. 1.1(b). At room temperature, the Doppler broadening achieves 0.38, 0.6 and 0.78 GHz for the D_2 lines of Cs, Rb, and K respectively.

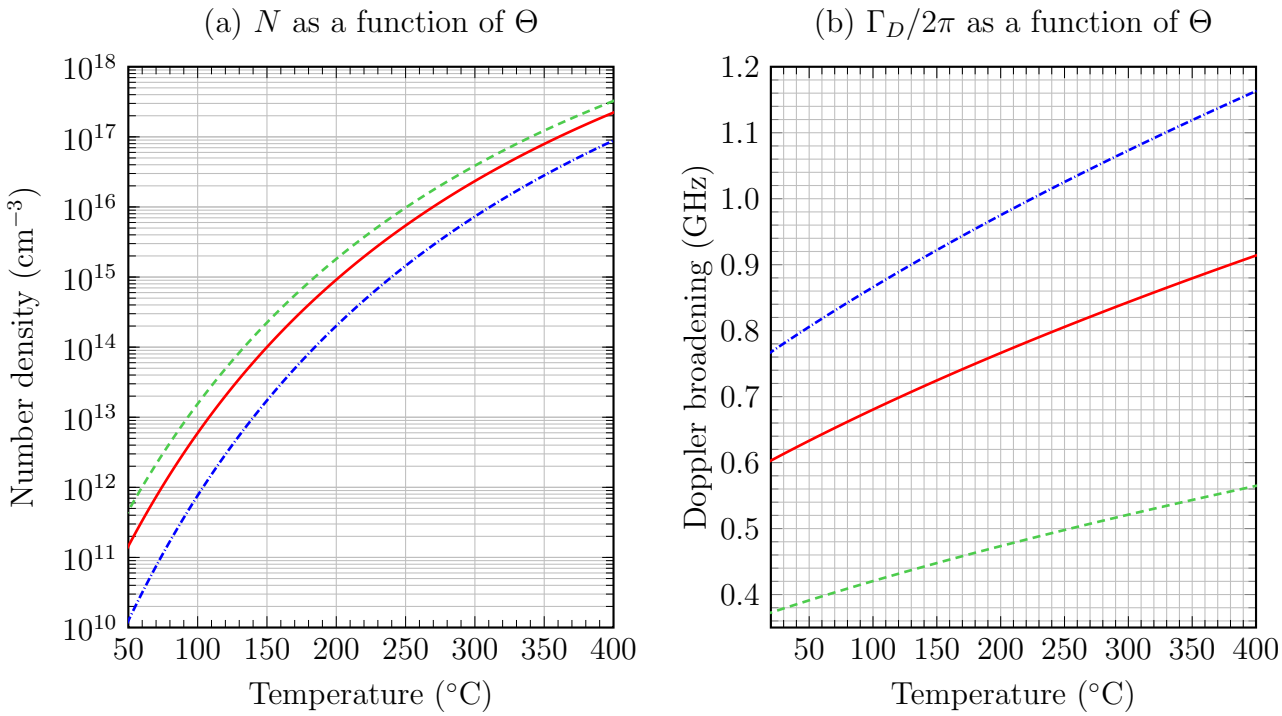

Figure 1.1: (a) Atomic number density N and (b) Doppler broadening Γ_D as function of the temperature Θ for ^{39}K (blue dash dotted lines), ^{85}Rb (red solid lines) and ^{133}Cs (green dashed lines) atoms. The Doppler broadening was calculated with the central frequency of the D_2 line.

1.1.2 Fine and hyperfine structure

The fine structure accounts for the total angular momentum **J** of the single valence electron. It results from the coupling of its orbital angular momentum **L** with its spin angular momentum **S**

$$\mathbf{J} = \mathbf{L} + \mathbf{S}, \tag{1.7}$$

where the total orbital momentum magnitude J can only take the values such that

$$|L - S| \leqslant J \leqslant L + S. \tag{1.8}$$

The coupling of the electron total angular momentum **J** with the total nuclear angular momentum spin **I** is responsible for the hyperfine structure, which is described by the total atomic angular momentum **F**

$$\mathbf{F} = \mathbf{J} + \mathbf{I}, \tag{1.9}$$

and, as before, the magnitude of **F** must lie in the range

$$|J - I| \leqslant F \leqslant J + I. \tag{1.10}$$

The coupling between **J** and **I** splits the fine energy levels according to [27]

$$\Delta E_{hf} = \frac{1}{2}A_{hf} + B_{hf}\frac{\frac{3}{2}K(K+1) - 2I(I+1)J(J+1)}{4I(2I-1)J(2J-1)}, \tag{1.11}$$

where A_{hf} is the magnetic dipole constant and B_{hf} is the electric quadrupole constant (applies only to excited manifold of the D_2 line transitions); in the previous equation, $K = F(F+1) - I(I-1) - J(J-1)$. For more details, see section 3.1.

In table 1.1 we have compiled hyperfine constants as well as other optical and physical constants of the main isotopes of K, Rb and Cs. Comparing the Doppler broadening (Fig 1.1(b)) with the states splittings given in table 1.1, one can see that, even at room temperature, the Doppler broadening exceeds the excited state splitting of Rb and is very close to that of Cs. For K vapor, the situation is even worse since the Doppler broadening exceed more than an order of magnitude the excited states splitting while being twice than that of the ground state one.

Entry	Symbol	^{39}K	^{85}Rb	^{133}Cs
Atomic number	Z	19	37	55
Principle quantum number	n	4	5	6
Nuclear spin	I	3/2	5/2	7/2
Atomic mass ($\times 10^{-25}$ kg)	m_a	0.647007	1.409993	2.206947
Isotopic abundance (%)	η	93.3	72.2	100
Melting point (°C)	Θ_m	63.7	39.3	28.5
Liquid phase first parameter	a	4.5267	4.312	4.165
Liquid phase second parameter (K^{-1})	b	4453	4040	3830
Magnetic dipole constant ($h \cdot$ GHz)	$A_{nS_{1/2}}$	0.2309	1.0119108	2.2981579425
Magnetic dipole constant ($h \cdot$ MHz)	$A_{nP_{1/2}}$	27.8	120.5	291.9
Magnetic dipole constant ($h \cdot$ MHz)	$A_{nP_{3/2}}$	6.1	25.0	50.3
Electric quadrupole constant ($h \cdot$ MHz)	$B_{nP_{3/2}}$	2.8	25.8	−0.49
Ground state splitting (GHz)	$\Delta_{nS_{1/2}}$	0.4617	3.0357	9.1926
D_1 line excited state splitting (MHz)	$\Delta_{nP_{1/2}}$	55.5	361.6	1167.7
D_2 line excited state splitting (MHz)	$\Delta_{nP_{3/2}}$	33.8	213.4	603.6

Table 1.1: Some physical and optical constants of the main isotopes of K, Rb and Cs atoms. These values have been extracted from [28, 29, 30], where more alkali data can be found. In the case of the D_2 line excited state manifold, the splitting given in this table corresponds to the difference of frequencies $\Delta\nu = (\Delta E_{hf}(F) - \Delta E_{hf}(F'))/h$ taken between the outermost states $|F\rangle$ and $|F'\rangle$, see Eq. (1.11).

To illustrate these statements, we have plotted in Fig 1.2 the Doppler-broadened (Gaussian profile) D_2 line spectra of ^{85}Rb (red dashdotted lines) and ^{133}Cs (green dashdotted lines) atoms

$$S_D(\omega) \propto \sum_i C_i \exp\left[-\frac{\omega - \omega_i}{0.6\Gamma_D}\right]^2, \tag{1.12}$$

where the summation is done on every hyperfine transition with an amplitude C_i and with a transition frequency $\omega_i/2\pi$ [2]; one can see strong broadening of the lines. As a comparison, we

also plotted the natural linewidth spectrum (in absence of motion, Lorentzian profile) given by

$$S_N(\omega) \propto \sum_i C_i \frac{\Gamma_N}{(\omega - \omega_i)^2 + (\pi\Gamma_N)^2}, \tag{1.13}$$

where $\Gamma_N \approx 5.7$, 4.5 MHz is the natural linewidth of ^{85}Rb and ^{133}Cs D_2 line transitions respectively [2]; which obviously shows that most hyperfine transitions are masked by the Doppler profile. Therefore, if one wants to study the hyperfine D line transitions independently, a sub-Doppler method must be implemented.

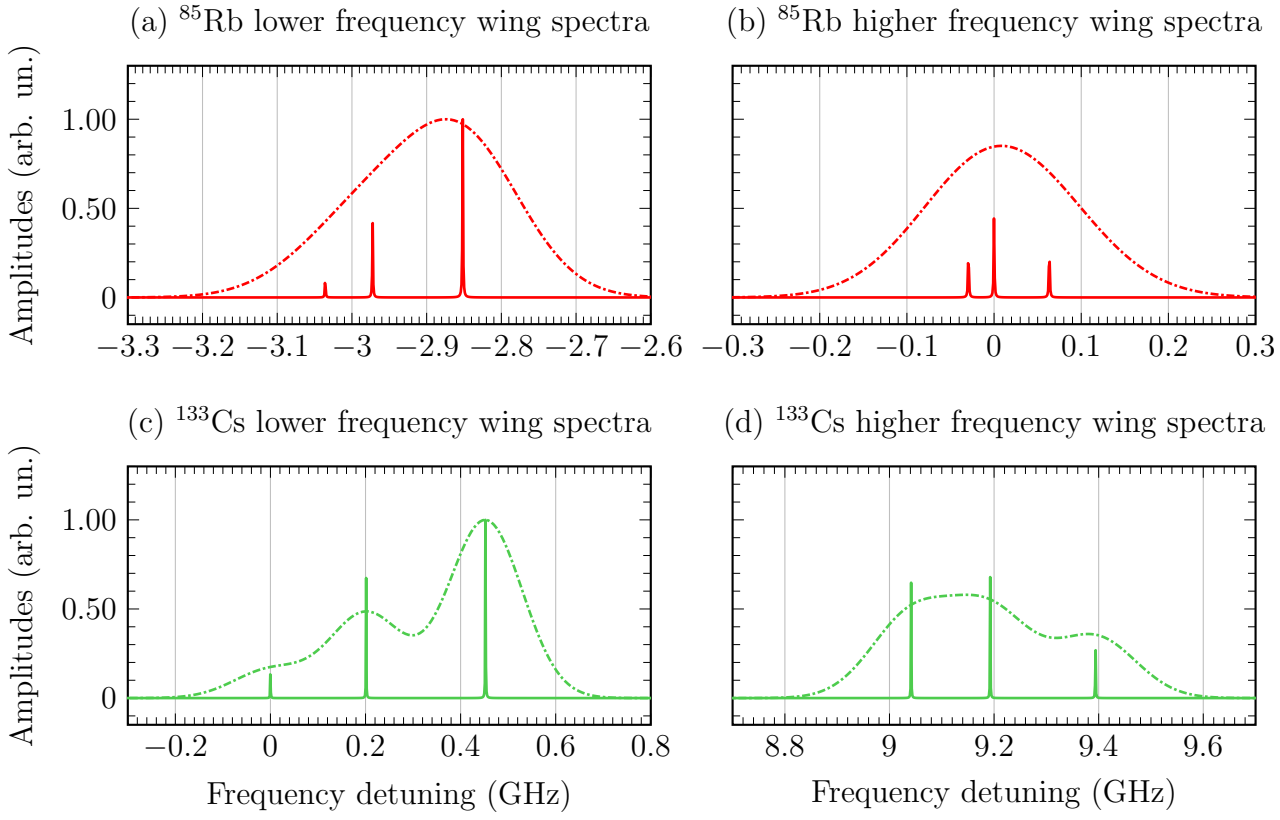

Figure 1.2: (a,b) ^{85}Rb and (c,d) ^{133}Cs D_2 line Doppler-broadened and natural linewidth spectra. For readability, the spectra have been normalized to the strongest transition and split into lower and higher frequency wings. For the ^{85}Rb D_2 line spectra, the zero frequency has been set to that of the transition $F_g = 2 \rightarrow F_e = 2$. In the case of ^{133}Cs D_2 line spectra, the transition $F_g = 4 \rightarrow F_e = 3$ was chosen as the zero frequency.

1.2 Review on sub-Doppler spectroscopic techniques

In the previous section, we have shown that due to the thermal motion of atoms, makes impossible the study of individual hyperfine transitions by conventional spectroscopic techniques, as they are partially or completely masked by the Doppler profile. Fortunately, methods allowing to

overcome partially or completely the Doppler effect have been developed and we make here-after a short review for some of the most widely used.

1.2.1 Atomic beam

An elegant way to reduce the Doppler broadening is to act directly onto the monokinetic atomic velocity distribution of atoms. The reduction of the velocity distribution can be achieved using a collimated beam, see for example [2, 31]. To form an atomic beam, alkali metals are placed in a stove heated at about 500 °C, providing a high vapor density. Atoms effuse from the stove through a small hole and propagate in a vacuum chamber over a distance d, usually of a few meters, before meeting a narrower slit of width w. The interaction region, located after the slit, is formed by the crossing of a laser beam propagating perpendicular to the atomic beam. If the laser beam propagates along the z-axis, then the Doppler broadening depend on the z speed component of the atomic velocities which is reduced by the geometrical factor

$$v_z = v_x \tan\epsilon \leqslant \frac{w}{2d}\bar{v}, \qquad \bar{v} = \sqrt{\frac{8k_B\Theta}{\pi m_a}}, \tag{1.14}$$

where $\bar{v}$ is the mean velocity of particles with mass m_a, Θ is the temperature of the stove, $\epsilon = \tan^{-1}(w/2d)$ is the collimation angle and v_x is the velocity component of the atoms parallel to the collimated beam axis. Consequently, only the atoms within a narrow interval of speed $v_z \leqslant (w/2d)\bar{v}$ contribute to the absorption which results in a smaller width of the absorption line as compared to the Doppler width of such gas at thermal equilibrium.

The density of atoms flying until the end of the vacuum pipe rarely exceeds 10^{10} cm^{-3}, and taking into account the size of the laser beam of about one millimeter, the number of atoms in the interaction region is about 10^7 which is relatively low as compared to that of a vapor cell and sometimes leads to small signal-to-noise ratio. Although elegant, the atomic beam method is expensive and technically difficult for realization, in particular, it requires high quality vacuum pumping which must be uninterrupted during the experiment. One should also note the need of a large space to perform experiments as well as the requirement of frequent maintenance of the system (cleaning alkali metal condensed on the pipes, refilling of metals, etc.).

1.2.2 Saturated absorption spectroscopy

Another method to perform sub-Doppler spectroscopy is a pump-probe experiment realized in a vapor cell. Let us consider a two-level system composed of the ground state $|g\rangle$ and the excited state $|e\rangle$ separated by a frequency $\Delta E = \hbar\omega_{eg}$. For sufficiently large laser field intensities I, the pumping rate exceed the relaxation rate and thus the ground state population $\mathcal{N}_g$ dicreases while the excited state population $\mathcal{N}_e$ increases; the difference of populations $\Delta\mathcal{N} = \mathcal{N}_g - \mathcal{N}_e$ can be written as a power series [26]

$$\Delta\mathcal{N} = \Delta\mathcal{N}_0 + \sum_{i=1}^{+\infty} I^i \frac{d^i}{dI^i}\big[\Delta\mathcal{N}\big], \tag{1.15}$$

with $d\Delta\mathcal{N}/dI < 0$. The absorption of the system can be derived by the Beer-Lambert law

$$dI = -\Delta\mathcal{N} I \sigma_s dz, \tag{1.16}$$

where σ_s is the absorption cross-section, and z is the propagation direction of the laser field. making use of the two previous relations, one gets

$$dI = -\left[I\sigma_s\Delta\mathcal{N}_0 + I^2\sigma_s\frac{d(\Delta\mathcal{N})}{dI} + ...\right]dz, \tag{1.17}$$

where the first term in the rhs brackets describes the linear absorption while the second one in the same brackets is responsible for diminishing the absorption. Hence, the transition $|g\rangle \rightarrow |e\rangle$ saturates. In addition, when considering moving atoms, the saturation occurs mostly for the class of velocity such that the Doppler-shifted laser frequency is resonant with atomic lines. This particularity can be used to perform sub-Doppler spectroscopy.

The so-called saturated absorption (SA) spectroscopy consists in pumping the vapor with a strong laser field propagating in the $+z$ direction and probing it with another (attenuated) beam from the same source propagating in the $-z$ direction (counter-propagation), overlapping with each other in the cell. For the probe to detect the saturation induced by the pump, atom within a given class of velocity should interact with both beams at the same time which is only possible for atoms with $v_z \cong 0$. Consequently, a dip called *Lamb dip* after W. Lamb (1955 Nobel Prize), is formed within the Doppler profile at the atomic line frequency. The width of this dip is usually about two orders of magnitude less than the Doppler width, and can be as small as the natural linewidth if not broadened by the laser power or atomic collisions.

Let us note that when two (or more) atomic lines are overlapped under a Doppler-profile, one observes another peak in addition to the two formed Lamb dips: a cross-over resonance. This particular resonance occurs for atoms moving with velocities such that the pump is in resonance with one of their transitions, and the probe is in resonance with the other one; it is thus located at the exact middle between the two transitions. If m transitions are masked under a Doppler profile, then the SA spectrum includes

$$\binom{m}{2} = \frac{m!}{2!(m-2)!} \tag{1.18}$$

crossover resonances. While this technique is easily executed and is relatively cheap as compared for example to atomic beams, see section 1.2.1, one should note that as the SA is a non-linear technique, the dips' amplitude are not proportional to the transition amplitudes. As a consequence, the SA technique can be unreliable when one wants to measure precisely transition amplitudes or when many lines overlap under a Doppler profile.

1.2.3 Selective reflection spectroscopy

First observed in 1909 by R. Wood [32], the selective reflection (SR) of light from the interface between a dielectric and a resonant vapor is a manifestation of the change of the Fresnel reflection coefficient at the window-vapor boundary as a function of the laser frequency due to presence of atomic resonance lines, such that

$$R(\omega) = \left(\frac{n_w - n_v(\omega)}{n_w + n_v(\omega)}\right)^2, \tag{1.19}$$

where n_w is the refractive index of the window while $n_v(\omega)$ is the frequency dependent refractive index of the vapor. However, this simple description does not explained that, when performed at normal incidence, a sub-Doppler component is added to the usual dispersive spectrum. The reason of this additional sub-Doppler feature is due to a transient regime of interaction between the vapor and the incident electric field so that only the slowest atoms reach the steady state regime in the spatial region where the SR signal develops [33].

Later, it was shown that the Doppler-broadened component of the SR spectra vanishes when applying a low-frequency modulation to the laser as a consequence of recording the derivative of the SR signal with respect to the laser frequency. Ducloy and Fichet (1991) [34] have shown that when the laser frequency is modulated, the SR signal becomes exclusively sensitive to atoms flying parallel to the windows. And even thought considering a macroscopic cell, they have shown that the reflected signal develops within a layer whose size is the order of the laser wavelength. As an example, frequency modulated SR spectroscopy was succesfully used to measure the collisional broadening Cs D_2 line resonances [35]. Note that selective reflection is also an excellent spectroscopic tool when dealing with high density vapor with a cell whose length exceeds the optical depth of the medium (*i.e.* no transmitted light) [36] but also for atom-surface interactions [37].

1.2.4 Nanometric-thick cell spectroscopy

The previous section has suggested that reducing the length of vapor cells to dimension close to that of the laser wavelength induces a transient light-atom interaction regime allowing only slower atoms to contribute to the signal. For transmission spectroscopy, evidence of such narrow contribution was first shown by Briaudeau *et al.* (1996) [38] using a vapor cell whose minimal thickness was about 10 µm, still greater than the laser wavelength by an order of magnitude.

Sarkisyan *et al.* (2001) [39] have later reported the fabrication of a nanometric-thick cell (NC), where the vapor layer was 150 – 300 nm-thick. In their paper, they have also recorded the weak-probed Cs D_2 line spectrum with a 20 MHz bandwidth laser where the $\sim$ 40 MHz broadened lines (an order of magnitude less than the Doppler-width of Cs at ambient temperature) were resolved in the spectrum. To get a good signal-to-noise ratio, the cell was heated at about 110 °C.

Figure 1.3 shows schematic views of the cell with its size. The reservoir of alkali metal is placed relatively far from the windows to allow easy formation of a temperature gradient during the operation to prevent condensation of the vapor on the windows. To prevent any birefringence, the sapphire (sometimes garnet) windows were cut such that their crystallographic axis (c-axis) is aligned with the propagation one. The windows have a wedged form allowing to tune to various thicknesses in the range 40 to 1000 nm by a simple vertical translation of the incident laser beam. For additional information on the design of the NC, see [39] and refs. therein.

One of the most outstanding properties of the NC is the possibility to realize a sub-Doppler spectroscopy with a low power single beam experiment. Moreover, it does not require particular equipment for the operation outside of a small oven to reach the sufficient vapor density. Over the past years, NC was the core of fascinating studies such as cooperative interaction [17], atom-surface interactions [40], magneto-optical processes [41], or molecular sub-Doppler spectroscopy [42].

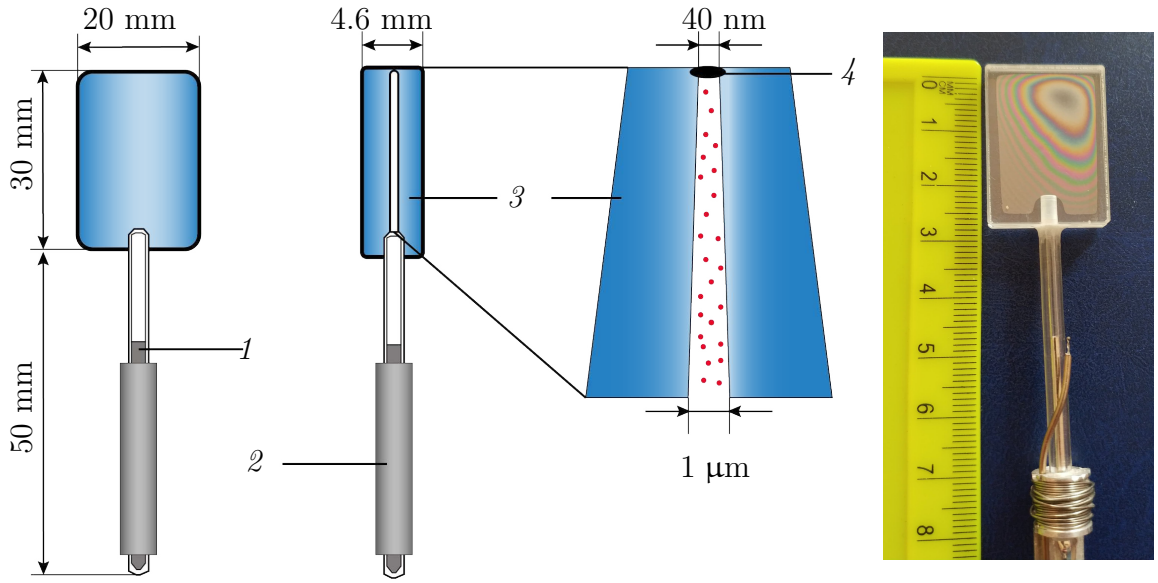

(a) Front view (b) Side view (c) Schematic gap view (d) Photograph

Figure 1.3: Schematic drawing of a nanocell: (a) front view, (b) side view, (c) schematic view of the gap where atoms are sketched as red balls, (d) photograph of the NC front view; *1* – alkali metal in the reservoir; *2* – metallic holder; *3* – high quality sapphire windows; *4* – glue.

1.3 Motivation and outline of the thesis

Selective reflection of light from the interface of a dielectric surface and resonant atomic vapor is known to be efficient spectroscopic tool for studies of high-density vapor, atom-surface interaction, etc., and has found numerous applications. Extension of this technique to the case of nanocells with the space between windows of the order of resonant radiation wavelength is promising both for deeper understanding of fundamental processes underlying interaction of laser radiation with atomic system and for new applications such as magnetic-field controlled tunable locking of laser frequency to atomic resonance lines. Meanwhile, as opposed to the case of ordinary cells, theoretical treatment of selective reflection from NCs is significantly complicated by involvement of additional effects, which have to be taken into account. Preliminary experimental studies demonstrate that the reflection spectrum indeed exhibits dramatic rapid oscillations with thickness ℓ.

We want to analyze the possible influence of concomitant effects inherent to resonant interaction of laser radiation with atoms confined in NC on SR spectra aiming at development of an appropriate theoretical model, which will be further verified and elaborated through experimental realization. Findings of this work will be used to define conditions of experimental studies using Rb or K nanocells with variable thickness.

This work also aims at understanding the behavior of thermal alkali vapors in a wide range of applied longitudinal magnetic fields and for different laser polarizations by monitoring NCs with selective reflection and derivative of Selective Reflection (dSR) techniques. The ultimate objective aims at developing a functional user-friendly wide range scalar magnetometer based on these previous studies.

1.3.1 Chapters

The present thesis is organized as follows:

- Chapter 1 presented an introduction to the field of sub-Doppler spectroscopy of thermal alkali vapors and outlined the scientific motivation of the work.

- Chapter 2 presents a low finesse Fabry-Pérot etalon model to describe the NC. The complete modeling requires to combine macroscopic equations (Maxwell's equations) to account propagation effects, with microscopic ones (optical Bloch equations) for the induced polarization. Numerical simulations show that even thought considering the Doppler effect, the contribution to the spectrum is mostly sub-Doppler, confirming that only slow atoms contribute to the signal for both reflection and transmission. Numerical simulations also suggest that the derivative of selective reflection profile experiences a large line narrowing which could be beneficial for various experiments. The last section of the chapter concerns experimental (SR and dSR) studies aiming at the validation of the model. Finally, the usefulness of the dSR technique is addressed for buffer-gas assisted and atom-surface interaction studies.

- Chapter 3 explores magneto-optical processes through the modification of alkali spectrum when exposed to a static magnetic field. A theoretical model starting from the Dirac equation is presented and allows to calculate the magnetic-field dependence of alkali D line energy levels, transitions frequencies and amplitudes. Numerical simulations yield useful results for natural Rb D_1 and D_2 lines and suggest particular regimes of circular dichroism depending on the magnetic field intensity. The model is verified with experimental realization of dSR spectroscopy of Rb and K NCs where a non-homogeneous magnetic field is applied with a permanent magnet.

- Chapter 4 exploits the findings of the previous chapters in the frame of sensing applications. A scheme to perform optical magnetometry is proposed and discussed in details, especially for its suitable operation parameters (atomic line, cell thickness and probe polarization). A proof of principle is given in the last section: a NC-based magnetometer driven by a Raspberry Pi computer and an Arduino Due board is built. A performance analysis is carried out to quantify precision (through coefficient of variation) and response time of the magnetometer in the range 0 to 2 kG. Possible optimization and outlook are addressed.

1.3.2 Appendices

Two appendices compiles various notes complementing the theoretical work proposed in this thesis:

- Appendix A gives complements on the density matrix and main approximations made in the course of this thesis.

- Appendix B presents some notes on angular momenta and the Wigner-Eckart theorem.

1.3.3 Thesis outcome

The present thesis is based on the following published and unpublished articles. Part of these results do not appear explicitly in the course of the thesis to preserve a good readability.

Published articles

- [43] A. Sargsyan, E. Klinger, Y. Pashayan-Leroy, C. Leroy, A. Papoyan, and D. Sarkisyan. *Study of Selective Reflection by an Optical Rb Cell with the Half- and Quarter-Wavelength thicknesses: application in strong magnetic fields*, J. Exp. Theor. Phys. Lett. **104**(4), (2016) 224.

- [44] A. Sargsyan, E. Klinger, G. Hakhumyan, A. Tonoyan, A. Papoyan, C. Leroy, and D. Sarkisyan. *Decoupling of hyperfine structure of Cs D_1 line in strong magnetic field studied by selective reflection from a nanocell*, J. Opt. Soc. Am. B **34**(4), (2017) 776.

- [45] E. Klinger, A. Sargsyan, A. Tonoyan, G. Hakhumyan, A. Papoyan, C. Leroy, and D. Sarkisyan. *Magnetic field-induced modification of selection rules for Rb D_2 line monitored by selective reflection from a vapor nanocell*, Eur. Phys. J. D **71**(8), (2017) 216.

- [46] E. Klinger, A. Sargsyan, C. Leroy and D. Sarkisyan. *Selective Reflection of Laser Radiation from Submicron Layers of Rb and Cs Atomic Vapors: Applications in Atomic Spectroscopy*, J. Exp. Theor. Phys. **125**(4), (2017) 543.

- [47] A. Tonoyan, A. Sargsyan, E. Klinger, G. Hakhumyan, C. Leroy, M. Auzinsh, A. Papoyan and D. Sarkisyan. *Circular dichroism of magnetically induced transitions for D_2 lines of alkali atoms*, Europhys. Lett. **121**(5), (2018) 53001.

- [48] A. Sargsyan, E. Klinger, A. Tonoyan, C. Leroy, and D. Sarkisyan. *Hyperfine Paschen–Back regime of potassium D_2 line observed by Doppler-free spectroscopy*, J. Phys. B: At. Mol. Opt. Phys., **51**(14), (2018) 145001.

- [49] E. Klinger. *Concept of an Optical Magnetometer Based on the Spectroscopy of Alkali Vapors Confined in Nanometric-Thick Cells*, J. Contemp. Phys. **53**(4), (2018) 313.

- [50] A. Sargsyan, E. Klinger, C. Leroy, T. A. Vartanyan and D. Sarkisyan. *Circular Dichroism of Atomic Transitions of the Rb D_1 Line in Magnetic Fields*, Opt. Spectrosc. **125**(6), (2018) 833.

Unpublished articles

- E. Klinger, H. Azizbekyan, A. Sargsyan, C. Leroy, D. Sarkisyan and A. Papoyan. *Proof of the feasibility of a nanocell-based wide-range optical magnetometer*, submitted to Appl. Opt., (2019). arXiv:1907.03106.

- A. Sargsyan, E. Klinger, C. Leroy, I. G. Hughes, D. Sarkisyan and C. S. Adams. *Selective reflection from a Potassium atomic layer with a thickness as small as $\lambda/13$*, accepted by J. Phys. B: At. Mol. Opt. Phys., (2019). arXiv:1905.05969.

Dissemination at international conferences

- E. Klinger, Y. Pashayan-Leroy, C. Leroy, D. Sarkisyan and A. Papoyan. *Selective reflection of laser radiation from an alkali metal nanocell.* 4th International Symposium, Optics & Its Applications (OPTICS-2016), Yerevan-Ashtarak, Armenia, July 25 – 28 (2016).

- E. Klinger, A. Amiryan, Y. Pashayan-Leroy, C. Leroy, A. Sargsyan, D. Sarkisyan and A. Papoyan. *Theoretical and experimental studies of selective reflection effect in a nanocell filled with alkali vapor.* 12th European Conference on Atoms, Molecules and Photons (ECAMP12), Frankfürt, Germany, Sept. 5 – 9 (2016).

- E. Klinger, A. Sargsyan, A. Tonoyan, G. Hakhumyan, A. Amiryan, A. Papoyan, C. Leroy, and D. Sarkisyan. *Forbidden at zero B-field atomic transitions monitored by selective reflection from a Rb vapor nanocell.* XXXIX Max Born Symposium: 5th International Symposium on Optics & its applications (OPTICS-2017), Wroclaw, Poland, July 3 – 7 (2017).

- E. Klinger, A. Sargsyan, A. Tonoyan, G. Hakhumyan, A. Amiryan, A. Papoyan, C. Leroy, and D. Sarkisyan. *Selective Reflection monitoring of forbidden at zero B-field atomic transitions of a Rb vapor nanocell.* 49th Conference of the European Group on Atomic Systems (EGAS49), Durham, United Kingdom, July 17 – 21 (2017).

- E. Klinger, A. Sargsyan, A. Tonoyan, G. Hakhumyan, A. Papoyan, C. Leroy, and D. Sarkisyan. *Investigation of alkaline vapors properties by derivative of Selective Reflection from a nanometric thickness cell.* Laser Physics 2018 International Conference (LP2017), Ashtarak, Armenia, Sept. 19 – 22 (2017).

- E. Klinger, A. Tonoyan, A. Sargsyan, G. Hakhumyan, A. Papoyan, C. Leroy, and D. Sarkisyan. *Giant Magnetic Circular dichroism exhibited using derivative of Selective Reflection spectroscopy.* 6th Symposium on Optics and its Applications (OPTICS-2018), Trento-Povo, Italy, Feb. 17 – 20 (2018).

- E. Klinger, A. Sargsyan, C. Leroy, A. Papoyan, and D. Sarkisyan. *Wide-range optical magnetometer based on hot alkaline vapor nanocell.* 50th Conference of the European Group on Atomic Systems (EGAS50), Kraków, Poland, July 9 – 13 (2018).

- E. Klinger, H. Azizbekyan, A Sargsyan, C. Leroy, D. Sarkisyan, and A Papoyan. *Optical Vapor Magnetometry using Nanocells*, OMNIDAV Workshop on Optical Magnetometry, Aghveran, Armenia, Sept. 15 – 16 (2018).

- E. Klinger, H. Azizbekyan, A Sargsyan, C. Leroy, D. Sarkisyan, and A Papoyan. *Optical Magnetometry using alkali Nanocells*, Laser Physics 2018 International Conference (LP2018), Ashtarak, Armenia, Sept. 18 – 21 (2018).

Chapter 2

Nanometric-thick Cell Spectroscopy

Contents

Introduction

Theoretical descrpition of the sub-Doppler structure of selective reflection spectra obtained from bulk cells have suggested that reducing the dimensions vapor cells leads to an enhancement of the spectral resolution. In fact, enhancement of spectral resolution for cells having a size close to that of resonant wavelength was known for years in the microwave domain as demonstrated by Romer and Dicke (1955) [51]. However, in the optical domain, it did not attract much attention until the mid 90's due to the difficulties of manufacturing such small vapor cells.

Vartanyan and Lin (1995) [52] have developed a theory of selective reflection and transmission from a thin vapor layer contained between two parallel plates (windows) and shown that a Doppler-free resonance occurs as a function of the layer thickness. Later, Zambon and Nienhuis (1997) [53] have discussed the symmetry properties of two-level atom lineshape and derived optical rotation and dichroism lineshape expressions; however without considering the reflection arising from the second window. The second reflection was later taken into account in the theoretical description of Dutier *et al.* (2003) [54] which lead to asymmetry of selective reflection and transmission profile. Recent development of another approach to describe the interaction of alkali vapor confined in NC with resonant light have demonstrated non-locality due to the atomic motion, responsible for a mesoscopic optical response [55].

In this chapter, we present a Fabry-Pérot (FP) model for the NC based on the works [53, 54]. We derive reflected and transmitted electric fields expressions from the Maxwell equation of propagation in the NC while making use of the continuity equations at each boundaries. These fields depend on the atomic polarization induced in the vapor which we derive for a two-level system in the dilute vapor regime and weak-probe limit by solving optical Bloch equations. In section 2.2, we present numerical simulations of the model, make a lineshape analysis and show that the derivative of selective reflection profile has an absorption-like shape, however being narrower than that of the absorption profile associated with the transmitted beam. Section 2.3 is dedicated to experimental studies of SR and dSR of Rb D lines in order to verify the theoretical predictions. In addition, by investigating K D_2 line spectrum for thicknesses less than 120 nm, we measure the C_3 coefficient associated with the van der Waals interaction between K atoms and the sapphire windows of the NC.

2.1 Theoretical considerations

2.1.1 Fabry-Pérot model for the NC

We consider the system schematically depicted on Fig. 2.1(a), composed of an atomic vapor sandwiched between two highly parallel windows having the same refractive index n_w and separeted by a distance ℓ. We have limited our study to a unique refractive index for the windows as the NCs produced in our laboratory do not have anti-reflection coatings. For the case of different refractive indices for both windows, see [54]. As long as the atomic vapor can be considered as dilute, the absorption can be neglected and the refractive index of the atomic vapor is very close to unity, that is $n_v \cong 1$.

(a) Sketch of the nanocell illumination (b) Sketch of a two-level system

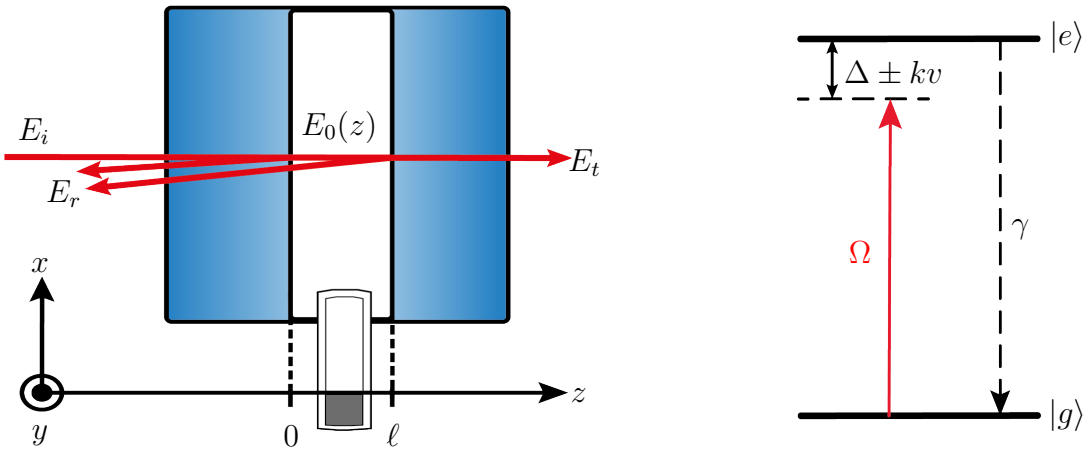

Figure 2.1: (a) Geometry of the problem: a thin vapor layer interacts with a near resonant incident light polarized in the plane (x, y) described by an electric field amplitude E_i. This field is partially reflected (E_r) partially transmitted (E_t) through the vapor. (b) Sketch of the vapor as a two-level system.

We consider a plane cw wave excitation directed at normal incidence onto the cell

$$\mathbf{E_i}(z,t) = \frac{1}{2} E_i \exp[-i(\omega t - kz)] \cdot \mathbf{e} + c.c. \tag{2.1}$$

where ω is the angular frequency of the laser field and $k = n_w\omega/c$ is the magnitude of the wave vector, the unit vector $\mathbf{e}$ denotes an arbitrary polarization in the (x, y) plane. We want to calculate the amplitude (and then the intensity) of the reflected and transmitted fields E_r and E_t. The atomic media is driven by the field $\mathbf{E_0}(z,t)$ inside the cell (from $z = 0$ to $z = \ell$) having the form

$$\mathbf{E_0}(z,t) = \frac{1}{2} E_0(z) \exp[-i(\omega t - kz)] \cdot \mathbf{e} + c.c. \tag{2.2}$$

The medium responses to this excitation by inducing the polarization $\mathbf{P_0}(z,t)$ having the local amplitude $P_0(z)$:

$$\mathbf{P_0}(z,t) = \frac{1}{2} P_0(z) \exp[-i(\omega t - kz)] \cdot \mathbf{e} + c.c. \tag{2.3}$$

It is important to note that we are not making any assumption on the form of $P_0(z)$ and $E_0(z)$, as the atomic response may exhibit inhomogeneities along the z-axis, arising from the possible transient effects associated with the atomic motion or with nonlinear response (pumping, saturation, etc.).

Propagation equation and solution

The field inside the diluted vapor obeys the Maxwell equation of propagation in the vacuum

$$\nabla^2 \mathbf{E_0} - \frac{1}{c^2}\frac{\partial}{\partial t}\mathbf{E_0} = \mu_0 \frac{\partial}{\partial t}\mathbf{P_0} \tag{2.4}$$

where $c = (\mu_0\epsilon_0)^{-1/2}$ is the speed of light, μ_0 is the vacuum permeability and ϵ_0 is the vacuum permittivity. Neglecting the losses in the medium, the propagation equation simplifies to

$$\frac{\partial^2}{\partial z^2}E_0(z) + 2ik\frac{\partial}{\partial z}E_0(z) = -\frac{k^2}{\epsilon_0}P_0(z), \tag{2.5}$$

that can be converted on an equivalent form:

$$\frac{\partial}{\partial z}\left[\exp(2ikz)\frac{\partial}{\partial z}E_0(z)\right] = -\frac{k^2}{\epsilon_0}P_0(z)\exp(2ikz). \tag{2.6}$$

Note that when the cell is empty, the resonant contribution $P_0(z)$ disappears and as a consequence the problem simplifies to the resolution of an elementary empty FP cell problem.

Using the continuity relations of the electric fields and their derivatives, at the boundaries $z = 0$ and at $z = \ell$, one gets

$$E_i + E_r = E_0(0), \qquad in_w k(E_i - E_r) = ikE_0(0) + \frac{\partial E_0}{\partial z}(0), \tag{2.7a}$$

$$E_0(\ell) = E_t, \qquad ikE_0(\ell) + \frac{\partial E_0}{\partial z}(\ell) = in_w kE_t, \tag{2.7b}$$

with ℓ the cell internal thickness and E_t the constant amplitude of the transmitted field through the second window. Integrating the propagation equations (2.5) and (2.6) between $z = 0$ and at $z = \ell$ we find

$$\frac{\partial E_0}{\partial z}(\ell) - \frac{\partial E_0}{\partial z}(0) + 2ik[E_0(\ell) - E_0(0)] = 2ikI_f, \tag{2.8a}$$

$$\frac{\partial E_0}{\partial z}(\ell)\exp(2ik\ell) - \frac{\partial E_0}{\partial z}(0) = 2ikI_b, \tag{2.8b}$$

where we have defined the forward and backward integral of the atomic response

$$I_f = \frac{ik}{2\epsilon_0}\int_0^\ell P_0(z)dz, \tag{2.9a}$$

$$I_b = \frac{ik}{2\epsilon_0}\int_0^\ell P_0(z)\exp(2ikz)dz. \tag{2.9b}$$

Assuming that the induced polarization is known (see section 2.1.2), the expression of E_r and E_t can be found by solving the linear system of equations composed by (2.7) and (2.8). We find that the reflected (respectively transmitted) field has two contributions: E_r' (respectively E_t') for the empty-FP solution, and E_r'' (respectively E_t'') for the resonant contribution; we have

$$E_r = \overbrace{r_w\left[1 - \exp(2ik\ell)\right]E_i/Q}^{E_r'} + \overbrace{t_{cw}\left[I_b - r_w I_f\exp(2ik\ell)\right]/Q}^{E_r''} \tag{2.10a}$$

$$E_t = \underbrace{t_{cw}t_{wc}E_i/Q}_{E_t'} + \underbrace{t_{cw}[I_f - r_w I_b]/Q}_{E_t''} \tag{2.10b}$$

where $Q = 1 - r_w^2\exp(2ik\ell)$ is the quality factor of the cavity; t_{cw} (cell-window), t_{wc} (window-cell) and r_w are respectively the transmission and reflection amplitude coefficients at the interfaces, having the following definition

$$t_{cw} = \frac{2}{n_w + 1}, \qquad t_{wc} = \frac{2n_w}{n_w + 1}, \qquad r_w = \frac{n_w - 1}{n_w + 1}. \tag{2.11}$$

Reflected and transmitted intensities for a dilute medium

Now, as we have found expressions for the electric fields, we are interested in calculating the intensity of the reflected and transmitted fields since intensity is the physical quantity measured by photo-detectors. By definition, the intensity is given by

$$\mathcal{I} = \frac{1}{2}\epsilon_0 c E E^*, \tag{2.12}$$

which leads to the calculation of the quantities $|E_r|^2 \equiv |E'_r + E''_r|^2$ for the reflected signal, and $|E_t|^2 \equiv |E'_t + E''_t|^2$ for the transmitted one. It is well known that the superposition of two electric fields gives rise to interference, and we can write

$$|E_r|^2 = |E'_r|^2 + |E''_r|^2 + 2\,\mathrm{Re}\,\{E'_r E''_r\}, \tag{2.13a}$$
$$|E_t|^2 = |E'_t|^2 + |E''_t|^2 + 2\,\mathrm{Re}\,\{E'_t E''_t\}. \tag{2.13b}$$

It means that the detected intensity in reflection has three contributions: the FP background signal $|E'_r|^2$, the signal re-emitted by the vapor $|E''_r|^2$, and the homodyne beating $\propto \mathrm{Re}\,\{E'_r E''_r\}$. These quantities read

$$|E'_r|^2 = \frac{2r_w^2}{|Q|^2}\big[1 - \cos(2k\ell)\big]E_i^2, \tag{2.14a}$$
$$|E''_r|^2 = \frac{t_{cw}^2}{|Q|^2}\Big[|I_b|^2 + r_w^2|I_f|^2 - 2r_w\,\mathrm{Re}\,\{I_f I_b^* \exp(2ik\ell)\}\Big], \tag{2.14b}$$
$$\mathrm{Re}\,\{E'_r E''_r\} = \frac{t_{cw}}{|Q|^2}\,\mathrm{Re}\Big\{r_w\big[1 - \exp(-2ik\ell)\big] \times \big[I_b - r_w I_f \exp(2ik\ell)\big]\Big\}E_i. \tag{2.14c}$$

The same remark holds for the transmitted intensity, and we have

$$|E'_t|^2 = \frac{t_{cw}^2 t_{wc}^2}{|Q|^2}E_i^2, \tag{2.15a}$$
$$|E''_t|^2 = \frac{t_{cw}^2}{|Q|^2}\Big[|I_f|^2 + r_w^2|I_b|^2 - 2\,\mathrm{Re}\,\big\{I_b I_f^*\big\}\Big], \tag{2.15b}$$
$$\mathrm{Re}\,\{E'_t E''_t\} = \frac{t_{wc}t_{cw}^2}{|Q|^2}\,\mathrm{Re}\,\{I_f - r_w I_b\}E_i. \tag{2.15c}$$

The reflected and transmitted intensities $\mathcal{I}_{SR}$ and $\mathcal{I}_T$ then read

$$\mathcal{I}_{SR} = \frac{1}{2}\epsilon_0 c\Big(|E'_r|^2 + |E''_r|^2 + 2\,\mathrm{Re}\,\{E'_r E''_r\}\Big), \tag{2.16a}$$
$$\mathcal{I}_T = \frac{1}{2}\epsilon_0 c\Big(|E'_t|^2 + |E''_t|^2 + 2\,\mathrm{Re}\,\{E'_t E''_t\}\Big). \tag{2.16b}$$

In most of cw laser spectroscopy experiments, the scanning range is much smaller than the free spectral range of the resonator implying that the FP contribution to the signal can be considered as a background. Thus we may consider only the resonant contributions, that is $S_r = |E_r|^2 - |E'_r|^2$ and $S_t = |E_t|^2 - |E'_t|^2$. Also, in the case of a dilute vapor, the FP-signal is much larger than the

one re-emitted by the vapor. Hence, the resonant contribution (the one that caries information on the vapor) arises mostly from the homodyne beating term, and we arrive at the expressions

$$S_t \cong 2\frac{t_{wc}t_{cw}^2}{|Q|^2}\,\mathrm{Re}\,\{I_f - r_w I_b\}E_i, \tag{2.17a}$$

$$S_r \cong 2\frac{t_{cw}}{|Q|^2}\,\mathrm{Re}\left\{r_w\big[1-\exp(-2ik\ell)\big]\times\big[I_b - r_w I_f\exp(2ik\ell)\big]\right\}E_i. \tag{2.17b}$$

2.1.2 Atomic Polarization

Microscopic equations

The macroscopic polarization arising from the interaction of an atomic ensemble with polarized light can be accuralty calculated using the density matrix formalism [56, 57], where the polarization is expressed as an average of dipoles

$$P_0(z,\omega) = N\langle d\rangle \propto \int dv M(v)\rho_{ij}(z,v), \tag{2.18}$$

where ρ_{ij} are the coherence (off-diagonal elements) of the density matrix. The dynamical behavior of the density matrix is given by the Liouville equation of motion (see appendix A.1)

$$\frac{d}{dt}\rho = -\frac{i}{\hbar}\big[\mathcal{H},\rho\big] - \frac{1}{2}\big\{\mathcal{R},\rho\big\} + \Lambda, \tag{2.19}$$

where $\mathcal{H} = \mathcal{H}_0 + \mathcal{H}_L$ is the Hamiltonian of the system composed by the sum of the unperturbed Hamiltonian $\mathcal{H}_0$ (atomic levels) with the interaction Hamiltonian $\mathcal{H}_L$ (laser). The matrix $\mathcal{R}$ describes relaxation processes while Λ account for the re-population, both in a phenomenological way; $\{a,b\} = ab + ba$ is the anticommutator.

For thermal vapors, the density matrix is in general a function of the position $\mathbf{r} = (x,y,z)$ and the time t. Hence, we should write the straight derivative d/dt in terms of partial derivatives:

$$d\rho(\mathbf{r},t) = \frac{\partial\rho}{\partial x}dx + \frac{\partial\rho}{\partial y}dy + \frac{\partial\rho}{\partial z}dz + \frac{\partial\rho}{\partial t}dt, \tag{2.20}$$

dividing everywhere by dt, one gets

$$\frac{d}{dt}\rho(\mathbf{r},t) = (\boldsymbol{\nabla}\cdot\mathbf{v})\,\rho(\mathbf{r},t) + \frac{\partial}{\partial t}\rho(\mathbf{r},t), \tag{2.21}$$

where $\mathbf{v}$ is the speed vector of the atoms. The geometry of the problem allows to consider only the z-component of both position and speed, that is $\rho \equiv \rho(z,v,t)$. In that case, Eq. (2.19) reduces to

$$\frac{\partial}{\partial t}\rho(z,v,t) + v\frac{\partial}{\partial z}\rho(z,v,t) = -\frac{i}{\hbar}\big[\mathcal{H},\rho\big] - \frac{1}{2}\big\{\mathcal{R},\sigma\big\} + \Lambda. \tag{2.22}$$

We make a transformation to a rotating frame, such that

$$\rho(z,v,t) = \sigma(z,v)\exp[i(kz-\omega t)] + c.c., \tag{2.23}$$

with $\sigma(z,v)$ the reduced density matrix. To find the equation of evolution of σ we shall inject (2.23) into (2.22), and in the steady state regime (that is for sufficiently long interaction time) the time derivative vanishes, and we get

$$v\frac{\partial}{\partial z}\sigma = -\frac{i}{\hbar}\big[\mathcal{H},\sigma\big] - \frac{1}{2}\big\{\mathcal{R},\sigma\big\} + \Lambda + i(\omega - kv)\sigma. \tag{2.24}$$

The amplitude of the macroscopic polarization (2.3) then reduces to the averaging of the coherences σ_{ij} of the reduced density matrix over the one-dimensional distribution of speed $M(v)$

$$P_0(z,\omega) = N\langle d\rangle = N\sum_{i\neq j} d_{ij}\int dv M(v)\sigma_{ij}(z,v), \tag{2.25}$$

where N is the vapor number density. The atomic distribution of speed $M(v)$ in the cell is assumed to be Maxwellian, and defined as $M(v) = (u\sqrt{\pi})^{-1}\exp(-v^2/u^2)$ with u the thermal velocity given by $u(\Theta) = \sqrt{2k_B\Theta/m_a}$. Here, we suppose a one-dimensional problem such that $v \equiv v_z$ is the projection of the atomic velocities onto the z-axis. Let us note that Todorov and Bloch (2017) [58] have recently discussed this assumption.

Atoms confined in the cell may move with positive or negative velocities along the z-axis, depending whether they move with increasing or decreasing z respectively. Consequently, the previous integral should be calculated between $-\infty$ to $+\infty$. It is usually well assumed that, in absence of anti-relaxation coating, atoms loose coherence when colliding with the cell's walls. As a consequence, at each windows we have $\sigma_{ij}(z=0,v) = \sigma_{ij}(z=\ell,v) = 0$ (for $i \neq j$), and we may separate the contributions to the polarization into two parts: one arising from the atoms departing from the wall at $z = 0$ with positive velocities and the other one from atoms departing from the wall at $z = \ell$ with negative velocities. Hence, the integral of (2.25) can be performed only on the positive velocities, and supposing that $M(v)$ is symmetric, we arrive at

$$P_0(z) = N\sum_{i\neq j} d_{ij}\int_0^{+\infty} dv M(v)\Big[\sigma_{ij}^{+}(z,v) + \sigma_{ij}^{-}(z,-v)\Big]. \tag{2.26}$$

In order to calculate the atomic polarization, we will need to solve the system of ordinary differential equations (ODEs) generated by the expansion of (2.24), and in most of the cases it will be difficult or even impossible to extract analytical solutions. For this reason, we only consider the case of a two-level system in the weak-driving approximation [53]. Outside of this simple case, it is better to numerically solve the system of ODEs arising from (2.24), with a Runge-Kutta routine. This method has, for example, accurately described electromagnetically induced transparency (EIT) experiments in NC, see [59].

Weak Driving Field approximation for a two-level system

At first, and using the results derived in the previous paragraph, we want to study the simple case of a two-level system interacting with a non-saturating laser field. We consider the two-level system with a ground state labeled $|g\rangle$ and an excited state $|e\rangle$, (see Fig. 2.1(b)) described by the Hamiltonian

$$\mathcal{H} = \hbar\omega_0|e\rangle\langle e| - \hbar\Omega|g\rangle\langle e| - \hbar\Omega|e\rangle\langle g|, \tag{2.27}$$

where $\Omega = d_{eg}E_0(z)\hbar^{-1}$ is the Rabi frequency, obtained by expanding the Hamiltonian $\mathcal{H}_L = \mathbf{d}\cdot\mathbf{E}$ in the frame of rotating wave and dipolar approximations, see appendix A.2. Note that we have shifted the energy axis such that the energy of the ground state is zero (*i.e.* $\hbar\omega_0$ represents the energy difference between the state $|e\rangle$ and $|g\rangle$). The relaxation matrix is assumed to be diagonal and set to

$$\mathcal{R} = \Gamma|e\rangle\langle e|, \tag{2.28}$$

where Γ parametrize the flow of population from the state $|e\rangle$ to $|g\rangle$ due to spontaneous emission. Let us remark that $\langle g|\mathcal{R}|g\rangle = 0$, the ground state does not decay. If all diagonal elements of $\mathcal{R}$ are simultaneously non-zero, the density matrix is damped over time which is out of our scope. Thus, the populations verify

$$\sigma_{gg} + \sigma_{ee} = 1 \quad \forall z, \qquad \frac{\partial}{\partial z}\big(\sigma_{gg} + \sigma_{ee}\big) = 0 \quad \forall z, \tag{2.29}$$

and the repopulation matrix expression has to be $\Lambda = \Gamma\sigma_{ee}$.

The atoms are driven by the electric field (2.2) propagating in the cell and having an amplitude $E_0(z)$; thus, without additional assumptions, atoms experience a different Rabi frequency Ω depending on their position. In the case of a dilute medium, we may consider that the vapor is essentially driven by the field $E_0'(z)$ (empty FP-cavity), that is to say $E_0(z) = E_0'(z) + E_0''(z) \cong E_0'(z)$. Using the expression of the fields (2.10) along with the boundary conditions (2.7), we find that the amplitude of the driving field reads

$$E_0(z) = \frac{E_i t_{wc}}{Q}\Big\{1 - r_w \exp\big[2ik(\ell - z)\big]\Big\}, \tag{2.30}$$

regardless of the incident electric field strength. As long as E_i remains weak, the interaction with the vapor will stay linear and one may write the electric field and the polarization as a sum of forward and backward propagating waves

$$E_0(z,t) = \frac{1}{2}E_0^+ \exp[-i(\omega t - kz)] + \frac{1}{2}E_0^- \exp[-i(\omega t + kz)] + c.c., \tag{2.31a}$$

$$P_0(z,t) = \frac{1}{2}P_0^+(z) \exp[-i(\omega t - kz)] + \frac{1}{2}P_0^-(z) \exp[-i(\omega t + kz)] + c.c., \tag{2.31b}$$

with $P_0^+(z)$ (respectively $P_0^-(z)$) driven only by the forward (respectively backward) electric field amplitude E_0^+ (respectively E_0^-). Let us note that Eq. (2.31a) is equivalent to (2.2), and using (2.30) we identify $E_0^\pm$ as

$$E_0^+ = \frac{t_{wc}}{Q}E_i, \qquad E_0^- = -r_w \exp(2ik\ell)\frac{t_{wc}}{Q}E_i. \tag{2.32}$$

Combining Eq. (2.3) with (2.31b) we get

$$P_0(z) = P_0^+(z) + P_0^-(z)\exp(-2ikz). \tag{2.33}$$

Consequently, and as long as the weak excitation approximation is satisfied, the driving field can be considered as a traveling wave with constant amplitude, implying that the light field "seen"

by the atoms along their motion in the cell corresponds to a constant Rabi frequency; which is related to the so-called optically thin medium approximation, see e.g. [54] and refs. therein. Let us note that $E_0^- = -r_w \exp(2ik\ell)E_0^+$. In addition, assuming some symmetry between the windows (velocity distribution, identical surface interactions, etc.), one has

$$\frac{P_0^-(\ell - z)}{E_0^-} = \frac{P_0^+(z)}{E_0^+}, \tag{2.34}$$

and (2.32) can be re-written as a function of $P_0^+(z)$ only, that is

$$P_0(z) = P_0^+(z) - r_w P_0^+(\ell - z)\exp[2ik(\ell - z)]. \tag{2.35}$$

The problem is then reduced to a one traveling-wave excitation with a constant amplitude E_0^+ and a constant Rabi frequency $\Omega = d_{eg}E_0^+/\hbar$. Neglecting multiple internal reflections inside the cell, we should be able to express the integrate of the induced polarization (2.9) as a combination of the common transmission and reflection signals, respectively governed by

$$I_T^{lin} = \frac{ik}{2\epsilon_0}\int_0^\ell dz P_0^+(z), \tag{2.36a}$$

$$I_{SR}^{lin} = \frac{ik}{2\epsilon_0}\int_0^\ell dz P_0^+(z)\exp(2ikz). \tag{2.36b}$$

Making use of Eqs. (2.35) and (2.36), we can re-write (2.9) as

$$I_f = I_T^{lin} - r_w I_{SR}^{lin}, \tag{2.37a}$$

$$I_b = I_{SR}^{lin} - r_w \exp(2ik\ell)I_T^{lin}, \tag{2.37b}$$

which are needed to calculate the signals given by (2.17). For a two-level system driven by the field E_0^+, the atomic polarization (2.26) reduces to

$$P_0^+(z) = N d_{eg}\int_0^{+\infty} dv M(v)\Big[\sigma_{eg}^+(z,v) + \sigma_{eg}^-(z,-v)\Big], \tag{2.38}$$

where both $\sigma_{eg}^+(z,v)$ and $\sigma_{eg}^-(z,-v)$ are driven by the Rabi frequency $\Omega = d_{eg}E_0^+/\hbar$. In order to calculate the atomic polarization from (2.26), we must find the expression of $\sigma_{eg}^\pm$.

Expanding equation (2.24) we have to solve the following system of ODEs

$$v\frac{\partial}{\partial z}\sigma_{gg} = +i\Omega(\sigma_{eg} - \sigma_{ge}) + \Gamma\sigma_{ee}, \tag{2.39a}$$

$$v\frac{\partial}{\partial z}\sigma_{ee} = -i\Omega(\sigma_{eg} - \sigma_{ge}) - \Gamma\sigma_{ee}, \tag{2.39b}$$

$$v\frac{\partial}{\partial z}\sigma_{eg} = +i\Omega(\sigma_{gg} - \sigma_{ee}) - \Lambda_\pm\sigma_{eg}, \tag{2.39c}$$

where $\Lambda_\pm = \gamma - i\Delta \pm ikv$, where γ is the Half Width at Half Maximum (HWHM) homogeneous linewidth, $\Gamma = 2\pi/\tau_l$ represents the natural linewidth (FWHM), $\Delta = \omega - \omega_0$ is the detuning

of the laser frequency with the resonance, Doppler shifted by $\pm kv$ for the atom moving with a positive or negative velocity. To account for additional decoherence processes leaving the population unchanged (for example elastic collisions), the homogeneous linewidth $\gamma = \Gamma/2$ is replaced by $\gamma = \Gamma/2 + \gamma_f$. In the case of a non-saturating field (weak excitation), the Rabi frequency Ω is much smaller than the relaxation Γ ($\Omega \ll \Gamma$), implying that the excited state is practically not populated, and we may set $\sigma_{gg} - \sigma_{ee} \cong 1$. In that case, and for positive velocities, Eq. (2.39c) reduces to

$$\frac{\partial}{\partial z}\sigma_{eg}^{+}(z, v, \Delta) = i\frac{\Omega}{v} - \frac{\Lambda_+}{v}\sigma_{eg}^{+}(z, v, \Delta), \tag{2.40}$$

easily solvable using the variation of parameters method. Let us remark that if we take the complex conjugate of the Bloch equation (2.40), and recalling the initial conditions $\sigma_{eg}(0, v) = \sigma_{eg}(\ell, v) = 0$, we get a useful relation

$$\sigma_{eg}^{-}(z, -v, \Delta) = -\sigma_{eg}^{+*}(\ell - z, v, -\Delta), \tag{2.41}$$

allowing one to evaluate only the contribution of the positive velocities to recover both contributions. The solution of the homogeneous equation $\partial_z \sigma'_{eg} + \Lambda_+ \sigma'_{eg}/v = 0$ is $\sigma'_{eg} = K \exp[-\Lambda_+ z/v]$ with K an integration constant, and it follows that the solution of equation (2.40) can be expressed as $\sigma_{eg}^{+} = K(z)\exp[-\Lambda_+ z/v]$, where $K(z)$ is specified by injecting the form of σ_{eg}^{+} into the differential equation it satisfies. Using the above-mentioned initial conditions and relation (2.41), one gets

$$\sigma_{eg}^{+}(z, v, \Delta) = \frac{i\Omega}{v}\left\{1 - \exp\left[-\frac{\Lambda_+}{v}z\right]\right\}, \tag{2.42a}$$

$$\sigma_{eg}^{-}(z, -v, \Delta) = \frac{i\Omega}{v}\left\{1 - \exp\left[-\frac{\Lambda_-}{v}(\ell - z)\right]\right\}. \tag{2.42b}$$

Injecting these later expressions into (2.38) and then in (2.36), while swapping the integrals over v and z, we get

$$I_T^{lin} = \frac{ik}{2\epsilon_0}\int_0^{+\infty} M(v)dv \int_0^{\ell}\left[\sigma_{eg}^{+}(z, v) + \sigma_{eg}^{-}(z, -v)\right]dz, \tag{2.43a}$$

$$I_{SR}^{lin} = \frac{ik}{2\epsilon_0}\int_0^{+\infty} M(v)dv \int_0^{\ell}\left[\sigma_{eg}^{+}(z, v) + \sigma_{eg}^{-}(z, -v)\right]\exp(2ikz)dz. \tag{2.43b}$$

Finally, by performing the integral over z and re-writing the one over v from $-\infty$ to $+\infty$, we can express the integrals I_T^{lin} and I_{SR}^{lin} as

$$I_T^{lin} = A\int_{-\infty}^{+\infty} dv M(v) g(v, \Delta), \tag{2.44a}$$

$$I_{SR}^{lin} = A\int_{-\infty}^{+\infty} dv M(v) h_{\pm}(v, \Delta), \tag{2.44b}$$

where the strength factor A depends on the atomic density N, the transition dipole moment d_{eg}, the transmission coefficient t_{wc} and the driving field E_0^{+}:

$$A = \frac{N|d_{eg}|^2}{2\hbar\epsilon_0}E_0^{+} = \frac{N|d_{eg}|^2}{2\hbar\epsilon_0}\frac{t_{wc}E_i}{Q}. \tag{2.45}$$

The functions g and h read

$$g(v,\Delta) = -\frac{k}{\Lambda_+}\left\{\ell - \frac{|v|}{\Lambda_+}\left[1-\exp\left(-\frac{\Lambda_+\ell}{|v|}\right)\right]\right\}, \tag{2.46a}$$

$$h_\pm(v,\Delta) = \frac{1}{2i}\left[\frac{1}{\Lambda_\mp} - \frac{\exp(2ik\ell)}{\Lambda_\pm}\right] - \frac{k|v|}{\Lambda_+\Lambda_-}\exp\left(-\frac{\Lambda_\mp\ell}{|v|}\right), \tag{2.46b}$$

where g is valid for both positive and negative velocities, while h_+ stands for the positive and h_- for the negative ones.

2.2 Numerical simulations

In the previous section, we have derived a theoretical model describing the interaction of a two-level system confined in a low-finesse Fabry-Pérot cavity, with near-resonant incident laser light. We now want to study the evolution of the transmission and reflection profiles versus the cell thickness. We thus present here-after a computational procedure to calculate numerically this evolution; we show and comment the model's predictions. To fit more realistic cases, we discuss the possibility to describe the vapor as an ensemble of two-level systems and give the respective formulas.

2.2.1 Computational procedure

To illustrate the theoretical model, one can calculate the transmission and reflection profiles versus the NC's thickness. To do so, we have written a MATLAB program which performs numerical evaluation of (2.44) with the `trapz()` function. This result is later injected in (2.37) and then in (2.17). In the calculations, the homogeneous broadening γ and the cell thickness ℓ are left as free parameters. While the temperature is also a free parameter, our model does not accurately describe its impact. However one expects the two following qualitative changes occuring with the increase of temperature: an overall amplitude increase through $N \equiv N(\Theta)$ and additional (collisional) broadening, which can be taken into account in γ_f, as long as the number density stays low enough that cooperative effects can be discarded, see for example [16]. Let us remark that a divergence will occur when trying to evaluate the terms of type $|v|^{-1}$ for $v = 0$. Using the properties of the exponential function, it is good to note the following limits:

$$\lim_{v\to 0} g(v,\Delta) = -\frac{k\ell}{\Lambda_0}, \tag{2.47a}$$

$$\lim_{v\to 0+} h(v,\Delta) = \lim_{v\to 0-} h(v,\Delta) = \frac{1}{2i}\left[\frac{1-\exp(2ik\ell)}{\Lambda_0}\right], \tag{2.47b}$$

with $\Lambda_0 = \gamma - i\Delta$. As another remark, the integration on v should be performed from $-\infty$ to $+\infty$ which is not possible with numerical calculations: appropriate numerical bounds should be specified. Fortunately, moving atoms should contribute to the signal only if they interact long enough with the laser beam, that is for a time $\sim (2\cdot 2\pi\gamma)^{-1}$ (the factor 2 accounts for the FWHM of the transition) without experiencing decoherence while having a time of flight

(wall to wall) $\tau = \ell/v$. Thus atoms with a speed $v \gg 2\pi\ell\gamma$ will not have time to interact with the laser. This statement is verified here-after, from Fig. 2.2, where we plot the derivative of selective reflection signal as a function of the linear detuning where the integral (2.44) has been calculated between the reduced bounds $[-v_b, +v_b]$ with $v_b = \xi \cdot 4\pi\ell\gamma$ and ξ ranged between 0.25 and 250. We see from panel (b) that the curves corresponding to the case $\xi = 1$ and onward almost overlap with each other. Thus, one can chose $v_b = 4\pi\ell\gamma$ as the bounds of the integral in (2.44) to perform the numerical integration.

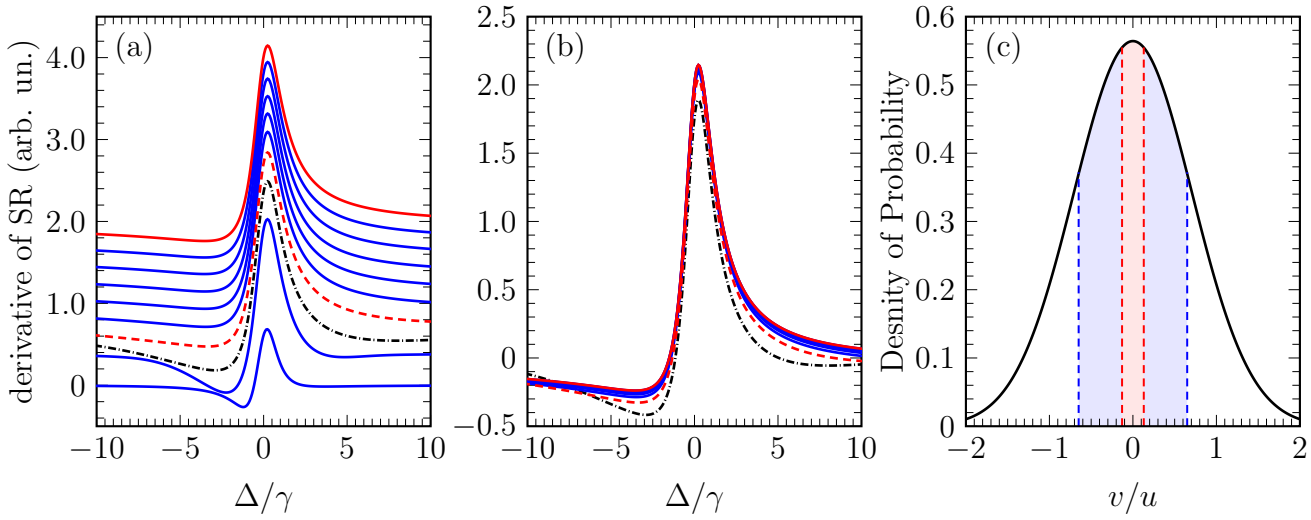

Figure 2.2: Evolution of the dSR spectrum as a function of the linear detuning calculated for $\ell = \lambda/4$, where the integral (2.44) has been calculated between the reduced bounds $[-v_b, +v_b]$ with $v_b = \xi \cdot 4\pi\ell\gamma$, for $\xi = 0.05$, 0.25, 0.5 (black dashdotted line), 1 (red dashed line), 1.5, 2, 2.5, 4, 5, and 250 (red solid line). On panel (a), the curves have been shifted vertically from each other by 0.2 for clarity, while keeping the same amplitude scale. On panel (b), the curves corresponding to $\xi = 0.5$ to $\xi = 250$ have been superimposed. On panel (c), the filled areas under the curve $M(v)$ correspond to $v_b/u = 0.13$ ($\xi = 1$, in red), and $v_b/u = 0.65$ ($\xi = 5$, in blue). The case $\xi = 250$ corresponds to the maximum speed $v_b/u = 32.5$.

This procedure repeated over the value of the laser frequency was used to calculate the theoretical spectra presented in some of our published works [43, 44, 45, 46]. Let us note that this procedure can be time consuming, due particularly to the numerical integration. The possibility of evaluating analytically the velocity integration (2.44) was shown by [54, 60] when considering the frequency modulated (FM) spectroscopy [34]. From an experimental point of view, the FM spectroscopy is known to yield high signal-to-noise ratio to the only "cost" of recording the derivative of the signal, which might not be a drawback in our case. For a short finite-length cell such that $\ell \ll u/\gamma$, Dutier *et al.* (2003) [54] have shown that the transmitted

and reflected signals are governed by

$$\frac{d}{d\omega}S_t = \frac{2(1-r_w)(1-r_w^2)}{|Q|^2}E_i\,\mathrm{Re}\left(\frac{dI_T}{d\omega}\right), \tag{2.48a}$$

$$\frac{d}{d\omega}S_r = -\frac{4(1-r_w)r_w\sin(k\ell)}{|Q|^2}E_i\,\mathrm{Im}\left(\frac{dI_T}{d\omega}\right), \tag{2.48b}$$

where

$$\frac{dI_T}{d\omega} = -\frac{4i}{\sqrt{\pi}ku}A\big[1-r\exp(ik\ell)\big]^2 \times \frac{\sin(k\ell/2)^2}{\gamma-i\Delta}. \tag{2.49}$$

We shall verify the consistency of the numerical integration with the formulas presented above in the range of thicknesses we are going to work with. Figure 2.3 shows dSR profiles as a function of the frequency detuning calculated with numerical integration and formulas (2.48b, 2.49) for $\ell = \lambda/4,\ 3\lambda/8,\ 5\lambda/8,\ 3\lambda/4$. As the thickness increases, discrepancies between both methods can be seen: the condition $\ell \ll u/\gamma$ may not be satisfied for these parameters (close to experimental conditions). Hence, when calculation time is not an issue, one will prefer using the numerical integration method.

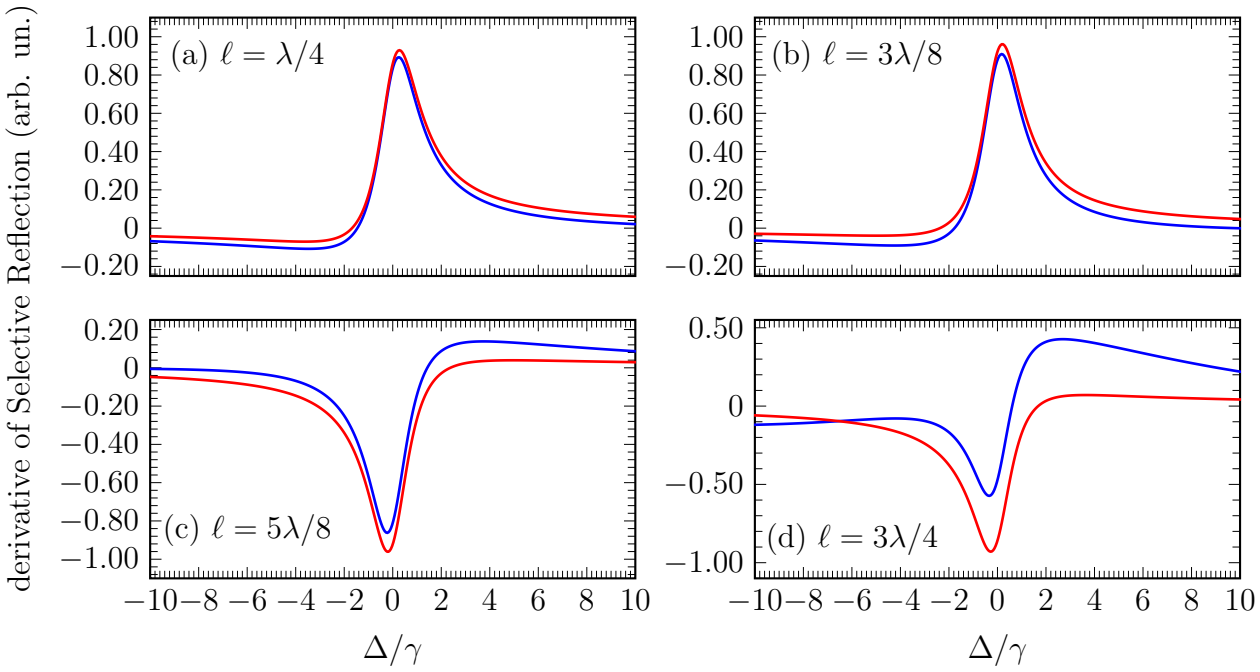

Figure 2.3: Comparison between dSR profiles calculated with numerical integration (red solid lines) and with formulas (2.48b, 2.49) (blue solid line) for (a) $\ell = \lambda/4$, (b) $\ell = 3\lambda/8$, (c) $5\lambda/8$, (d) $3\lambda/4$; $\gamma = 2\pi \cdot 40$ MHz and $\Theta = 130$ °C. For the lowest thicknesses, both approaches are consistent with each other; discrepancies appear with increasing thickness.

It is important to note that the two-level system calculations performed before describe a simple system having only two levels. However in the experiment, the most simple atomic system we can study is composed of four two-level systems for the alkali D_1 lines. It will be necessary

to understand how this difference can be taken into account. For the moment, let us analyze what our model predicts for the lineshape.

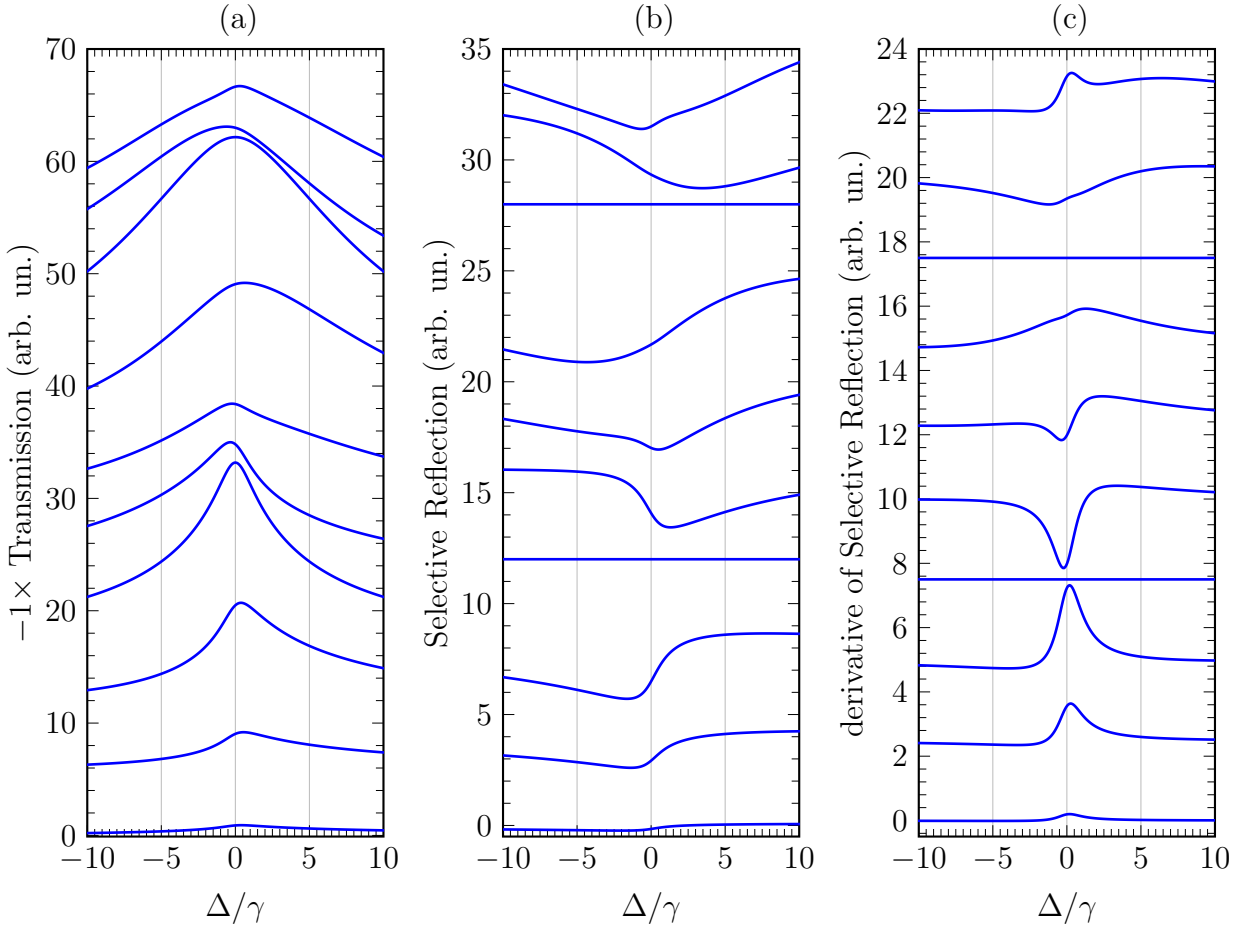

Figure 2.4: Qualitative evolution with increasing thickness (bottom to top) from $\ell = \lambda/8$ to $\ell = 5\lambda/4$ with a step of $\lambda/8$ for: (a) transmission profile, (b) selective reflection profile and (c) derivative of the selective reflection profile. For clarity, the curves have been shifted vertically from each other with equal intervals of 6, 4 and 2.5 for the absorption, the selective reflection and its derivative respectively, while preserving the same amplitude scale.

2.2.2 Lineshape analysis

The qualitative evolution of the transmission, selective reflection and its derivative in the range $\lambda/8 \leqslant \ell \leqslant 5\lambda/8$ is shown in Fig. 2.4 with a step of $\lambda/8$. First of all, one can see that the transmission is no longer a simple absorption spectrum nor symmetric in contrast to what was predicted by Zambon and Nienhuis (1997) [53] when setting the second window's reflection coefficient to zero. Indeed, the derived expressions (2.37) combined with the ones of the resonant fields E_t'' and E_r'' (2.10) show how thin-cell spectroscopy combines interferometrically responses known to be associated either to transmission spectroscopy (I_T^{lin}) or to the selective reflection

spectroscopy (I_{SR}^{lin}), impacting both the lineshape and the linewidth of the signal:

$$I_T = I_f - r_w I_b = \left[1 + r_w^2 \exp(2ik\ell)\right] I_T^{lin} - 2r_w I_{SR}^{lin}, \tag{2.50a}$$

$$I_{SR} = I_b - r_w I_f \exp(2ik\ell) = \left[1 + r_w^2 \exp(2ik\ell)\right] I_{SR}^{lin} - 2r_w \exp(2ik\ell) I_T^{lin}, \tag{2.50b}$$

where I_T is the thin-cell transmission and I_{SR} the thin-cell reflection. Hence, the transmission spectrum includes a dispersive contribution while the selective reflection includes a transmission one. Moreover, although all the spectra are sub-Doppler (one expect spectra with a FWHM a few order of magnitude larger than the homogenous broadening γ), one can see an additional narrowing mechanism occurring for $\ell = m\lambda/2$, which is a manifestation of the so-called coherent Dicke narrowing, initially observed by Romer and Dicke (1955) [51] in the microwave domain.

As for the selective reflection (see Fig. 2.4(b)), one immediatly note that the signal vanishes for the thicknesses $\ell = m\lambda/2$, which is a consequence of the FP behavior of the NC. In fact, let us recall that the signals presented on Fig. 2.4 are only the homodyne beating between the FP and spontaneous emission from atoms, see Eq. (2.14). For experiments at $\ell = m\lambda/2$, one can expect to record the signal re-emitted by the vapor, whose amplitude is much smaller than the selective reflection, is proportional to $|E_r''|^2$. One can also note that the usual dispersive shape slowly disappears with the increase of thickness.

In the panel (c) of Fig. 2.4 we plot the derivative of selective reflection which exhibits a shape resembling the transmission one. One note however that the profile of dSR has much smaller wings, and is narrower. For many studies, it is preferable to have as narrow resonances as possible. Thus, we will prefer the dSR spectrum to the transmission in the studies presented in this thesis. One can also note a sign oscillation of the dSR profile with a periodicity of $\lambda/2$. In what follows, we will mostly be interested by the selective reflection and its derivative as they show attractive properties for atomic spectroscopy. The peculiarities of the selective reflection and its derivative will be explored experimentally in section 2.3, where the coincidence between the theory and experiment is analyzed; but before, let us discuss the possibility of describing the vapor as an ensemble of two-level systems.

2.2.3 Ensemble of two-level systems

In the experiment, the recorded spectra will be composed of various amount of lines, distinguishable or not whether the separation between them is smaller or bigger than the transition linewidth. Even though the model depicted above considers only two-level atoms, it seems reasonable that in the first approximation, one can make use of the superposition theorem. Indeed, we may consider the atomic levels to be independent from each other in the linear regime of interaction and in the dilute medium approximation. Hence, the vapor may be viewed as an ensemble of two-level systems, and the total polarization is simply the superposition of the contribution of each hyperfine transition. It means that we can rewrite (2.38) as

$$P_0^+(z) = \sum_i N d_i \int_0^{+\infty} dv M(v) \left[\sigma_{eg}^+(z, v, \Delta_i) + \sigma_{eg}^-(z, -v, \Delta_i)\right], \tag{2.51}$$

with $\Delta_i = \omega - \omega_i$; and in that case equations (2.44) read

$$I_T^{lin} = \sum_i A_i \int_{-\infty}^{+\infty} dv M(v) g(v, \Delta_i), \tag{2.52a}$$

$$I_{SR}^{lin} = \sum_i A_i \int_{-\infty}^{+\infty} dv M(v) h_{\pm}(v, \Delta_i). \tag{2.52b}$$

In this description, each hyperfine transition arises from a two-level system $|e, g\rangle_i$ and has two parameters: a transition frequency $\omega_i = \omega_e - \omega_g$ and an amplitude A_i which depends on a Clebch-Gordan coefficient; oscillator strengths can also be used if only looking for qualitative results. For alkali atoms, these two parameters can be found for example in [28, 29, 30, 61].

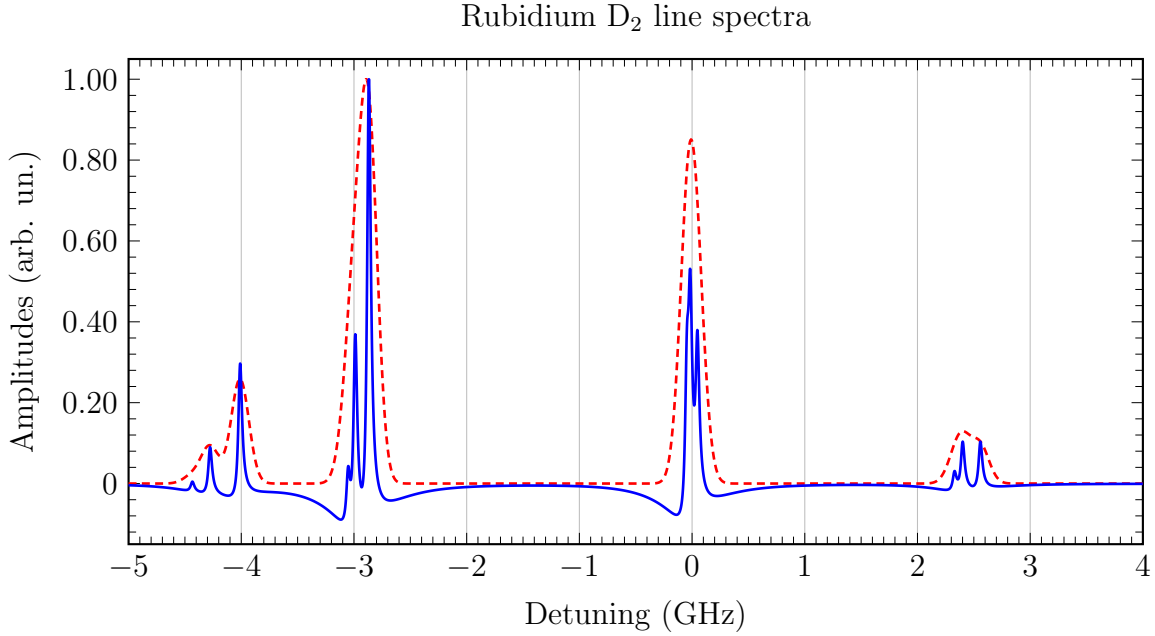

Figure 2.5: Blue solid line: theoretical D_2 line spectrum of natural Rb (72% of ^{85}Rb and 28% of ^{87}Rb) for $\ell = 350$ nm, $\gamma = 2\pi \cdot 20$ MHz and $\Theta = 130$ °C. Red dashed line: typical Doppler-broadened spectrum (Gaussian profile, $\Gamma_D = 2\pi \cdot 600$ MHz) recorded with cm-long cell.

To include this discussion in the calculation procedure, we should repeat the procedure described in section 2.2.1 over all the hyperfine transitions and make a summation to get the complete signal. Here-after we illustrate what can be obtained using the above-mentioned procedure applied in the case of Rb D_2 line. Figure 2.5 shows the theoretical Rb D_2 dSR spectrum, calculated for $\ell = 350$ nm, $\gamma = 2\pi \cdot 40$ MHz and $\Theta = 130$ °C, along with a typical Doppler-broadened spectrum (Gaussian profile, $\Gamma_D = 2\pi \cdot 500$ MHz) recorded in similar conditions with a cm-long cell, see formula 1.12. In contrast to the Doppler-broadened spectrum, hyperfine transitions are resolved in the dSR spectrum.

2.3 Experimental study

We present in this section some experimental results obtained by selective reflection monitoring of nanocells. Particularly, we present the general experimental assembly allowing to perform sub-Doppler spectroscopy of alkali vapors confined in NC. Besides, we show that the cell thickness can be measured accurately using an intereferometric method making use of the Fabry-Pérot nature of the nanocell. The selective reflection technique is implemented for studies of the Rb D_1 and D_2 lines to make qualitative comparison with the widely used saturated absorption technique and evaluate the consistency of the experimental results with the theoretical model presented in 2.1. We also study the influence of a Ne buffer gas on SR spectra of Rb D_2 lines. At last, we show that the SR technique is very convenient to study atom-surface interaction, when the cell thickness is much smaller than the radiation wavelength: $\lambda/13 \leqslant \ell \leqslant \lambda/7$.

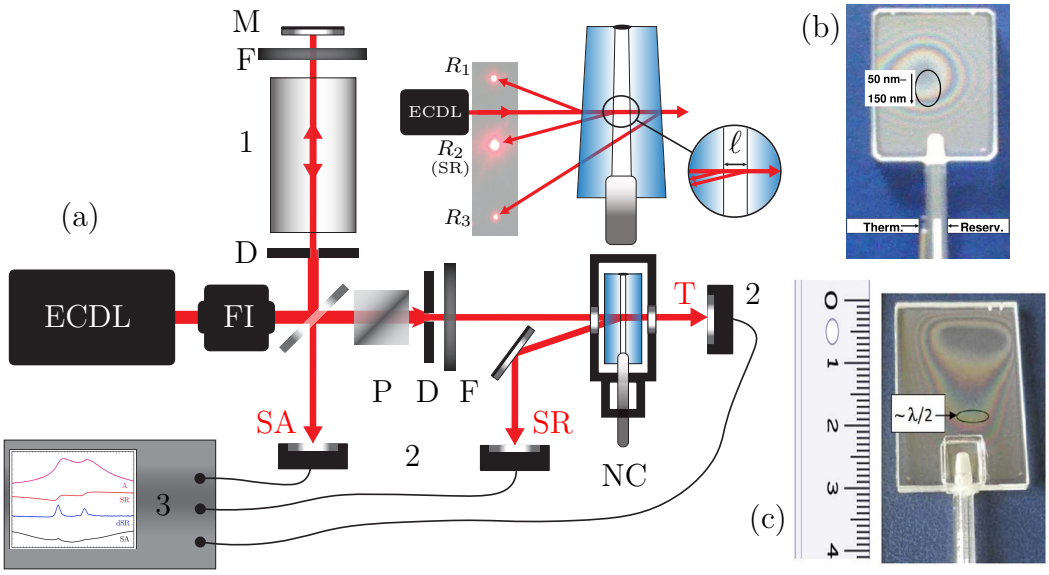

Figure 2.6: (a) Layout of the experimental setup: ECDL – cw tunable extended cavity diode laser, FI – Faraday insulator, NC – nanocell in the oven, 1 – frequency reference cm-long cell, 2 – photodetectors, 3 – oscilloscope, P – polarizer, D – diaphragm, F – filter, SR – selective reflection channel, SA – saturated absorption channel, T – transmission channel. The inset shows the geometry of three reflected beams from the NC; the selective reflection beam propagates in the direction of R_2. (b) Photograph of a K-filled nanocell; the oval marks the region 50 – 150 nm thickness. (c) Photograph of a Rb-filled nanocell where the region $\ell \sim \lambda/2$ is marked. The cm-graduated ruler on the side roughly gives the size of the NC.

2.3.1 Experimental consideration

Typical experimental setup

The scheme of a typical experimental setup is shown in Fig. 2.6. A VitaWave© continuous wave extended cavity diode laser outputting a power of several mW and having a spectral

linewidth about one MHz is used to scan the radiation frequency across alkali D line resonances. Depending on which species the NC is filled with, different lasers (wavelengths) have to be used: for example $\lambda_{D_1}^{Rb} = 795$ nm, $\lambda_{D_2}^{Rb} = 780$ nm; $\lambda_{D_1}^{K} = 770$ nm, $\lambda_{D_2}^{K} = 767$ nm. A Faraday insulator is used to prevent any laser radiation feedback into the cavity. The light polarization is refined using a polarizer, linearly-polarizing the incident laser light. To prevent shinning a large area on the cell (*i.e.* simultaneous action on different thickness regions), the laser beam diameter has to be lowered down to about 1 mm with the help of a diaphragm while keeping an acceptable signal-to-noise ratio. The inset of Fig 2.6(a) shows the geometry of the three beams reflected from the NC, where SR is the beam selectively reflected from the interface between the windows and the atomic vapor; it propagates in the direction of R_2. For the selective reflection to be spectrally narrow, the laser radiation should be directed as close as possible to the normal incidence on the NC's window [62]. A fraction of the laser radiation is guided to a unit forming a saturated absorption-based frequency reference from a 3 cm-long cell filled with the same alkali as the NC [63]. The SR, SA and transmission (T) radiations are recorded by sensitive photodiodes, outputting amplified signals fed to a four-channel Tektronix oscilloscope. To separate the selective reflection signal from ambient noise, an interference filter can be used.

The NC is placed in a two-chamber oven allowing to heat it up to 400 °C and to reach number densities up to $N \sim 10^{17}$ cm^{-3}. Indeed, due to the small size of the gap between the windows, we need to heat the reservoir of the cell, containing the liquid alkali metal to a temperature $\Theta_r > 100$ °C in order to be able to record atomic signal. To prevent condensation of the vapor on the windows, one should always make sure that the temperature at the windows is at least 20 °C higher than that on the sidearm: $\Theta_w > \Theta_r + 20$ °C.

Measurement of NC's thickness

In section 2.2 we have shown a strong dependence of the SR profile on the cell thickness, and thus it is extremely important to know precisely the thickness of the cell we are shinning the laser on in the experiments. As noted before, the NC behave like a low finesse Fabry-Pérot etalon, and we can thus use this property to determine accurately the thickness ℓ of the cell [64].

Let us come back to Eq. 2.14, which shows that, when the cell is empty or when the laser is far-detuned from atomic resonances ($E_r'' = 0$), the reflected intensity (of the beam R_2) depends on the cell thickness such that

$$\mathcal{I}_{R_2} \equiv \frac{1}{2}\epsilon_0 c|E_r'|^2 = \frac{1}{2}\epsilon_0 c\frac{2r_w^2}{|Q|^2}\left[1-\cos(2k\ell)\right]E_i^2, \tag{2.53}$$

with $|Q|^2 = 1+r_w^2\left[r_w^2 - 2\cos(2k\ell)\right]$. Thus, for a given wavelength of the laser, the thickness of the cell can be extracted by measuring $\mathcal{I}_{R_2}$. However, let us note that to avoid problems imposed by to laser power fluctuations, it is judicious to measure the ratio of $\mathcal{I}_{R_2}$ to the intensity of the beam reflected from the front window $\mathcal{I}_{R_1}$ rather than only $\mathcal{I}_{R_2}$. The etalon curve for the intensity ratio versus the cell thickness will follow

$$\frac{\mathcal{I}_{R_2}}{\mathcal{I}_{R_1}} = \frac{(1-R)^2}{R}\cdot\frac{F\sin^2(2\pi\ell/\lambda)}{1+F\sin^2(2\pi\ell/\lambda)}, \tag{2.54}$$

where $R = r_w^2$ is the reflection coefficient of the cell (in intensity) and $F = 4R/(1-R)^2$. To obtain Eq. 2.54, we have divided 2.53 by $\mathcal{I}_{R_1} = 1/2\cdot\epsilon_0 cRE_i^2$, noting that $\cos(2k\ell) = 1-2\sin^2(k\ell)$.

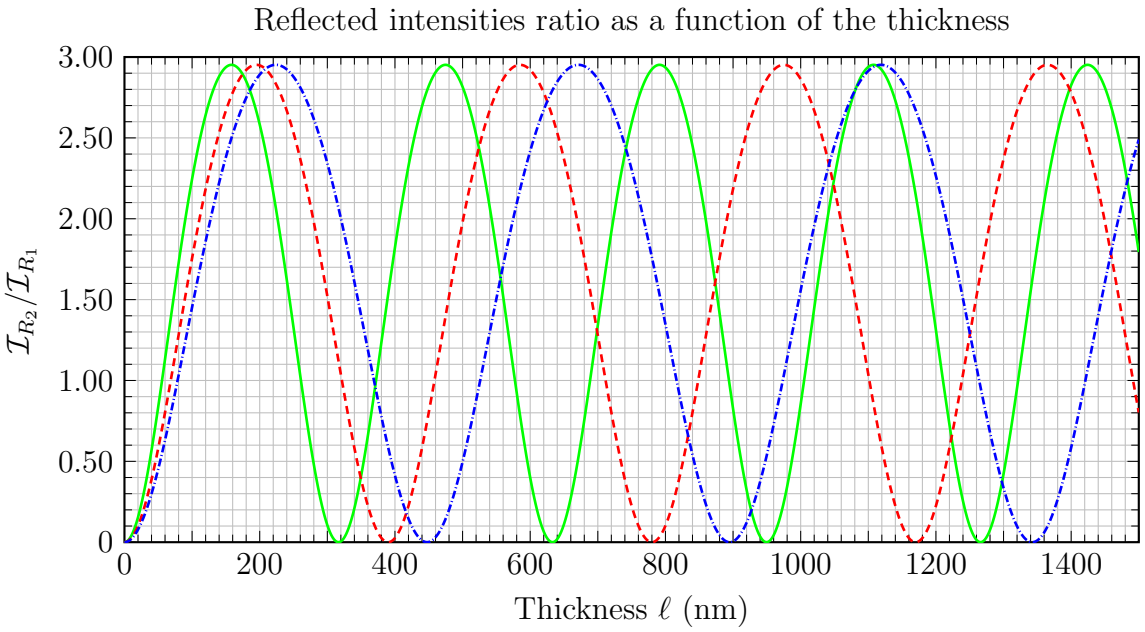

Figure 2.7: Evolution of the ratio $\mathcal{I}_{R_2}/\mathcal{I}_{R_1}$ versus the cell thickness for the wavelengths $\lambda =$ 633 nm (green solid line), $\lambda = 795$ nm (red dashed line) and $\lambda = 895$ nm (blue dash-dotted line) plotted using formula 2.54. These wavelengths respectively correspond to He-Ne, Rb D_2 and Cs D_1 resonances for which sources are available at our laboratory.

Figure 2.7 shows the evolution of the ratio $\mathcal{I}_{R_2}/\mathcal{I}_{R_1}$ when the cell thickness varies in the range 0 – 1300 nm for the wavelengths $\lambda = 633$ nm (green solid line), $\lambda = 795$ nm (red dashed line) and $\lambda = 895$ nm (blue dash-dotted line). On this figure, one can see that the value of the ratio oscillates between 0 (destructive interference) and 2.9 (constructive interference) versus the cell thickness. Indeed, formula 2.54 predicts an oscillation of the ratio with a periodicity of $\ell = m\lambda/2$, where m is an integer.

A consequence of this non one-to-one correspondence is, from a practical point of view, that the thickness cannot be measured with a single evaluation of the ratio. One can note two solutions to this problem: (*i*) using another laser having a different wavelength but his technique requires to have perfect alignment of both beams, see Dutier's thesis (2003) [65, section 2.4]; (*ii*) keeping the cell at a known position, that is to say an incidence point where ℓ is known, then the value of the thickness can be followed with a smooth and slow translation of the cell until the desired position is reached. Particularly, the NCs are made such that there is almost an optical contact, where the thickness is much less than $\lambda/4$. This point can be easily identified when looking at the NC, see the dark central halo on NC pictures of Fig 2.6(b) and (c). Let us note that in this discussion we have neglected possible losses of light by diffusion, absorption, etc. such that $R + T = 1$. Some small losses, for example non-perfect extinction at $\ell = m\lambda/2$, are attributed to the roughness of the windows' surfaces; the roughness is still smaller than $\lambda/10$.

2.3.2 Selective reflection spectroscopy of Rb D_1 and D_2 line

We want to study the natural Rb D_1 and D_2 lines using the selective reflection from a NC. As the resonance frequencies for both of these lines are known with a great accuracy, we should be able to evaluate the consistency of the theoretical model presented in section 2.1 with experimental results. Particularly, we would like to see if the predicted oscillations of the sign of dSR signals are observed.

(a) Rb D_1 line levels and transitions diagram

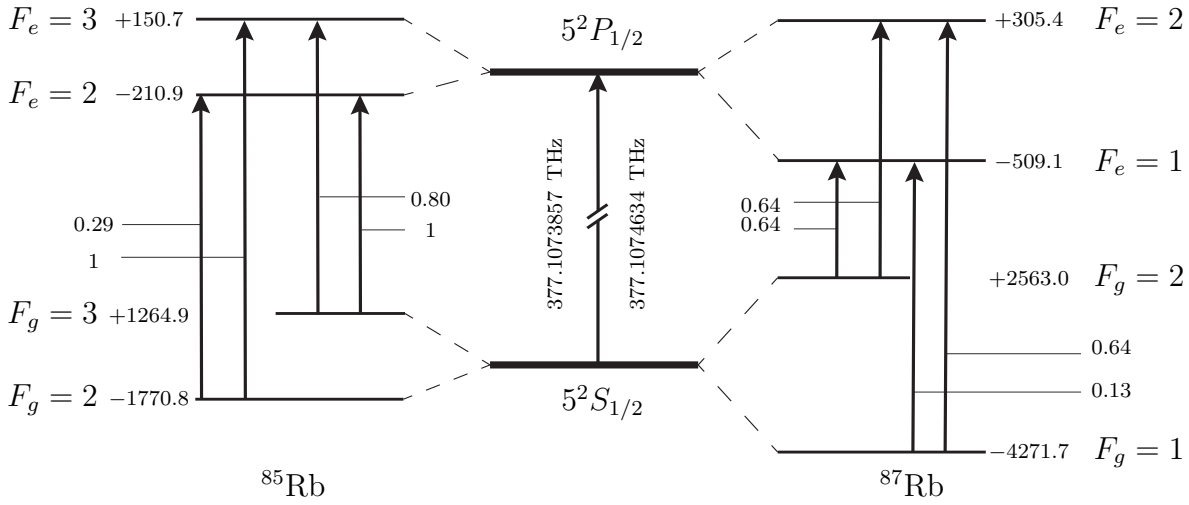

(b) Rb D_2 line levels and transitions diagram

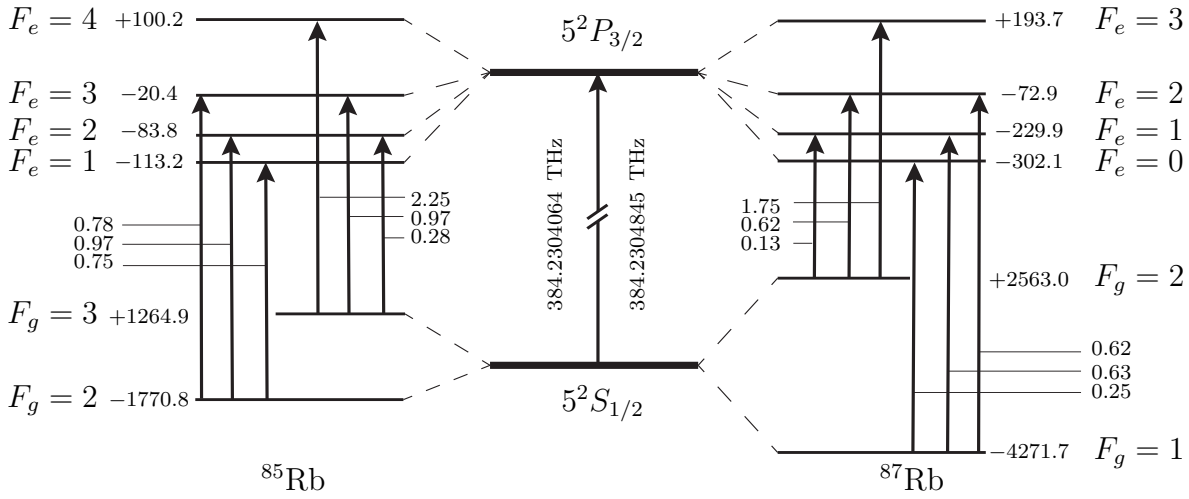

Figure 2.8: (a) Rubidium D_1 line and (b) Rb D_2 line levels and transitions diagram. The numbers near the levels are the frequency shifts with respect to the fine structure levels: $5S_{1/2}$ for the ground states, $5P_{1/2}$ (a) and $5P_{3/2}$ (b) for the excited states. Optical transitions are marked by arrows, and the nearby numbers correspond to the relative transition probabilities.

The saturated absorption is one of the most widely used technique to form sub-Doppler resonances, see section 1.2.2. In this technique, sub-Doppler resolution is attained by the formation of atomic velocity-selective optical pumping (VSOP) resonances. In the experimental realization, the laser beam is split in two components: a high-power ($\sim$ 2 mW) pump beam and a counter-propagating weak probe beam with much lower power. Due to the Doppler effect, only the group of atoms flying in the cell with velocities perpendicular to laser beams simultaneously experiences interaction with both pump and probe beams. As a consequence of the pumping, the population of the absorbing level decreases, which is then detected by the probe radiation. In this way, narrow VSOPs with a spectral linewidth close to the natural one are formed along with strong cross-over (CO) resonances which, as a rule, only complicate the spectrum. Another disadvantage of the SA method is that VSOP amplitudes do not correspond to atomic transition probabilities. Thus, for possible applications such as frequency markers, it is interesting to make a qualitative comparison between the dSR and the SA methods, and find optimum experimental parameters.

Rubidium D_1 line

The experimental setup presented on figure 2.6 with a laser, whose wavelength is equal to 795 nm, resonant with the D_1 line transitions of Rb, was used to record the following SR and dSR curves. Figure 2.9 shows the selective reflection spectrum and its derivative for all transitions between hyperfine levels of the D_1 line of ^{85}Rb and ^{87}Rb atoms which are shown in Fig. 2.8(a). One can see that the amplitudes of the dSR peaks exactly correspond to the probabilities presented in the transitions diagram. Let us note that this proportionality to the oscillator strengths is invalid for Faraday rotation spectra recorded from NC [66], as well as for spectra recorded with the widely used saturated absorption technique.

Owing to this important feature of selective reflection and because the derivative of selective reflection signals are narrow ($\sim$ 40 MHz) and located exactly at atomic transitions, confirmed by the velocity selective optical pumping frequency reference, the dSR signals can thus be used as appropriate identifiers of atomic transitions. The analysis of selective reflection spectra at various temperatures of the nanocell ranging from 110 to 205 °C (corresponding to the number densities of 1×10^{13} to 7×10^{14} cm^{-3}), has shown that the spectrum is broadened while having an increased amplitude. The optimal (compromised) parameters are reached in the range of $\Theta_r \sim 130 - 140$ °C.

Rubidium D_2 line

We now use a laser whose wavelength $\lambda = 780$ nm is resonant with the D_2 line transitions of Rb. Figure 2.11 shows experimental (red dots) and theoretical dSR spectra (blue solid lines) for thicknesses $\ell \approx 500$ nm $> \lambda/2$ (panels (a) and (b)) and $\ell \approx 300$ nm $< \lambda/2$ (panels (c) and (d)) for ^{85}Rb D_2 line. The energy levels involved in the transitions $F_g = 2, 3 \rightarrow F_e = 1, 2, 3, 4$ are shown in the inset of Fig. 2.8(b). A sign oscillation of the dSR spectra can be observed, which is well described by the theoretical model. One can see that all the six atomic transitions are well resolved, the signal-to-noise ratio is exceeding 30.

The dSR FWHM linewidth is 30 – 40 MHz when the reservoir temperature $\Theta_r \sim 110$ °C.

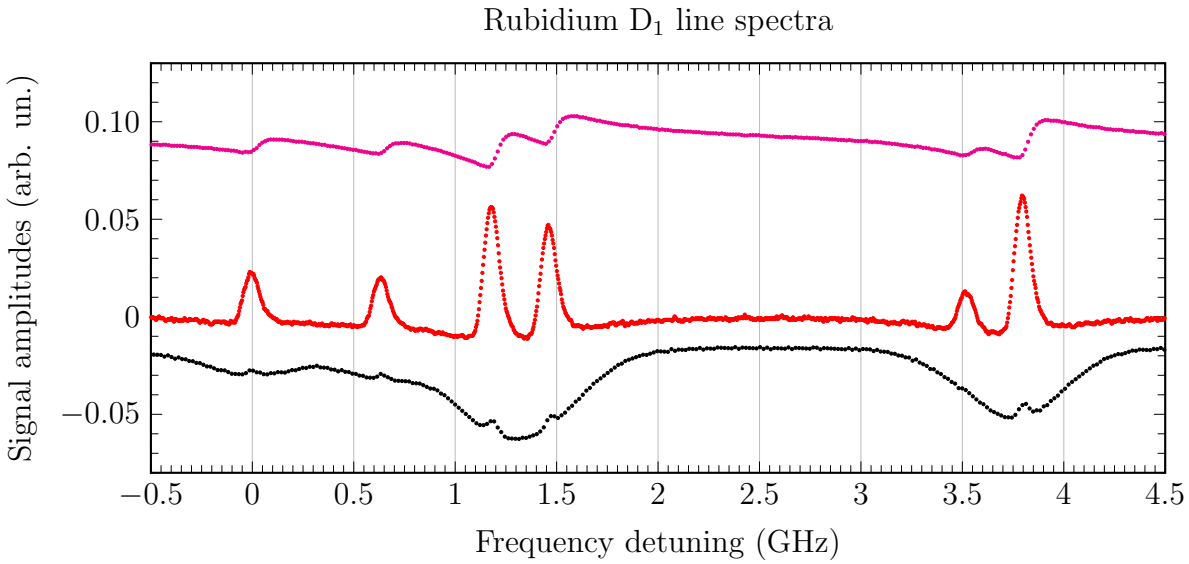

Figure 2.9: Selective reflection spectrum (magenta dots) and its derivative (red dots) for all hyperfine transitions of Rb D_1 line (see Fig. 2.8(a)) at $\ell \approx 368$ nm. The power of laser radiation is below 0.1 mW. The lower line is a velocity selective optical pumping spectrum serving as a frequency reference.

This is more than 15 times smaller than the Doppler width of atomic transitions of Rb in a usual 1-cm long cell: the Doppler width of an individual transition in a Rb atom at this temperature is approximately 600 MHz. One can see that all the transitions are completely resolved. For the theoretical curves, we have set the homogeneous width 35 MHz including the natural width of the atomic transition (about 6 MHz for Rb atoms), the collisional width of atoms colliding with sapphire windows of the NC which is about 10 MHz for thicknesses $\ell \leqslant 300$ nm, and the residual Doppler width ~ 20 MHz. The dSR power broadening due to the 20 μW laser power was less than 1 MHz. However, as the laser power was increased up to 2 mW, the dSR signal broadened for an additional 10 MHz.

Figures 2.11 (e) and (f) show the reference spectra formed by the SA method. The comparison of the dSR amplitudes for $F_g = 3 \to F_e = 4$ and $F_g = 3 \to F_e = 3$ transitions presented in Fig. 2.11(a) both experimentally and theoretically is consistent with the ratio $2.25/0.97 \approx 2.3$ of the relative probabilities of these transitions presented in the transition diagram of Fig. 2.8(b), whereas this ratio for the SA spectrum is smaller than unity. Similarly, the comparison of the dSR amplitudes for the transitions $F_g = 3 \to F_e = 4$ and $F_g = 3 \to F_e = 2$ yields in both experiments and theory a consistent ratio of $2.25/0.28 \approx 8$ for these transition probabilities, whereas this ratio in the SA spectrum slightly exceeds 1. Besides, the SA spectrum exhibits strong CO resonances which, as a rule, only complicate the spectrum and do not carry any additional information. Therefore the dSR is advantageous for the correspondence between transition amplitudes and probabilities, which is important for atomic transition markers. Futhermore, the advantage of the dSR method over the SA method is especially evident when the frequency distance between the upper levels is small, as for the transitions $F_g = 2 \to F_e = 1, 2, 3$ (see the rigth panels of Fig. 2.11). In the SA spectrum, strong CO resonances overlap with useful VSOPs, severely

complicating their identification. Noteworthy, Sargsyan *et al.* (2014) [67] have shown that the use of a microcell with thickness $\ell \approx 30 - 40$ μm excludes the formation of CO resonances.

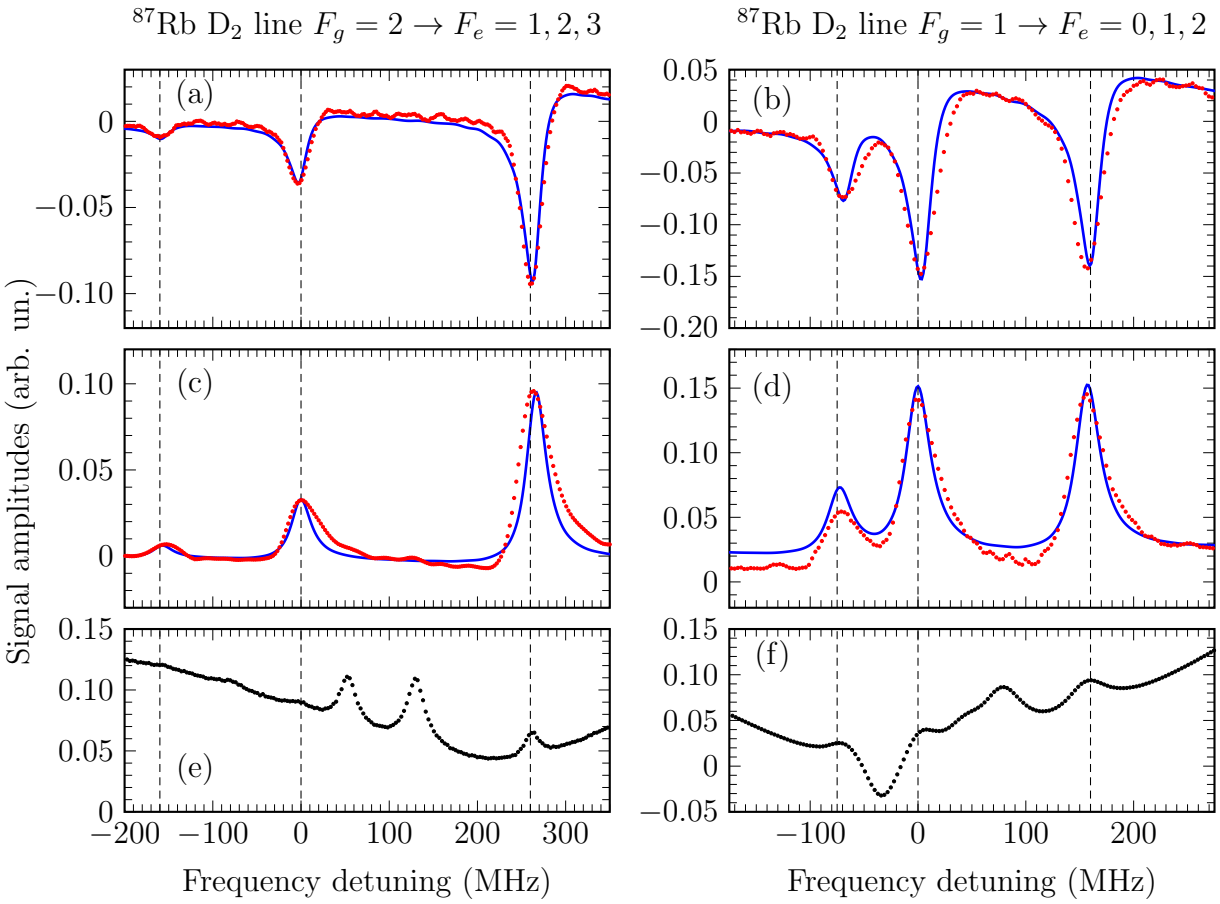

Figure 2.10: Experimental (red dots) and theoretical (blue solid lines) dSR spectra for $\ell \approx$ 500 nm (a,b) and $\ell \approx$ 300 nm (c,d) for ^{87}Rb D$_2$ line $F_g = 2 \to F_e = 1, 2, 3$ transitions (left panels) and $F_g = 1 \to F_e = 0, 1, 2$ transitions (right panels). The lower black curves (e) and (f) are the corresponding reference SA spectra. The advantage of the dSR method is evident when comparing panels (d) with (f) because strong CO resonances overlap with useful VSOPs preventing easy identification.

The spectral linewidth of the dSR signal for $\ell \approx 500$ nm is about 35 MHz, which is narrower than that for $\ell \approx 300$ nm (about 40 MHz). This is explained by the fact that the time of flight $\tau = \ell / v_z$ between NC's windows decreases when decreasing the thickness for atoms with the thermal velocity projection v_z along the laser beam. This leads to more frequent collisions of atoms with the windows, resulting in the broadening of the dSR spectrum; the broadening is especially evident for thicknesses about 120 nm achieving 120 MHz, see paragraph 2.3.4). Therefore, when it is necessary to have the minimal dSR signal width, a NC with $\ell \sim 500$ nm is preferable.

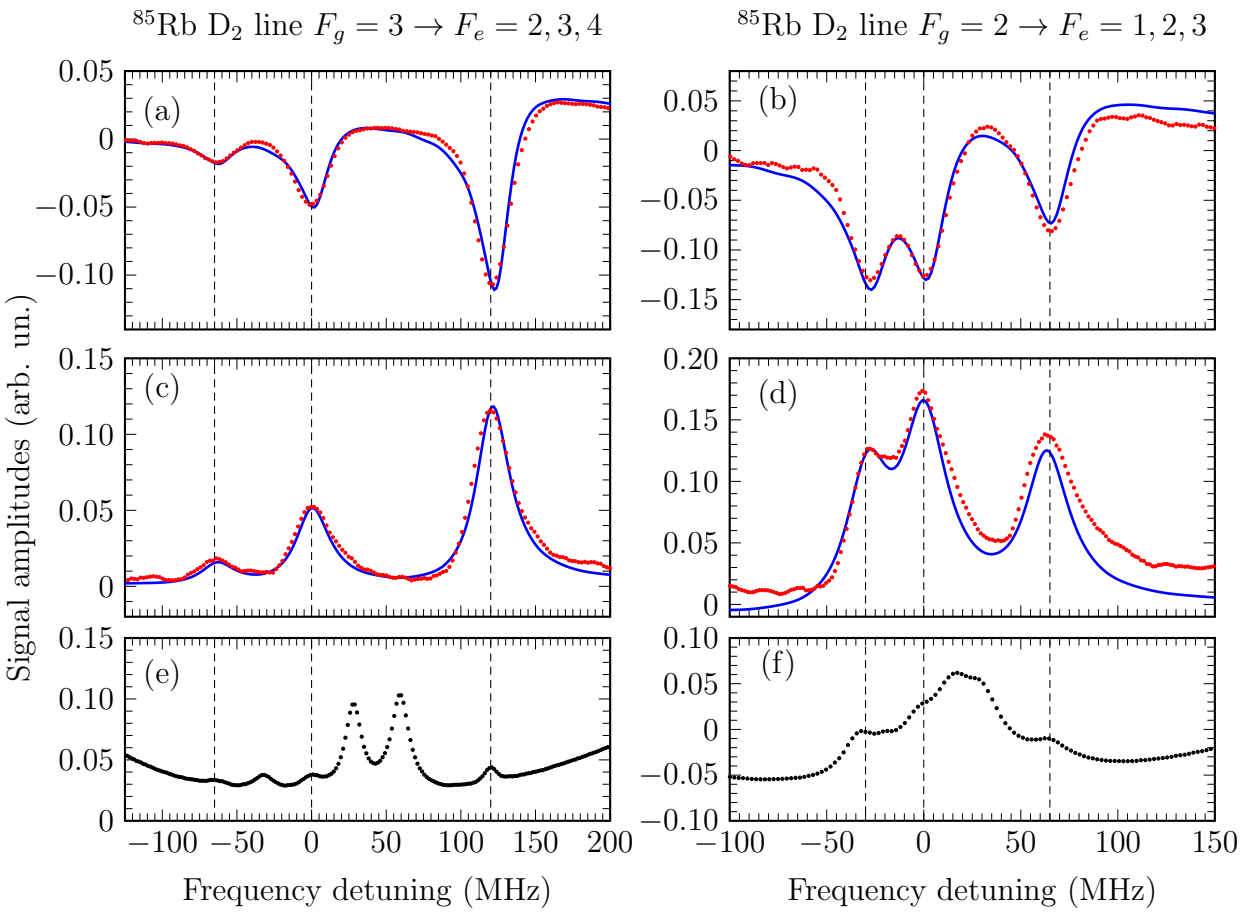

Figure 2.11: Experimental (red dots) and theoretical (blue lines) dSR spectra for the thicknesses $\ell \approx 500$ nm (a,b) and $\ell \approx 300$ nm (c,d) for ^{85}Rb D$_2$ line $F_g = 3 \rightarrow F_e = 2, 3, 4$ transitions (left panels) and $F_g = 2 \rightarrow F_e = 1, 2, 3$ transitions (right panels), for the laser power $P_L \sim 20$ µW. The lower curves (e) and (f) are the corresponding frequency reference SA spectra. The advantage of the dSR method over SA is evident when comparing panel (d) with (f), where strong CO resonances overlap with the VSOPs indicating atomic transitions.

2.3.3 Influence of Ne buffer gas on Rb D$_2$ line

It is known that the presence of some residual (buffer) gas in a cell at a pressure above 0.1 Torr leads to the complete disappearance of VSOPs, see for example [68]. In this paragraph, we study the influence of a buffer gas on the dSR spectrum using a two-region Rb-filled vapors cell containing Ne buffer gas at a 6 Torr pressure. This cell consists of two communicating chambers: a nanocell located in the upper part of the assembly and a convenient 1 cm-cell located in the middle part, see [69]. Both parts are connected through a sapphire tube and therefore both contain Ne-buffed Rb vapors. As resonances are absent in the SA spectrum when the buffer gas pressure is above 0.1 Torr, the SA reference spectra presented here-below was obtained using a cell with pure Rb vapor.

Figure 2.12 shows experimental and theoretical dSR spectra recorded from the nanocell of

the combined cell for $\ell \approx 300$ nm for the ^{85}Rb D_2 line transitions $F_g = 3 \to F_e = 2, 3, 4$ and ^{87}Rb D_2 line transitions $F_g = 2 \to F_e = 1, 2, 3$ transitions. One can see from Fig. 2.12 that the three distinct atomic transitions in the dSR spectra demonstrate an additional broadening caused by collisions of Rb and Ne atoms. Theoretical curves calculated for ^{85}Rb and ^{87}Rb atoms (D_2 line), with the fitted broadening parameter $\gamma = 2\pi \cdot 45$ MHz, well describe the experiments. Therefore, the broadening caused by Rb-Ne collisions leads to the same broadening of 10 MHz/Torr. This is quite consistent with the width of the fluorescence spectrum from a NC measured by Hakhumyan *et al.* (2010) [69]. In this article, the width of the fluorescence spectrum from a pure Rb vapor measured for ℓ around 400 nm was about 85 MHz. The narrower (about 2.5 times) dSR spectrum along with the Rb-Ne collision spectral broadening allowed the measurement of a small red frequency shift of about 2 MHz/Torr. As a rule, and in addition to spectral broadening, collisions of alkali atoms with different buffer gases cause a red frequency shift about 10 – 30% of the broadening value [70].

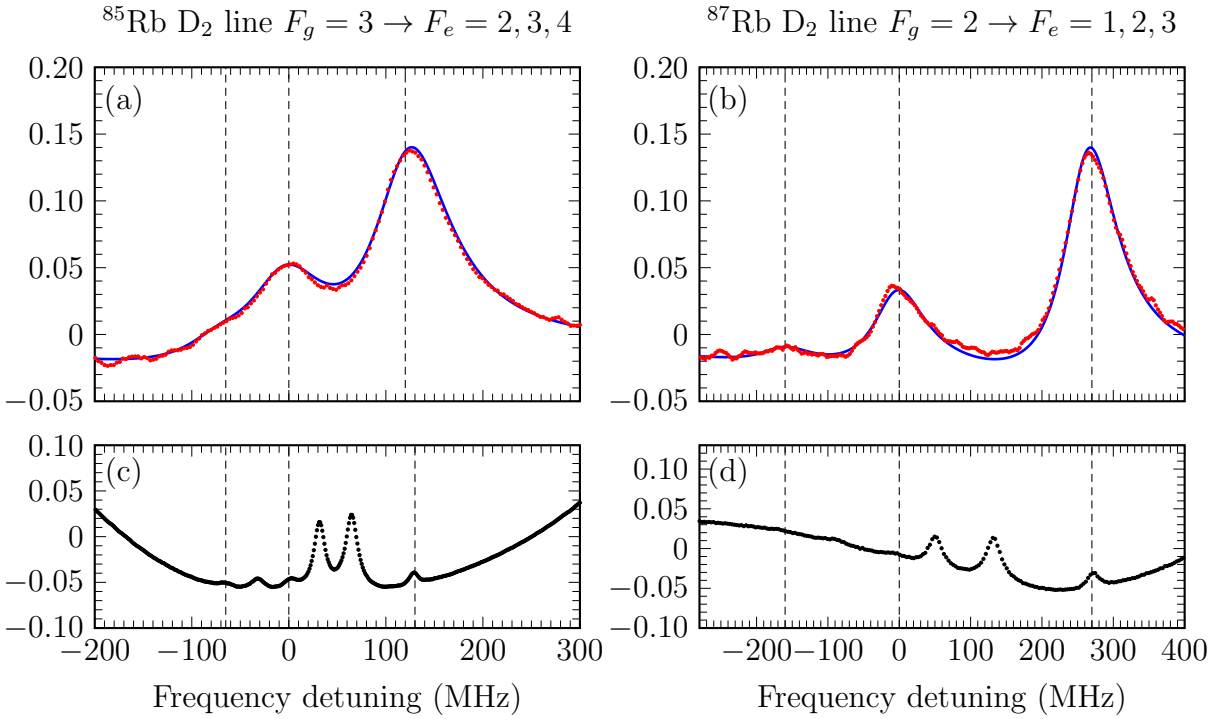

Figure 2.12: Experimental (red dots) and theoretical (blue solid lines) dSR spectra for (a) ^{85}Rb D_2 line $F_g = 3 \to F_e = 2, 3, 4$ transitions and (b) ^{87}Rb D_2 line $F_g = 2 \to F_e = 1, 2, 3$ transitions in the presence of 6 Torr Ne buffer gas. The calculations were performed for $\ell = 300$ nm and $\gamma = 2\pi \cdot 45$ MHz. The lower black solid lines are the corresponding reference SA spectra recorded from a pure Rb vapor cell.

2.3.4 Van der Waals effect on K D_2 line

For numerous applications, it is important to reduce the dimensions of the cell containing atomic vapor [71], thus reaching the scale where the proximity of the atoms to the cell's surface be-

comes significant. Hence, a thorough understanding of the atom-surface interactions is essential. Many of the applications use atoms in ground states, where atom-surface (AS) interactions are relatively small as the induced dipole is only a few Debye. However, AS interactions can still have a significant effect if the surface is located near the atom, that is less than typically 100 nm (see [72] and refs. therein). In this regime, the AS potential is governed by an inverse power law $U_{\mathrm{vdW}} = -C_\alpha z^{-\alpha}$, where C_α is the coupling coefficient and z is the atom-surface distance. For an uncharged surface one expects the van der Waals (vdW) interaction with $\alpha = 3$ in the regime $z < \lambda/2\pi \approx 120$ nm [73, 74], where $\lambda = 767$ nm is the transition wavelenght. Note that in the regime $z > \lambda/2\pi$, the AS interaction is described by the Casimir-Podler interaction with $\alpha = 4$ [75, 76].

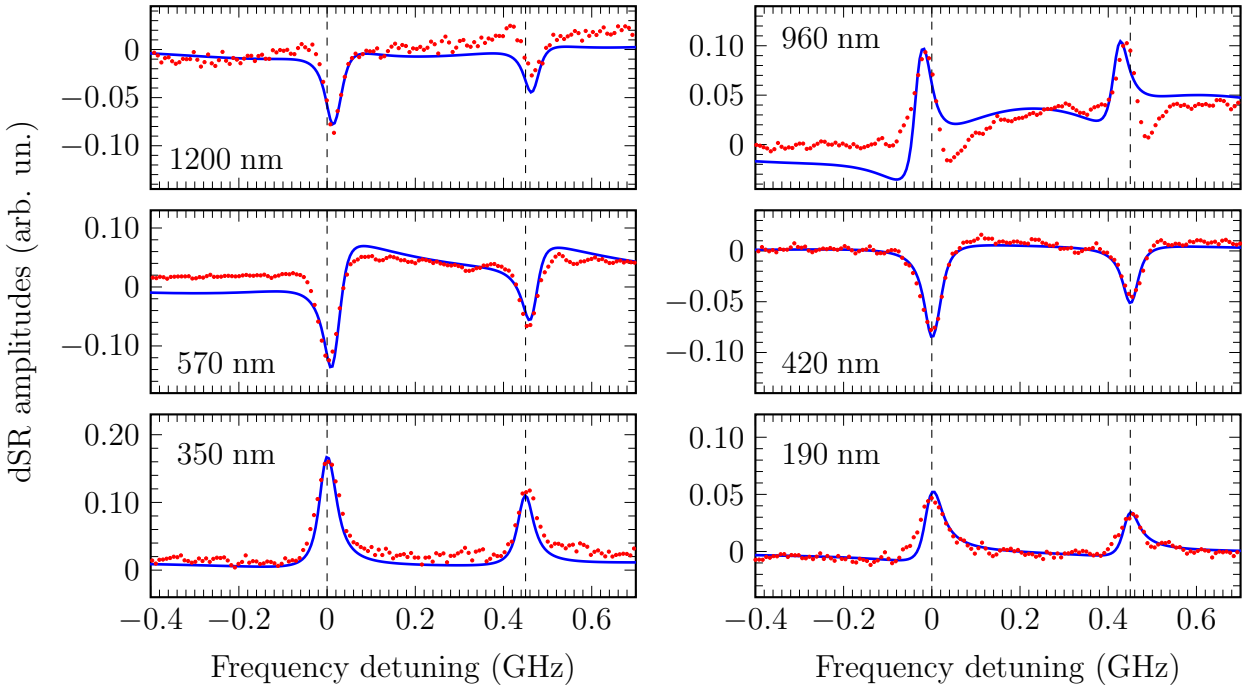

Figure 2.13: ^{39}K D_2 line spectra as a function of the nanocell thickness. The experimental results for $\Theta_r = 190$ °C, $P \sim 0.2$ mW are shown with red dots; the corresponding theoretical curves are the blue solid lines. Oscillations of the dSR sign are observed: it is positive for $\ell = 190,\ 350$ and 960 nm, while negative for $\ell = 420,\ 570$ and 1200 nm. The theory coincides well with the experiment.

Some works have demonstrated that NCs filled with alkali metal vapors serve as very convenient tools for alkali atom-surface studies using resonant absorption and fluorescence processes [16, 40, 72, 74, 77, 78, 79]. The NC is constructed such that the gap between the inner surfaces of the windows has a wedged form, thus the vapor column length ℓ can be varied smoothly in the range 50 – 1500 nm with a simple vertical translation. Consequently, atoms inside the gap are located very close to the surface of the NC's dielectric windows. The nanocell brings several benefits such as: (i) a smooth translation of the laser beam in the vertical direction allows tunable in distance atom-surface interactions studies; (ii) when $\ell \sim 50$ nm, the efficiency of optical processes (e.g. absorption, fluorescence, selective reflection, etc.) is strongly reduced,

thus it is important to be able to increase the number density of the vapor which can be done by increasing the temperature of the NC's sidearm. The temperature can be increased up to 500 °C without any chemical reactions of hot alkali vapors with the sapphire windows of the NC. Note that in the case of glass cells, a strong chemical reaction at ~ 150 °C causes a blackening of the cell's windows, making them opaque to the laser radiation.

It is important to note that in order to obtain a detectable optical process signal when $\ell < 100$ nm, the potassium number density must be above 10^{13} cm^{-3}, which means that the temperature of the NC's reservoir must be above 150 °C, while the temperature at the windows must remain 20 °C higher in order to prevent condensation of the K vapor on the windows. That is why the NC filled with potassium vapor is ideal for atom-surface interaction study.

In Fig. 2.13, we present the evolution of dSR spectra when the NC thickness varies from 190 to 1200 nm, for the reservoir temperature $\Theta_r = 190$ °C and a laser power $P \sim 0.2$ mW. On this figure, we have superimposed the theoretical curves (blue solid lines) on the top of the experimental results (red dots). A similar situation to that obtained for Rb D_1 line [43] is observed: a small deviation from the thickness $\ell = \lambda/2 = 384$ nm leads to a sign reversal of the dSR signal from negative for $\ell > \lambda/2$ to positive for $\ell < \lambda/2$. The same behavior is also observed when the thickness varies from $\lambda/2 < \ell < \lambda$ and again when $\lambda < \ell < 1.5\lambda$. The predicted periodicity of the sign oscillation of $\lambda/2$ is thus verified experimentally over three periods. This result is consistent with previous results obtained for the Rb D_1 and D_2 lines [43, 46]. The small discrepancies seen between experiment and theory is due to the fact that the size of the homogeneous region (where ℓ is constant across the laser beam) gets smaller as the thickness is increased making the laser beam cover a larger range of thicknesses simultaneously.

For applications in laser spectroscopy, the most convenient method is the dSR when $\ell \sim \lambda/2$, which corresponds to the range 300 – 450 nm for K D_2 studies. The linewidth of dSR presented in Fig. 2.13 when $\ell = 350$ nm is ~ 50 MHz (FWHM). In this case, an 18 times smaller linewidth than the potassium Doppler width was acheived. Note that in [80] it was shown that with good experimental parameters ($\ell = 350$ nm, $\Theta_r = 150$ °C, $P \sim 0.1$ mW) the spectral linewidth of potassium D_1 line atomic transitions was reduced down to 30 MHz using the dSR technique.

As visible from Fig. 2.14(a), a decrease in ℓ leads to a red frequency shift (the frequency is decreasing, the wavelength is increasing) of the peak of the dSR profile and to a strong asymmetric broadening toward low frequencies which is caused by vdW interactions of atoms with the NC's windows. As one can expect, atomic transition frequencies of the dSR spectrum for $\ell = 350$ nm are unshifted when comparing with the SA frequency reference which is explained by a relatively large distance between atoms and NC's windows. Indeed, evidences of AS interactions for atomic $D_{1,2}$ lines of alkali metals are found only for thicknesses $\ell \leqslant 100$ nm, see for example [81]. For this reason, the atomic transition frequency shift is negligible for $\ell = 190$ nm since atoms are still at a relatively large distance from the windows. Meanwhile, for $\ell = 120,\ 100,\ 90,\ 80$ and 60 nm, red frequency shifts of atomic transition peaks are -20, -30, -45, -63 and -130 MHz, respectively. The thicknesses of the cell have been measured with a $\pm$ 5 nm accuracy, using the interferometric method presented in section 2.3.1.

To determine the value of the vdW interaction coefficient C_3 of potassium $4S_{1/2} \rightarrow 4P_{3/2}$ transitions with nanocell's sapphire windows, we present in Fig. 2.14(b) the frequency shifts with respect to the first window (w_1): $\Delta\nu_{\mathrm{vdW}} = -C_3 z_1^{-3}$ (red dashed line), and for the second window (w_2): $\Delta\nu_{\mathrm{vdW}} = -C_3 z_2^{-3}$ (blue dashed line), where z_1 and z_2 are the distances between

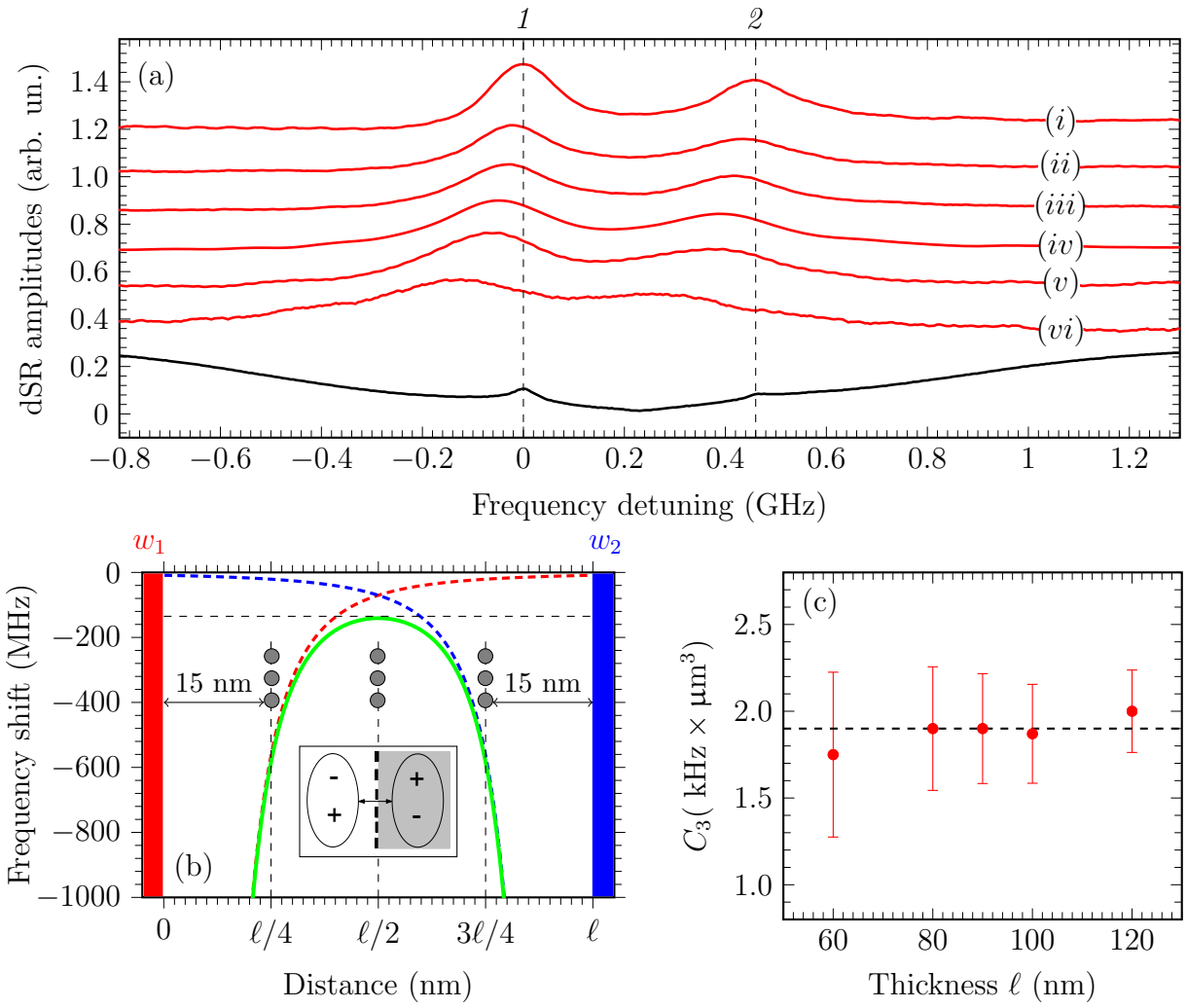

Figure 2.14: (a) Experimental ^{39}K D_2 line spectra as a function of the nanocell thickness, for a temperature $\Theta_r = 230$ °C and a laser power of 0.5 mW. (*i*) $\ell = 190 \pm 5$ nm: no frequency shift; (*ii*) $\ell = 120 \pm 5$ nm: -20 MHz shift; (*iii*) $\ell = 100 \pm 5$ nm: -30 MHz shift; (*iv*) $\ell = 90 \pm 5$ nm: -45 MHz shift; (*v*) $\ell = 80 \pm 5$ nm: -63 MHz shift and (*vi*) $\ell = 60 \pm 5$ nm: -130 MHz shift. The lower black solid line curve serves as a frequency reference: *1* corresponds to the group $F_g = 2 \rightarrow F_e = 1, 2, 3$ and *2* corresponds to the group $F_g = 1 \rightarrow F_e = 0, 1, 2$ of ^{39}K D_2 line. (b) Transition frequency shift versus atom-windows distance for the inter-window distance $\ell = 60$ nm. The red dashed line shows the red frequency shift caused by the first window (w_1) while the blue dashed one shows the one caused by the second window (w_2). The green solid line shows the total frequency shift caused by both windows simultaneously. The inset shows the sketch of an atom in the form of a dipole and its mirror image formed inside NC's dielectric windows. Potassium atoms located at the distance $z = 15,\ 30,\ 45$ nm from the windows are shown as gray-filled circles. (c) ^{39}K D_2 line vdW interaction coefficient C_3 as a function of the NC thickness. The horizontal dashed line follows $C_3 = 1.9$ kHz × μm^3.

a potassium atom with each windows (w_1) and (w_2) respectively [72]. The total frequency shift (green solid line) is the sum both of contributions, which can be expressed as

$$\Delta\nu_{\mathrm{vdW}} = -\frac{C_3}{z^3} - \frac{C_3}{(\ell - z)^3}. \tag{2.55}$$

As is seen from Eq. (2.55), the total frequency shift caused by the influence of both windows for atoms located at the center of the NC, that is $z = \ell/2$, reads

$$\Delta\nu_{\mathrm{vdW}} = -16C_3\ell^{-3}. \tag{2.56}$$

From Fig 2.14(b), one can see that the frequency shift of all atoms located at a distance $z = \ell/2 \pm 5$ nm from the windows is ~ 30 MHz, close to the overall frequency shift at $z = \ell/2$ (for $\ell = 60$ nm). Meanwhile, the frequency shift of the atoms located at a distance $z = \ell/4 \pm 5$ nm (or $z = 3\ell/4 \pm 5$ nm) from the windows is larger by a few orders of magnitude (close to the frequency shift reached at $z = \ell/4$). Particularly, the red frequency shift experienced by atoms located at the distance $z = \ell/4 - 5$ nm (or $z = 3\ell/4 - 5$ nm) reaches ~ 3 GHz. As a consequence, the spectral density of selective reflection signal is maximal for the atoms located near $z = \ell/2$ (center of the NC). Therefore the peak of the dSR signal spectrum at any thickness $\ell \leqslant 100$ nm will be located where the frequency shift modulus is minimal, see Fig. 2.14(b). Using the frequency shift values of the dSR signal peaks with $N_{\mathrm{K}} \sim 4 \times 10^{14}$ cm^{-3} for various thicknesses (see Fig. 2.14(a)) and Eq. 2.56, we have calculated the C_3 coefficient of the vdW interaction coefficient values, presented in Fig. 2.14(c). Thus, we measure $C_3 = 1.9 \pm 0.3$ kHz $\times$ μm^3 for the vdW interaction coefficient between ^{39}K D_2 line transition dipole moments with NC's sapphire windows. It it worth to note that this value is close to that obtained for Cs D_1 line transitions [78]. The inaccuracy in the determination of the C_3 coefficient arises from the inaccuracy in determining the thickness of the nanocell.

As already noted in [17], for nanocell thicknesses $\ell > 200$ nm, the obtained spectrum broadens strongly for both D_1 and D_2 lines when increasing the temperature of the nanocell's reservoir because of Rb – Rb interaction, while not inducing any transition frequency shift. The situation for $\ell < 100$ nm is significantly different: as the temperature increases from 170 to 210 °C, an additional red frequency shift to the vdW, the cooperative Lamb shift, has been observed. In order to measure a pure vdW interaction one has to minimize the influence of the Rb – Rb interaction; thus, it is preferable to measure the red shift of the dSR signal peak at low densities, where the condition $Nk^{-3} \ll 1$ is fulfilled. This condition remains fulfilled as long as $\Theta_r \leqslant 160$ °C (that is $N_{\mathrm{K}} = 2 \times 10^{13}$ cm^{-3}). However, a decrease in the temperature at 60 – 90 nm strongly degrades the signal-to-noise ratio and, by extension, the accuracy of determining the position of the dSR signal peak. At 160 °C, the red shift decreases by approximately 10%. Fortunately, the coefficient C_3 is linearly proportional to the measured frequency shift, thus also the related correction for the coefficient C_3 and is smaller than the error given in this work.

Note that the behavior of atomic transition frequencies when the potassium vapor density increases under the rigid spatial confinement by the windows of the nanocell is being actively studied, since new specific features have been revealed. For example, the following unusual behavior of the D_2 line frequency of the atomic transition of potassium at a NC thickness $\ell = 490$ nm was revealed in a recent work [82]: a blue frequency shift was detected when the K

vapor density was increased such that $N_{\mathrm{K}}k^{-3} \sim 1$; the frequency shift became zero with further increase of the number density (such that $N_{\mathrm{K}}k^{-3} \sim 100$).

Summary

In this chapter, we have presented a theoretical model describing the interaction of a low-power laser beam with a dilute alkali vapor contained in a NC. Numerical simulations have suggested to use the selectively reflected beam from the NC rather than the transmitted one as the selective reflection exhibit stronger line narrowing, even when the Dicke effect occurs for the transmitted beam. The model predicts, in addition, an oscillation of the dSR profile with a periodicity of $\ell = m\lambda/2$.

In our experiments, we have investigated Rb D_1 and D_2 lines and have shown that the dSR from NCs yields narrow spectra allowing to record individually Rb hyperfine transitions. Besides, we have shown that dSR spectra are more convenient than that of SA due to the presence of CO resonances and lower contrast of hyperfine resonances in the case of saturated absorption. The oscillation of the dSR profile predicted by the model have been verified experimental using a K-filled NC. In addition, we have demonstrated the usefulness of the dSR technique to study atom-surface interactions and measured the interaction coefficient between ^{39}K D_2 line transition dipole moment with NC's sapphire windows to be $C_3 = 1.9 \pm 0.3$ kHz $\times$ μm^3.

The simplicity of the experimental implementation, large amplitude, and sub-Doppler width ($\sim$ 40 MHz) of a detected signal at an atomic transition frequency are appropriate for applications in metrology. In particular, selective reflection from nanocells is a convenient frequency marker of atomic transitions; in this case, peak amplitudes are proportional to the transition probabilities. Thanks to the small size of the atomic layer, the remote optical monitoring of a magnetic field with a nanometric spatial resolution should be possible on the basis of the splitting of selective reflection peaks in a magnetic field, which will be explored in the next chapter.

Chapter 3

Alkali vapors under magnetic field

Contents

Introduction

The presence of a magnetic field is known to split the spectral line of atoms in several components, as first observed in 1896 by P. Zeeman whose name was given to this famous effect. As the spectral lines split in components having, in general, different intensities, the Zeeman effect is often used to measure, for example, the magnetic field created by stars or involved plasma physics. Notable applications of the Zeeman effect includes laser cooling experiments [83], laser frequency stabilization [84], electron spin and nuclear magnetic resonance spectroscopy [85, 86] or single photon sources [87].

Tremblay *et al.* (1990) [88] have proposed a theoretical model describing the evolution of alkali D line profiles as a function of the magnetic field. In their work, they have calculated the evolution of transition frequencies and intensities for magnetic fields up to 2.5 kG. However, due to the Doppler broadening they they were not able to record individually each component for magnetic fields less than 1.5 kG and thus could not conclude on the validity of their theoretical model for the small magnetic field values.

In chapter 2, we have shown that alkali dSR spectra recorded from a NC experience strong line narrowing. Among other advantages of the dSR technique is proportionality of the recorded signal to atomic transition probabilities in addition to the fact their transition frequencies are the same than that of local maximums in the dSR spectrum. These benefits make the dSR technique particularly convenient for the studies of closely-spaced individual atomic transition components in a magnetic field.

In this chapter, we derive the expression of the Hamiltonian describing the interaction between the valence electron of alkali atoms and a homogeneous static magnetic field, starting from the time-independant Dirac equation. We present a theoretical model, partially based on that depicted in [88], describing the evolution of alkali transition frequencies and intensities as a function of the magnetic field. Furthermore, we present a computational method to perform numerical simulations. Numerical results demonstrate particular behaviors of alkali D line transitions for intermediate values of magnetic fields, resulting in dichroism. The last section is dedicated to experimental studies of Rb and K vapor behavior in magnetic fields, where alkali spectra are recorded with the dSR technique. Comparing experimental spectra with numerical simulations, we conclude on the quality of the theoretical model.

3.1 Theoretical background

The most accurate way to study the spectrum of an alkali atom within an electromagnetic field described by the potentials $\boldsymbol{A}, V$ is the time independent Dirac equation limited to the order v^2/c^2, applied to a single electron

$$\left[\frac{1}{2m_e}(\mathbf{p}+\frac{e}{c}\mathbf{A})^2+\frac{e}{m_e c}\mathbf{S}\cdot\boldsymbol{\nabla}\times\mathbf{A}-\frac{p^4}{8m_e^3c^2}-\frac{e\hbar}{8m_e^2c^2}\Delta V - \frac{e}{2m_e^2c^2}\mathbf{S}\cdot(\nabla V\times\mathbf{p})-eV\right]\Psi=E\Psi, \tag{3.1}$$

where $\mathbf{S} = (\hbar/2)\cdot\boldsymbol{\sigma}$ is the spin momentum of the electron with $\boldsymbol{\sigma} = (\sigma_x, \sigma_y, \sigma_z)$ the matrices of Pauli; $\mathbf{p}$ is the impulsion, m_e is the mass of the electron and e its electric charge. This equation includes respectively the kinetic energy and interaction with a field described by a potential vector $\mathbf{A}$, the interaction of the spin magnetic moment with a magnetic field $\mathbf{B} = \boldsymbol{\nabla}\times\mathbf{A}$, the first order relativistic correction, the Darwin term (inducing an energy shift on S-states), the spin-orbit interaction, and the scalar potential energy.

3.1.1 Zero-field Hamiltonian

At first, we want to examine each of the zero-field ($\mathbf{A} = 0$) contributions to the Dirac Hamiltonian and find an appropriate basis to expand them. When only considering a non relativistic electron in the gauge $\{\mathbf{A} = 0, V\}$, Eq. (3.1) reduces to

$$\Big[\mathcal{H}_k + \mathcal{H}_c\Big]\Psi_n \equiv \Big[\frac{\mathbf{p}^2}{2m_e} - eV\Big]\Psi_n = E_n\Psi_n. \tag{3.2}$$

For a spherically symmetric potential $V \equiv V(r)$ and in the case of bounded atomic states, the previous eigenvalue equation is known to yield

$$E_n = -\mathcal{R}\frac{Z^2}{n^2}, \tag{3.3a}$$

$$|nLm\rangle \equiv \Psi_{nLm}(r,\theta,\phi) = R_{nl}(r)Y_{Lm}(\theta,\phi), \tag{3.3b}$$

where $\mathcal{R} \equiv m_e e^4(8\epsilon_0 h^2)^{-1} \approx 13.6$ eV is the Rydberg constant, the eigenvectors $|nLm\rangle$ are called the bound states often associated with hydrogen ($Z = 1$) or hydrogen-like atoms/ions ($Z > 1$) whose eigenvalues are degenerate n^2 times. They are function of R_{nL} and spherical harmonics $Y_{Lm}(\theta,\phi)$ [89, chapter XII].

Let us examine the spin-orbit (SO) interaction Hamiltonian $\mathcal{H}_{SO} = -e/2m_e^2c^2\ \mathbf{S}\cdot(\boldsymbol{\nabla}V\times\mathbf{p})$, responsible for the atomic fine structure. For a potential $V \equiv V(r) = Ze/r$, one has

$$\boldsymbol{\nabla}V\times\mathbf{p} = \frac{1}{r}\frac{\partial}{\partial r}V(r)\ \mathbf{L} \tag{3.4}$$

where we have used the definition of the angular momentum: $\mathbf{L} = \mathbf{r}\times\mathbf{p}$. Hence, the SO interaction can be rewritten in a more compact form

$$\mathcal{H}_{SO} = \frac{Ze^2}{2m_e^2c^2r^3}\ \mathbf{L}\cdot\mathbf{S}. \tag{3.5}$$

Obviously, the angular momentum commutes with the spin momentum as $\mathbf{L}$ acts on the functions of coordinates while $\mathbf{S}$ acts on the spin functions. The Hamiltonian describing an electron bounded to the nucleus by a potential $V(r)$ with the spin orbit interaction is

$$\mathcal{H}_0 + \mathcal{H}_{SO} = -\frac{\hbar^2}{2m_e}\nabla^2 - \frac{Ze^2}{r} + \frac{Ze^2}{2m_e^2c^2r^3}\ \mathbf{L}\cdot\mathbf{S}. \tag{3.6}$$

Noting that $\mathbf{L}\cdot\mathbf{S} = 1/2\ \left(\mathbf{J}^2 - \mathbf{L}^2 - \mathbf{S}^2\right)$, where we have defined $\mathbf{J} = \mathbf{L} + \mathbf{S}$, let us find an appropriate basis to expand $\mathcal{H}_{SO}$. The following commutation relation can be derived :

$$[\mathcal{H}_0, L^2] = [\mathcal{H}_0, S^2] = [\mathcal{H}_0, J^2] = [\mathcal{H}_0, L_\alpha] = [\mathcal{H}_0, S_\alpha] = [\mathcal{H}_0, J_\alpha] = 0, \tag{3.7a}$$

$$[\mathbf{L}\cdot\mathbf{S}, L^2] = [\mathbf{L}\cdot\mathbf{S}, S^2] = [\mathbf{L}\cdot\mathbf{S}, J^2] = [\mathbf{L}\cdot\mathbf{S}, J_z] = 0, \tag{3.7b}$$

$$[\mathbf{L}\cdot\mathbf{S}, L_z] \neq 0 \qquad [\mathbf{L}\cdot\mathbf{S}, S_z] \neq 0, \tag{3.7c}$$

where α denotes an arbitrary component (Cartesian, spherical,...) of the operator. From (3.7a), one can see that both coupled ($|LSJm_J\rangle \equiv |J, m_J\rangle$) and uncoupled ($|LSm_Lm_S\rangle \equiv |m_L, m_S\rangle$) are eigenbasis of $\mathcal{H}_0$. While the uncoupled basis is not eigenfunction of $\mathbf{L}\cdot\mathbf{S}$ (see (3.7c)), Eq. (3.7b) shows that the coupled one is simultaneously eigenbasis of L^2, S^2, J^2 and J_z. Thus, it is preferable to expand $\mathcal{H}_{SO}$ in the coupled basis. Noting that L^2, S^2, J^2 have only diagonal elements (see appendix B.1), the only off-diagonal contribution arises from the term r^{-3}, which can be neglected using the perturbation theory. We have

$$\begin{aligned} E_{SO} &\equiv \langle J, m_J|\mathcal{H}_{SO}|J, m_J\rangle \\ &= \frac{Ze^2}{4m_e^2c^2}\hbar^2\left[J(J+1) - L(L+1) - S(S+1)\right]\langle nL|r^{-3}|nL\rangle, \end{aligned} \tag{3.8}$$

where the matrix elements $\langle nL|r^{-k}|nL\rangle$ ($k \geqslant 1$) can be found in the literature. We finally find that

$$E_{SO} = \frac{Z^4e^2\hbar^2}{4a_0^3m_e^2c^2}\cdot\frac{J(J+1) - L(L+1) - S(S+1)}{n^3(L+1)(L+\frac{1}{2})L}, \tag{3.9}$$

with $a_0 \equiv 4\pi\epsilon_0\hbar^2(m_ee^2)^{-1} \approx 0.53$ Å the Bohr radius in the infinitely massive nucleus approximation. One of the consequences is that the SO interaction partially rises the degeneracy of a level $|n\rangle$: a given eigenvalue of $\mathcal{H}_0 + \mathcal{H}_{SO}$ is only degenerated $2J+1$ times (n^2 for that of $\mathcal{H}_0$).

We now examine the first order relativistic correction $\mathcal{H}_R = -p^4/8m_e^3c^2$. Recalling that $\mathcal{H}_0 = p^2/2m_e - Ze^2/r$, $\mathcal{H}_R$ can be rewritten as

$$\mathcal{H}_R = -\frac{1}{2m_ec^2}\left(\mathcal{H}_0 + \frac{Ze^2}{r}\right)^2. \tag{3.10}$$

On a similar fashion to that for the spin-orbit interaction, we treat $\mathcal{H}_R$ as a perturbative term in the coupled basis $|nLS, Jm_J\rangle$. While being careful that r^{-1} and $\mathcal{H}_0$ do not necessarily commute, one can show that the first order relativistic correction has only diagonal elements that read

$$E_R = -E_n^2\frac{Z^2e^2}{2m_ec^2a_0}\left(\frac{2n}{L+\frac{1}{2}} - 3\right). \tag{3.11}$$

Finally, the Darwin term $\mathcal{H}_D = e\hbar^2\Delta V/8m_e^2c^2$ is known to produce an energy shift only for the S-states ($L = 0$). Its expression reads

$$E_D = \frac{Z^4e^2\hbar^2}{2n^3m_e^2c^2a_0^3}. \tag{3.12}$$

All these terms form the so-called atomic fine structure, whose Hamiltonian is

$$\mathcal{H}_f = \mathcal{H}_k + \mathcal{H}_c + \mathcal{H}_{SO} + \mathcal{H}_R + \mathcal{H}_D. \tag{3.13}$$

It is interesting to note that, for the fine structure, the energies of the states $n^2S_{1/2}$ and $n^2P_{1/2}$ are identical. However, experiments using hydrogen atoms have shown small discrepancies. This difference, called the Lamb shift, can be corrected using higher-order radiative corrections, see e.g [90].

3.1.2 Magnetic Hamiltonian

Let us now consider the Zeeman effect which arises when $\mathbf{A} \neq 0$. From Eq. (3.1), the magnetic Hamiltonian limited at the order v^2/c^2 reads

$$\mathcal{H}_m = \frac{e}{2m_e c}\left(\mathbf{p}\cdot\mathbf{A} + \mathbf{A}\cdot\mathbf{p}\right) + \frac{e}{m_e c}\,\mathbf{S}\cdot\boldsymbol{\nabla}\times\mathbf{A}. \tag{3.14}$$

For what follows, we will suppose that the magnetic field interacting with the alkali atoms (spin 1/2) is static and homogeneous, that is $\mathbf{B} = 1/2\ \boldsymbol{\nabla}\times(\mathbf{B}\times\mathbf{r})$, such that $\nabla\cdot\mathbf{A} = 0$, and

$$\mathbf{A} = \frac{1}{2}\left(\mathbf{B}\times\mathbf{r}\right). \tag{3.15}$$

In this case, one can show that $[\mathbf{A}, \mathbf{r}] = 0$. The magnetic Hamiltonian can thus be expressed as

$$\mathcal{H}_m = \frac{\mu_B}{\hbar}\ \mathbf{B}\cdot(\mathbf{L} + 2\ \mathbf{S}), \tag{3.16}$$

where $\mu_B \equiv e\hbar\ (2m_e c)^{-1} \approx 9,27\times10^{-24}$ JT^{-1} is the Bohr magneton. Thanks to the small size of the vapor column, the magnetic field in the cell should verify the hypothesis of uniformity which will be verified in section 3.3 by comparing experimental and theoretical results.

By analogy with the classical expression of a magnetic dipole, the magnetic Hamiltonian is sometimes written as $\mathcal{H}_m = -\boldsymbol{\mu}_L\cdot\mathbf{L} - \boldsymbol{\mu}_S\cdot\mathbf{S}$, where $\boldsymbol{\mu}_L = -g_L\mu_B\hbar^{-1}\mathbf{L}$ and $\boldsymbol{\mu}_S = -g_S\mu_B\hbar^{-1}\mathbf{S}$ are interpreted as magnetic moment operators respectively associated with orbital angular momentum and the spin angular momentum. The factors $g_L = 1$ and $g_S = 2$ are respectively the so-called electron orbital and electron spin Landé factors, which account for various modifications to the corresponding magnetic dipole moments. When taking into account the finite mass of the nucleus, one has $g_L = 1 - m_e/m_n$, where m_n is the nuclear mass. Let us also note that, while the theory of Dirac predicts $g_S = 2$, higher order corrections from quantum electrodynamics show that $g_S \simeq 2.002319304$ [91].

We choose the frame such that the applied static magnetic field $\mathbf{B}$ is along z-axis, that is $\mathbf{B} = B_z\ \hat{\mathbf{e}}_z$, defining the quantization axis. In this frame, the magnetic Hamiltonian (3.16), taking into account the corrections to g_L and g_S, reads

$$\mathcal{H}_m = \frac{\mu_B}{\hbar}B_z\left(g_L L_z + g_S S_z\right) \equiv \frac{\mu_B}{\hbar}B_z\left(g_L L_0^{(1)} + g_S S_0^{(1)}\right), \tag{3.17}$$

In Eq. 3.17, we have explicitly written the orbital momentum and the spin momentum as rank one tensorial operators since they both verify the properties exposed in appendix B.3. The next

step is to calculate the matrix elements of $\mathcal{H}_m$. Noting that $\mathbf{L} = \mathbf{J} - \mathbf{S}$, we can rewrite Eq. (3.17) as

$$\mathcal{H}_m = \frac{\mu_B}{\hbar} B_z \left[g_L J_0^{(1)} + (g_S - g_L) S_0^{(1)} \right]. \tag{3.18}$$

Making use of the Wigner-Eckart theorem and derived formulas, see appendix B.3, one can show [92] that

$$\begin{aligned} \langle J, m_J | \mathcal{H}_m | J', m'_J \rangle =& \mu_B B_z \delta_{LL'} \delta_{SS'} \delta_{m_J m'_J} \Bigg[g_L m_J \delta_{JJ'} - (g_S - g_L)(-1)^{m_J+L+S} \sqrt{2J+1} \\ & \times \sqrt{2J'+1} \sqrt{S(S+1)(2S+1)} \begin{pmatrix} J & 1 & J' \\ -m_J & 0 & m_J \end{pmatrix} \begin{Bmatrix} L & S & J \\ 1 & J' & S \end{Bmatrix} \Bigg], \end{aligned} \tag{3.19}$$

Expanding the $3j$ and $6j$ coefficients, see for example Chapters 8 and 9 in Varshalovich (1988) [93], we get for the diagonal matrix elements of $\mathcal{H}$

$$\langle J, m_J | \mathcal{H}_0 + \mathcal{H}_m | J, m_J \rangle = E_f(J) + \mu_B g_J m_J B_z, \tag{3.20}$$

where g_J is the Landé factor associated with the total electronic angular momentum $\mathbf{J}$, given by

$$g_J = g_L \frac{J(J+1) - S(S+1) + L(L+1)}{2J(J+1)} + g_S \frac{J(J+1) + S(S+1) - L(L+1)}{2J(J+1)}. \tag{3.21}$$

As a consequence of the Wigner-Eckart Theorem, the off-diagonal elements of the Hamiltonian are nonzero only between states such that $\Delta L = L - L' = 0$, $\Delta m_J = m_J - m'_J = 0$ and read

$$\begin{aligned} \langle J, m_J | \mathcal{H}_0 + \mathcal{H}_m | J-1, m_J \rangle =& \frac{\mu_B}{2} (g_L - g_S) B_z \sqrt{\frac{J^2 - m_J^2}{J(2J+1)(2J-1)}} \\ & \times \sqrt{\frac{[(L+S+1)^2 - J^2][J^2 - (L-S)^2]}{J}}. \end{aligned} \tag{3.22}$$

Although the intrinsic electronic magnetic momentum (spin) appears naturally in the construction of the Dirac equation, it omits the possible interaction of the nuclear spin momentum $\mathbf{I}$ with the total electronic angular momentum $\mathbf{J}$. Indeed, as electrons are moving charges, they create a magnetic field with which the nucleus can interact. It results in the splitting of the fine structure, called hyperfine structure as this splitting is much smaller than that induced by the SO interaction. In order to take it into account, one can rewrite the unperturbed (zero-field) Hamiltonian as $\mathcal{H}_0 = \mathcal{H}_f + \mathcal{H}_{hf}$ with

$$\mathcal{H}_{hf} = \sum_k \mathbf{T}^{(k)} \cdot \mathbf{M}^{(k)}, \tag{3.23}$$

where $\mathbf{T}^{(k)}$ and $\mathbf{M}^{(k)}$ are spherical tensorial operator of rank k whose product describes the interaction between the nucleus and atomic electrons. In this equation, even k values reprensent

electric interactions while odd k values represent magnetic interactions, see for example [27]. Limiting the expansion of (3.23) to $k = 2$, the hyperfine Hamiltonian reads

$$\mathcal{H}_{hf} = A_{hf}\ \mathbf{I}\cdot\mathbf{J} + B_{hf}\frac{3(\mathbf{I}\cdot\mathbf{J})^2 + \frac{3}{2}\mathbf{I}\cdot\mathbf{J} - I(I+1)J(J+1)}{2I(2I-1)2J(2J-1)}, \tag{3.24}$$

where A_{hf} is the magnetic dipole constant and B_{hf} is the electric quadrupole one, determined experimentally. It was shown by Gerginov *et al.* (2003) [94] that higher order multipole interactions are small as compared to the first two ($\Delta E/h < 1$ kHz). The construction of the Hamiltonian describing the interaction of a static magnetic field with alkali atoms including their hyperfine structure is done in the way analogous to that for the case of the fine structure: the Hamiltonian of the system is given by the sum of the unperturbed Hamiltonian $\mathcal{H}_0$ and the magnetic contribution $\mathcal{H}_m$, and

$$\mathcal{H}_m = \frac{\mu_B}{\hbar}B_z\left(g_L L_z + g_S S_z + g_I I_z\right). \tag{3.25}$$

where g_I is the nuclear Landé factor. The diagonal elements of $\mathcal{H}$ in the coupled basis $|F, m_F\rangle$ are given by

$$\langle F, m_F|\mathcal{H}|F, m_F\rangle = E_{hf}(F) + \mu_B g_F m_F B_z, \tag{3.26}$$

where $E_{hf}(F)$ is the hyperfine energy of the sub-levels $|F, m_F\rangle$ in the absence of magnetic field, and

$$g_F = g_J\frac{F(F+1) - I(I+1) + J(J+1)}{2F(F+1)} + g_I\frac{F(F+1) + I(I+1) - J(J+1)}{2F(F+1)} \tag{3.27}$$

is the associated Landé factor. One can show that the off-diagonal matrix elements are nonzero only when $\Delta F = \pm 1$ and $\Delta m_F = 0$. They are given by [88]

$$\begin{aligned}\langle F-1, m_F|\mathcal{H}|F, m_F\rangle &= \langle F, m_F|\mathcal{H}|F-1, m_F\rangle \\ &= \frac{\mu_B}{2}(g_J - g_I)B_z\sqrt{\frac{F^2 - m_F^2}{F(2F+1)(2F-1)}} \\ &\quad\times\sqrt{\frac{[(J+I+1)^2 - F^2][F^2 - (J-I)^2]}{F}}.\end{aligned} \tag{3.28}$$

A consequence of the last relation is that the matrix representation of $\mathcal{H}$ is block diagonal: each block corresponds to a given value of m_F. Let us note that the sign difference between the work of Tremblay *et al.* (1990) [88] and the model exposed above is linked to different sign convention for the Landé factors, see e.g. [27, page 36].

3.1.3 Level shift and transition probabilities

We are interested in finding the evolution of optical transitions between the ground state $n^2S_{1/2}$ further denoted $|g\rangle$, and the excited states $n^2P_{1/2}$ (D_1 line) and $n^2P_{3/2}$ (D_2 line) further denoted

$|e\rangle$. Three regimes will be covered: a weak-field regime, when the magnetic interaction can be treated as a perturbation, often referred to as the Zeeman regime; a strong-field regime, when the field is sufficiently strong that it decouples **I** and **J**, often referred to as the hyperfine Paschen-Back (HPB) regime; and in between the two, an intermediate regime where no proper quantum numbers can describe the system.

While relatively simple formulas can express the frequency shift of the transitions in the first two regimes, no similar expressions can be found for the last one. To get results in the intermediate regime, we thus have to diagonalize $\mathcal{H}_m$. After diagonalization, the system will be described by a new set of state vectors denoted as $|F', m_F\rangle$ that we can express in the unperturbed basis as

$$|\Psi(F'_g, m_{F_g})\rangle = \sum_{F_g} \chi_{F'_g F_g}(B)|F_g, m_{F_g}\rangle, \tag{3.29a}$$

$$|\Psi(F'_e, m_{F_e})\rangle = \sum_{F_e} \chi_{F'_e F_e}(B)|F_e, m_{F_e}\rangle, \tag{3.29b}$$

where $\chi_{F'_{g,e}F_{g,e}}(B)$ are the (B-field dependent) mixing coefficients. In what follows, we give useful formulas to calculate the energy shifts (and thus the transition frequencies) versus magnetic field and we express the transition probabilities depending on the incident electric field polarization.

Level and transition frequency shifts

The weak magnetic field regime occurs when $B_z \ll B_0$, where $B_0 = A_{hf}\mu_B^{-1}$. To the lowest order, the energy levels split linearly [95] according to

$$E_{|F,m_F\rangle}(B_z) = E_0(F) + \mu_B g_F m_F B_z. \tag{3.30}$$

In the case of strong magnetic field, that is $B_z \gg B_0$, J is a good quantum number and the eigenvalues in the uncoupled basis can be written as [96]

$$\begin{aligned} E_{|J\ m_J, I\ m_I\rangle}(B_z) = A_{hf} m_J m_I + B_{hf} \frac{3(m_J m_I)^2 + 3/2 \times m_I m_I - I(I+1)J(J+1)}{2J(2J-1)I(2I-1)} \\ + \mu_B(g_J m_J + g_I m_I)B_z. \end{aligned} \tag{3.31}$$

In the intermediate regime $B_z \sim B_0$, one has to diagonalize $\mathcal{H}_m$. It is worth to note however that for the D line ground state one can use the Breit-Rabi formula [97]

$$\begin{aligned} E_{|J=1/2\ m_J, I\ m_I\rangle}(B_z) = -A_{hf}\frac{I+1/2}{2(2I+1)} + g_I\mu_B B_z(m_I \pm 1/2) \\ \pm A_{hf}\frac{I+1/2}{2}\left(1 + \frac{4x(m_I \pm 1/2)}{2I+1} + x^2\right)^{1/2}, \end{aligned} \tag{3.32}$$

where $x = (I+1/2)(g_J - g_I)\mu_B B_z (A_{hf})^{-1}$. Otherwise, the energies are obtained by numerical diagonalization of $\mathcal{H}_m$. Regardless of how the eigenvalues have been obtained, the transition frequencies between a level $|g\rangle$ and $|e\rangle$ are simply calculated using

$$\omega_{eg}(B_z) = \frac{E_{|e\rangle}(B_z) - E_{|g\rangle}(B_z)}{\hbar}. \tag{3.33}$$

Transition dipole moments

Atoms interact with the electric field $\mathbf{E}$ of the laser according to $-\mathbf{d}\cdot\mathbf{E}$, where $\mathbf{d}$ is the electric dipole moment. In terms of standard components, the electric dipole moment and the electric field are expressed as

$$\mathbf{d}\cdot\mathbf{e} = \sum_q (-1)^q d_{-q} e_q, \qquad \mathbf{E}\cdot\mathbf{e} = \sum_q (-1)^q E_{-q} e_q, \tag{3.34}$$

where $\mathbf{e}_q$ is a unit vector of the spherical basis and $q = 0, \pm 1$. The Cartesian (laboratory) coordinates are linked to the spherical ones by the relations

$$\boldsymbol{e}_{+1} = -\frac{\boldsymbol{e}_x + i\boldsymbol{e}_y}{\sqrt{2}}, \qquad \boldsymbol{e}_{-1} = +\frac{\boldsymbol{e}_x - i\boldsymbol{e}_y}{\sqrt{2}}, \qquad \boldsymbol{e}_0 = \boldsymbol{e}_z, \tag{3.35}$$

where we recall that $\mathbf{e}_z$ was chosen as the quantization axis. Hence, $E_{0,+1,-1}$ corresponds to a linearly, left and right-circularly polarized electric field, respectively.

The matrix elements of a given component of the electric dipole observable in the dipole approximation, see appendix A.2.1, are known to be proportional to the spontaneous rate A_{eg} of the associated transition, see for example de Clerc *et al.* (1984) [98]

$$|\langle e|d_q|g\rangle|^2 = \frac{3\epsilon_0 \hbar \lambda_{eg}^3}{8\pi^2} A_{eg}. \tag{3.36}$$

The spontaneous emission rates are given by the product of the excited state natural linewidth Γ with the square of the transfer coefficients modified by the external magnetic field such that

$$A_{eg} = \Gamma a^2[\Psi(F'_e, m_{F_e}); \Psi(F'_g, m_{F_g}); q]. \tag{3.37}$$

The transfer coefficients can then be expressed in the "old" coupled basis (before diagonalization, see (3.29)), their expressions read

$$a[\Psi(F'_e, m_{F_e}); \Psi(F'_g, m_{F_g}); q] = \sum_{F_e, F_g} \chi_{F'_e F_e} a(F_e, m_{F_e}; F_g, m_{F_g}; q) \chi_{F'_g F_g}, \tag{3.38}$$

with $a(F_e, m_{F_e}; F_g, m_{F_g}; q)$ the transfer coefficients associated to the unperturbed basis $|F, m_F\rangle$, defined as [98]

$$\begin{aligned} a(F_e, m_{F_e}; F_g, m_{F_g}; q) =& (-1)^{1+I+J_e+F_e+F_g-m_{F_e}} \sqrt{2J_e+1}\sqrt{2F_e+1}\sqrt{2F_g+1} \\ &\times \begin{pmatrix} F_e & 1 & F_g \\ -m_{F_e} & q & m_{F_g} \end{pmatrix} \begin{Bmatrix} F_e & 1 & F_g \\ J_g & I & J_e \end{Bmatrix}. \end{aligned} \tag{3.39}$$

The parentheses denote the 3-j symbols and the curly brackets denote the 6-j symbols. The transition exists only if the m_F values of the excited and ground states verify the selection rules defined by

$$\Delta m_F \equiv m_{F_e} - m_{F_g} = q, \tag{3.40}$$

where q is the standard component defined in (3.34) also associated to the field polarization: $q = 0$ corresponds to a π–polarized (linear) field, $q = +1$ to a σ^+–polarized (circular left) field and $q = -1$ to a σ^-–polarized (circular right) field. We will show later that, due to the mixing of states, $\Delta F = 0, \pm 1$ is not a strict selection rule.

3.2 Numerical simulations

This section is dedicated to numerical simulations of the theoretical model exposed above. We start by reviewing the computational procedure carrying out calculation of alkali D lines evolution in the presence of a static magnetic field. We apply this procedure to calculate the evolution of both ^{85}Rb ($I = 5/2$) and ^{87}Rb ($I = 3/2$) isotopes' energy levels, transition frequencies and transition dipole moments for magnetic fields ranging from 0 up to $3B_0$. Obviously, this procedure allows one to perform similar calculations at higher fields and for other alkalis. From these results, we discuss the induced circular dichroism. Making use of the model derived in chapter 2, we propose a method to calculate spectra of alkali as a function of the magnetic field and the incident light polarization.

3.2.1 Computational procedure

Transition frequencies and intensities

Equations (3.29, 3.33, 3.38) have shown the necessity of obtaining the eigenvalues and eigenvectors of $\mathcal{H}$ in order to compute the evolution of the transitions as a function of the magnetic field. As the degeneracy of each state is equal to $2F+1$, $\mathcal{H}$ is of dimension 48 when considering both D_1 and D_2 hyperfine manifolds of ^{85}Rb as an example: 12 states from $5S_{1/2}$, 12 from $5P_{1/2}$ and 26 from $5P_{3/2}$. In the case of brute force diagonalization, one thus has to evaluate 48 eigenvalues and 48×48 components for the eigenvectors. As the Hamiltonian is different for each considered value of the magnetic field, it should be rebuilt at each iteration of the program. We are thus facing an highly recurrent task. For sure, block by block diagonalization would lower the calculation time, but thanks to the large computational power of personal computers, this optimization is not mandatory.

To perform the calculation using the theoretical model exposed above, we have developed a FORTRAN90 program which recursively evaluates energy levels, transition frequencies and transition dipole moments for B-field values in a range specified by the user. An overview of this program is shown in Fig. 3.1; the routine functions called by the program are briefly described here-after.

`Initialize()`. An initialization step is necessary to allocate all the arrays (memory) that will be used throughout the program. For the alkali specified as its argument (^{85}Rb in the example of Fig. 3.1), the initialization function loads related data (quantum numbers, zero-field state energies, etc.) that we have compiled in a data file. These values are picked from [28, 29, 61] for every alkali atom studied in the present thesis. Furthermore, a buffer file is created; it makes a correspondence between each ket labels $|i\rangle$ (i^{th} vector of the basis) and their corresponding quantum numbers. This is particularly important when applying selection rules to calculate transition shifts and dipole moments.

`FillHamiltonian()`. Looping over each possible states of the basis, the routine builds the Hamiltonian using formula (3.26) for the diagonal matrix elements and (3.28) for the off-diagonal ones that verifies $\Delta m_F = 0$, $\Delta F = \pm 1$. Otherwise, the matrix elements are set to zero.

`Diagonalize()`. To diagonalize $\mathcal{H}$, we employ a Gaussian elimination algorithm, see for

```
PROGRAM AlkaliSpectra.f90
atom = '85Rb'
call initialization(atom)
step = 1.0d0 ! in Gauss
    do i=1,n
        B = (i - 1) * step
        call fillHamiltonian(B,H)
        call diagonalize(H,HD,EV)
        call sort(HD,EV)
        call transitionShifts(HD)
        call transitionIntensities(EV)
    enddo
end
```

Figure 3.1: Overview of the FORTRAN90 program performing the calculations for ^{85}Rb atoms. Subroutines are briefly described in the text.

example section 3.2 in Olver *et al.* (2010) and refs. therein [99], that solves the characteristic polynomial

$$\det[\mathcal{H} - \lambda \mathbb{1}] = 0, \tag{3.41}$$

where λ is an eigenvalue and $\mathbb{1}$ is the identity matrix having the same dimension as the Hamiltonian to diagonalize. After obtaining the eigenvalues, the eigenvectors Ψ are found using the eigenvalue equation

$$\mathcal{H}\Psi_i = \lambda_i \Psi_i. \tag{3.42}$$

`Sort()`. Due for example to possible level crossing, the Gaussian diagonalization algorithm employed by the `diagonalize()` routine cannot sort eigenvalues and eigenvectors the same way it did for the previous value of magnetic field. For this reason, when called, the sort routine compares the first order derivative of a given eigenvalue (obtained at the iteration i) with the ones calculated at the iteration $i-1$ and $i-2$. If the derivatives do not coincide (at a given level of tolerance), the routine swaps with another eigenvalue obtained at the iteration i until a good coincidence is found with all eigenvalues.

`ShiftsAndIntensities()`. After finding eigenvalues and vectors with `Diagonalize()`, and having verified that the order of the basis coincides with the initial one with `Sort()`, the transition frequency shifts and dipole moments are calculated using (3.33) and (3.36) for both D lines and every polarization by looping over all possible states and standard components while applying the selection rules, and saving the results to data files. Due to the mixing of states, the selection rules $\Delta F = 0, \pm 1$ are not applicable, and transitions verifying $\Delta F = \pm 2$ are even possible [88]. Indeed, nor F, m_F, nor m_J, m_I are good quantum numbers in the intermediate regime of fields. As we start the calculations at low B-field values, we label the transitions according to the initial states in the coupled basis. To be accurate one would have to name them using the mixing coefficients, see Eq. (3.29).

Selective reflection spectrum under magnetic field

In the previous sections, we have given a theoretical model illustrating how the alkali D line transitions behave when atoms interact with a longitudinal magnetic field and presented a procedure to compute it for a wide range of magnetic fields. In chapter 2 we have shown how to calculate theoretically dSR spectra for the complete hyperfine manifold of both D lines, describing the vapor as an ensemble of two-level systems; demonstrating an excellent agreement with experiments.

Hence, it is reasonable to use the results for transition frequencies and intensities as data for ω_i and A_i of (2.52), repeating the procedure of section 2.2.1 for every transition allowed by a given polarization or combination of polarizations. In fact, this procedure is correct since magnetic fields considered in the frame of this thesis are time independent and supposed to be homogeneous (along the propagation axis). This procedure is indeed equivalent to writing (2.27) as

$$\mathcal{H} = \mathcal{H}_0 + \mathcal{H}_B + \mathcal{H}_L, \tag{3.43}$$

and finding a unitary transformation $\mathcal{U}$ that diagonalize $\mathcal{H}_0 + \mathcal{H}_B$ such that

$$\begin{aligned} \tilde{\mathcal{H}}_0 + \tilde{\mathcal{H}}_L &= \mathcal{U}\big(\mathcal{H}_0 + \mathcal{H}_B\big)\mathcal{U}^\dagger + \mathcal{U}\mathcal{H}_L\mathcal{U}^\dagger \\ &= \sum_i \omega_{g_i}|g_i\rangle\langle g_i| + \sum_j \omega_{e_j}|e_j\rangle\langle e_j| - \sum_{i,j}\hbar\Omega_{ij}|e_j\rangle\langle g_i| + cc. \end{aligned} \tag{3.44}$$

where $|g_i\rangle$ and $|e_j\rangle$ are states vectors from the coupled basis after diagonalization, see (3.29). With the same hypothesis of low electric field power, one can decompose (3.44) as an ensemble of two-level systems.

3.2.2 Evolution of Rb D line transitions under magnetic field

To illustrate the model, we present in this section the evolution of Rb D_1 and D_2 line transition frequencies and probabilities for magnetic fields ranging from 0 up to $3B_0$; at this last value, hints related to the undergoing establishment of the Paschen-Back regime should be visible.

Rubidium D_1 line

The ^{85}Rb D_1 line transition frequencies and dipole moments are shown on Fig. 3.2, where we plotted their evolution as a function of the magnetic field ranging from 0 to $3B_0 \approx 2.1$ kG, as the constant $B_0 \approx 700$ G for ^{85}Rb atoms. From panels (a-c), one can see that as the field increases, the transition dipole moments (proportional to the square of the transfer coefficients) tend to two different values: while the first group tends to 0.165 (for $\sigma^\pm$ polarizations, see Fig. 3.2(a) and (c)) and 0.085 (for π polarization, see Fig. 3.2(b)), the other group of transitions tends to 0. That, along with the transitions frequency shift experiencing a linear shift with respect to the magnetic field are evidences of the ongoing establishment of the Paschen-Back regime. Let us remark that for π polarization, two transitions have a constant amplitude, see the blue solid line in Fig.3.2(b). These two transitions involve uncoupled states.

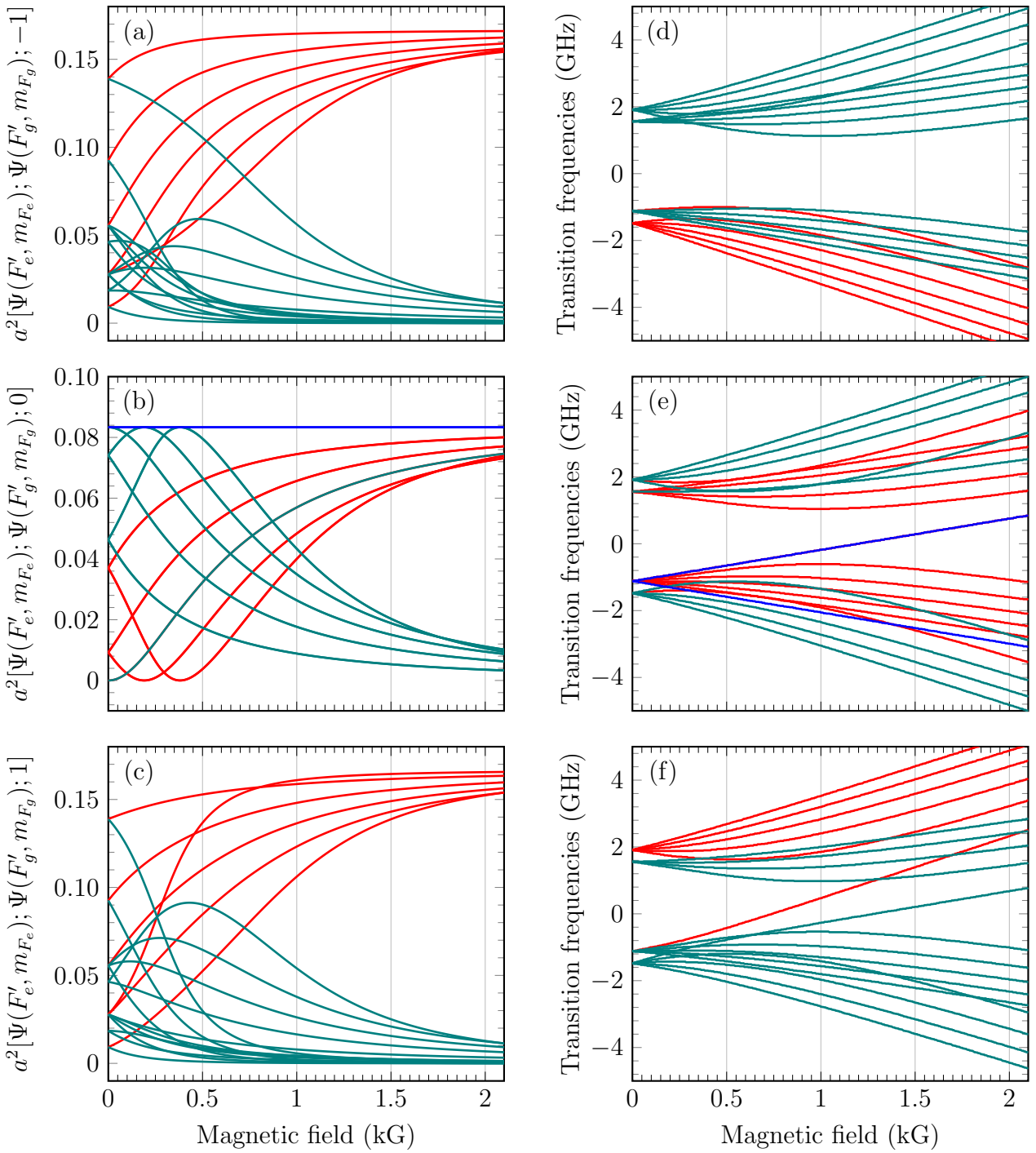

Figure 3.2: ^{85}Rb D_1 line transition frequencies (d-f) and dipole moments (a-c) as a function of the magnetic field. On panels (d-f), the zero frequency corresponds to the weighted center of the ^{85}Rb $5S_{1/2} \rightarrow 5P_{1/2}$ line. The transition frequencies and dipole moments for transitions which remain in the spectra at large fields are plotted with red lines, while with dark green lines for those which disappear. The blue solid lines indicate transitions whose dipole moments are invariant with changes in magnetic field.

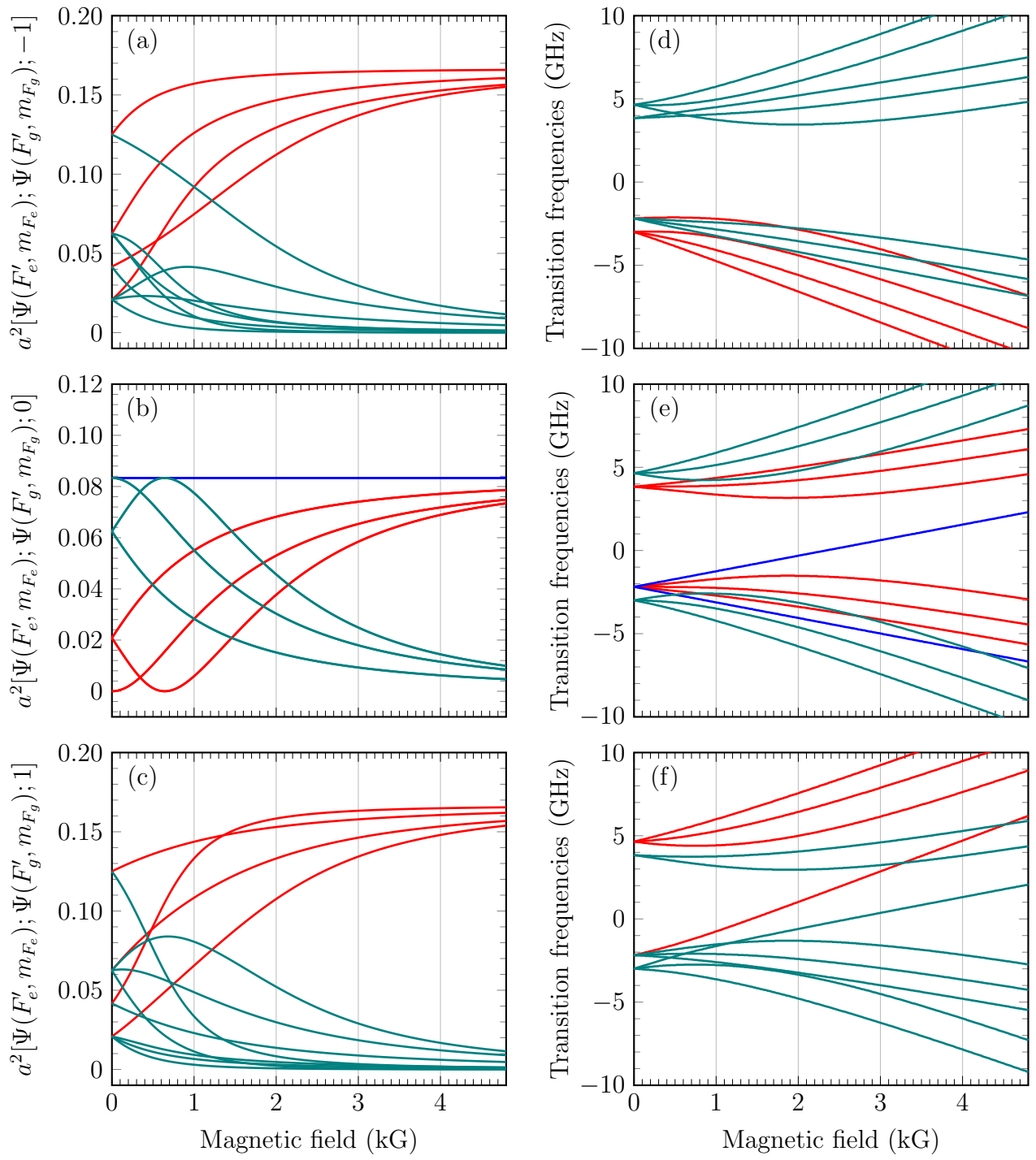

Figure 3.3: ^{87}Rb D_1 line transition frequencies (d-f) and dipole moments (a-c) as a function of the magnetic field.On panels (d-f), the zero frequency corresponds to the weighted center of the ^{87}Rb $5S_{1/2} \rightarrow 5P_{1/2}$ line. The transition frequencies and dipole moments for transitions which remain in the spectra at large fields are plotted with red lines, while with dark green lines for those which disappear. The blue solid lines indicate transitions whose dipole moments are invariant with changes in magnetic field.

One also sees from Fig. 3.2(d-f), that some transitions shift with positive magnitudes while other with negative ones, whose consequence is a spread of the transitions over a larger bandwidth: the bandwidth necessary to record all transitions at once increases with the magnetic field. However, in the Paschen-Back regime, only transitions experiencing blue shifts remain in the spectrum in the case of σ^+ polarized light (respectively red shifts for σ^-), see panels (d) and (f) of Fig. 3.2.

The ^{87}Rb D_1 line transitions frequencies and dipole moments are shown on Fig. 3.3, where we plotted their evolution as a function of the magnetic field ranging from 0 to $2B_0 \approx 4.8$ kG, where the constant $B_0 \approx 2400$ G for ^{87}Rb atoms. One observes similar behavior to that of ^{85}Rb except that the magnetic field value should be much higher, which is explained by the differences between the B_0 values. Let us also note that, as the nuclear spin of ^{87}Rb ($I = 3/2$) is smaller than that of ^{85}Rb ($I = 5/2$), the hyperfine states have smaller F quantum numbers, which lead to a smaller number of degenerated states and thus explains why one obverse less transitions than for ^{85}Rb.

Rubidium D_2 line

The case of D_2 line is slightly different from that for the D_1 line. First of all, the higher value of J for the excited state $5P_{3/2}$ leads to more hyperfine excited states than that for the D_1 line and thus more possible transitions. As noted before, transitions verifying the selection rule $\Delta F = \pm 2$ are possible in the case of the D_2 line. Note that the hyperfine states involved for the D_1 line ($5S_{1/2}$ and $5P_{1/2}$) have the same structure, there are no such states that verify $F_e = F_g \pm 2$ in contrast to the D_2 line. We will call transitions obeying $\Delta F = \pm 2$ selection rules magnetically induced (MI) transitions and we will show that they have a particular behavior.

Figure 3.4 shows the evolution of ^{85}Rb transition frequencies and dipole moments as a function of the magnetic field for up to 2.1 kG. Equivalent results for ^{87}Rb are shown in Fig. 3.5, where the transition frequencies and dipole moments are plotted for magnetic fields up to 4.8 kG. In these graphs, we have highlighted different behaviors: for $\sigma^\pm$ polarizations, the transitions split in two groups with different intensities in the Paschen-Back regime. One observes similar behavior for π polarizations except that both groups have the same amplitudes. In weaker fields, some transitions experience a large increase in their amplitude, before vanishing when increasing the magnetic field; part of these are MI transitions. One notes once again that, in the Paschen-Back regime, strong transitions shift to high frequencies for σ^+ while to lower frequencies for σ^-. Finally, transitions whose amplitudes are invariant are also observable in the D_2 line, however they appear in the spectra with of circular polarizations this time (one transition for each circular polarization).

To not overload the previous graphs, we have omitted transitions whose dipole moments remain small in the window of magnetic fields considered. In the next section we study the influence of the magnetic field on the circular dichroism. Indeed, while exploring the low and intermediate range of magnetic fields we will see that the vapor behaves in a non-symmetric way for circular polarizations which results in a circular dichroism.

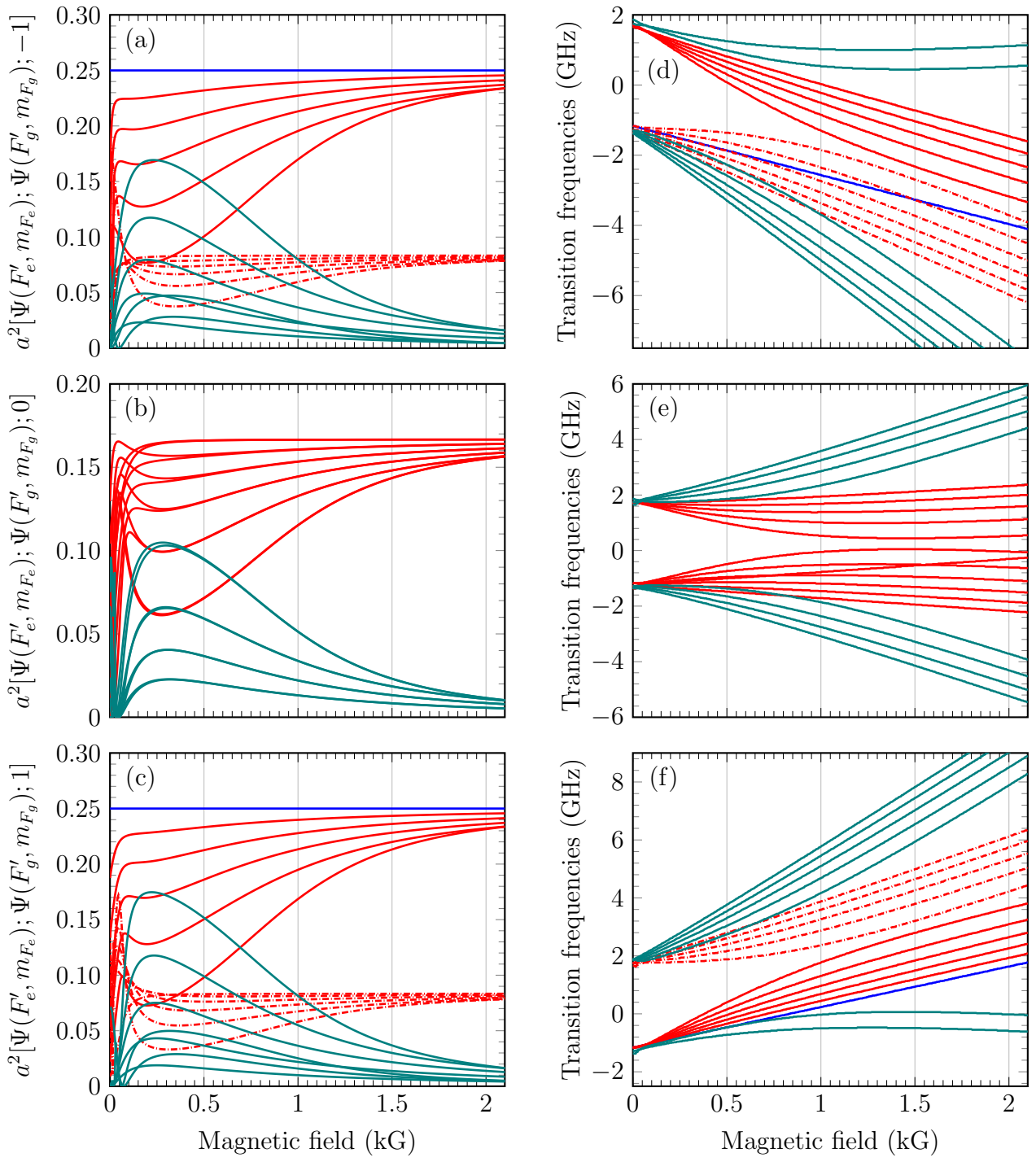

Figure 3.4: ^{85}Rb D_2 line dipole moments (a-c) and transition frequencies (d-f) as a function of the magnetic field. On panels (d-f), the zero frequency corresponds to the weighted center of the ^{85}Rb $5S_{1/2} \rightarrow 5P_{3/2}$ line. The transition frequencies and dipole moments for transitions remaining in the Paschen-Back regime split in two groups, indicated either with red solid or dash dotted lines; the dark green solid lines correspond to transitions whose dipole moments experience large increase followed by a large decrease with increasing magnetic field. The blue solid lines indicate transitions whose dipole moments are invariant with changes in magnetic field.

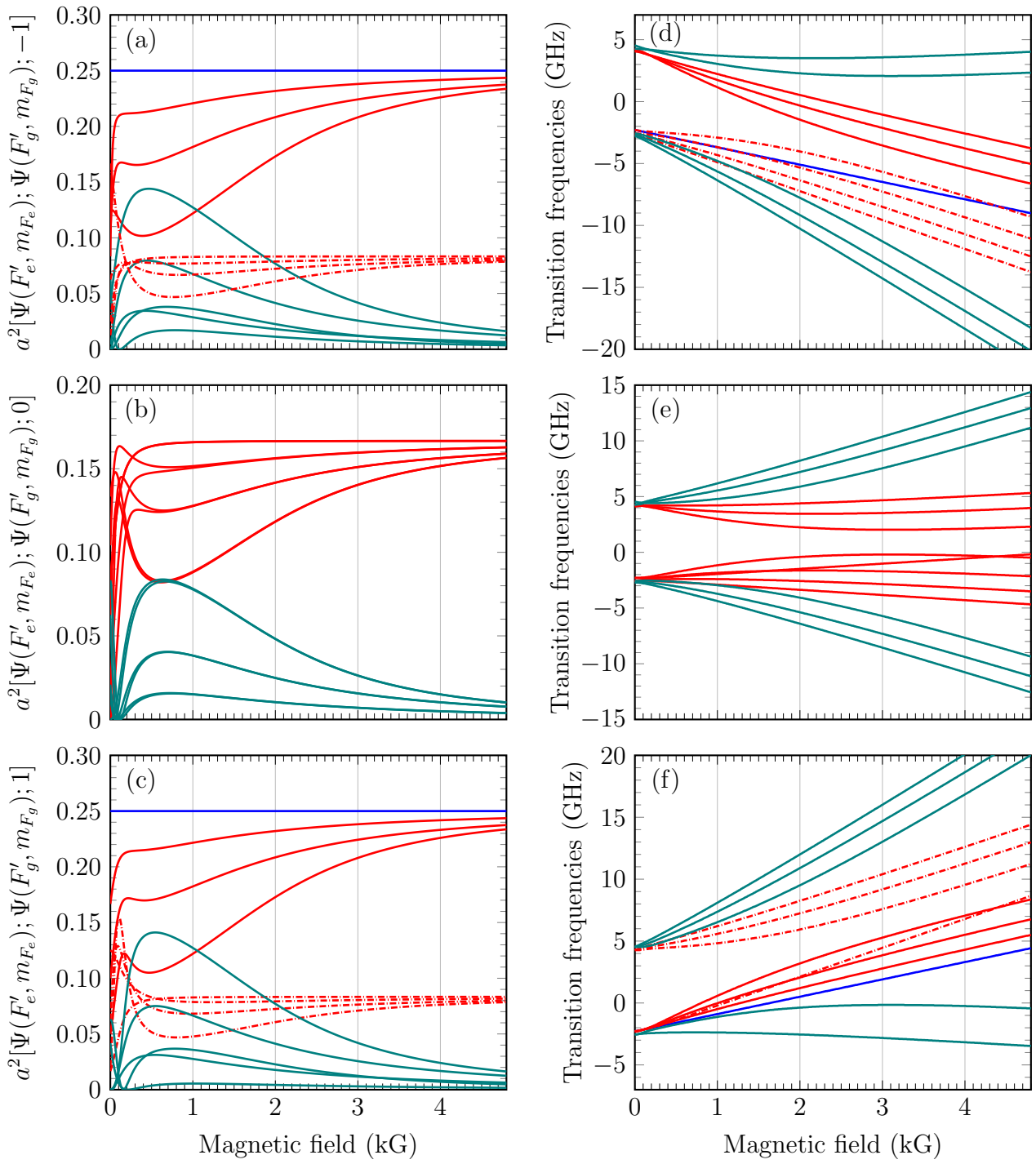

Figure 3.5: ^{87}Rb D_2 line dipole moments (a-c) and transition frequencies (d-f) as a function of the magnetic field. On panels (d-f), the zero frequency corresponds to the weighted center of the ^{87}Rb $5S_{1/2} \rightarrow 5P_{3/2}$ line. The transition frequencies and dipole moments for transitions remaining in the Paschen-Back regime split in two groups, indicated either with red solid or dash dotted lines; the dark green solid lines correspond to transitions whose dipole moments experience large increase followed by a large decrease with increasing magnetic field. The blue solid lines indicate transitions whose dipole moments are invariant with changes in magnetic field.

3.2.3 Magnetic field-induced circular dichroism in Rb vapors

Magnetic circular dichroism (MCD) in an atomic medium for right and left circularly polarized radiations attracts growing attention due to numerous applications. A strong MCD has been measured for the number of electrons ejected by ionization of atomic helium using right-polarized light [100]. Fundamental interest towards MCD is particularly connected with studies of parity violation in optical experiments with heavy atoms see e.g. [100, 101, 102, 103]. As was suggested by Angstmann *et al.* (2005) [103], the Zeeman transitions are more suitable for precise measurements of parity non-conservation induced by nuclear spin-dependent interaction than hyperfine ones. While it was not demonstrated experimentally before Tonoyan *et al.* (2018) [47] have made a study based on the investigation of Zeeman transitions which makes a significant step forward towards solving this outstanding problem.

In a particular range of external magnetic field, alkali D_2 lines contain two groups of transitions which are "forbidden" by the $\Delta F = 0, \pm 1$ total atomic angular momentum selection rule at zero magnetic field. The application of a magnetic field causes mixing of states, inducing transitions between the states with $\Delta F = \pm 2$ [88]. It is a conditional notation because neither $|F, m_F\rangle$, nor $|m_I, m_J\rangle$ bases are applicable in the intermediate range of the magnetic field. For the case of Rb, these transitions are $F_g = 2 \rightarrow F_e = 4$ and $F_g = 3 \rightarrow F_e = 1$ for ^{85}Rb, and $F_g = 1 \rightarrow F_e = 3$ and $F_g = 2 \rightarrow F_e = 0$ for ^{87}Rb. The transitions obeying the selection rules $\Delta F = +2$ (first group) and $\Delta F = -2$ (second group), behave distinctly depending on whether the excitation radiation is σ^+ ($\Delta m_F = +1$) or σ^- ($\Delta m_F = -1$) polarized.

Here-after, we study theoretically magnetic field-induced circular dichroism in Rb vapors and show that an asymmetric circular dichroism occurs for low and intermediate magnetic fields while the symmetry is recovered in the Paschen-Back regime. Particularly, we show that for the first group (obeying $\Delta F = +2$) the strongest transition probability for the case of σ^+ is around four times higher than that for σ^-, while for the second group (obeying $\Delta F = -2$) the strongest transition probability in the case of σ^- is few orders of magnitude times higher than that for σ^+. In other words, in the first group for the case of σ^+ radiation, transitions are stronger than in the case of σ^-, whereas in the second group the transitions are stronger for the case of σ^- polarization. This difference leads to a circular dichroism.

Symmetric magnetic circular dichroism

Let us first investigate MCD in the Paschen-Back regime of ^{85}Rb D_2 line. As can be seen from Fig. 3.4, in the case of circular polarization (top and bottom panels) only eight transitions remain in the spectrum at sufficiently high magnetic field; they split in two groups of different amplitude. Comparing Fig. 3.4(a) and (c) for magnetic fields larger than 2 kG, one sees that the transitions follow the same behavior for both circular polarizations. However, when making the same comparison for the transition frequencies (see Fig. 3.4(d) and (f)), one observe that σ^- transitions shift toward lower frequencies while σ^+ transitions shift toward higher frequencies. In both cases, transitions of each groups shift with the same absolute value of about 2.33 MHz G^{-1} (stronger groups) and 1.39 MHz G^{-1} (weaker groups) [104], leading as a consequence to symmetry with respect to the frequency position of the $5S_{1/2} \rightarrow 5P_{3/2}$ line. For this reason, we qualify such MCD as symmetric (with respect to frequency).

To illustrate these conjectures, we show in Fig. 3.6 the calculated dSR spectrum of ^{85}Rb D_2

line simultaneously excited by left and right circular polarizations at $B = 9$ kG. We demonstrate the complete mirror symmetry in the HPB regime by calculating the D_2 line dSR spectra of ^{85}Rb for in the case of circularly polarized excitation. As is clearly seen, the groups of the σ^+ and σ^- polarized transitions exhibit mirror symmetry with respect to the zero detuning frequency. This behavior is emphasized in the inset, where the σ^- spectrum has been calculated as a function of $-\omega$, demonstrating almost complete overlap of both σ^+ and σ^- spectra.

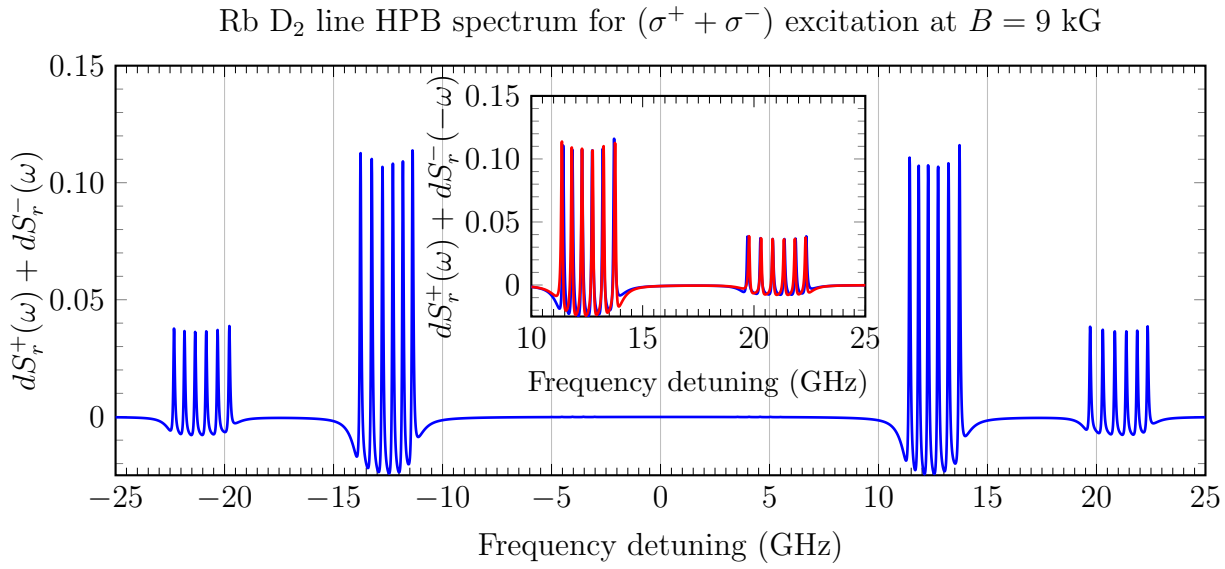

Figure 3.6: Calculated dSR spectra of the ^{85}Rb D_2 line for $B = 9$ kG in the case of simultaneous σ^+ and σ^- excitation. The zero-detuning-frequency position corresponds to the weighted center of the $5S_{1/2} \rightarrow 5P_{3/2}$ line. The inset illustrates the "mirror" overlap of the σ^- (red lines) and σ^+ (blue lines) spectra when the σ^- spectrum is calculated as a function of $-\omega$. The slight discrepancies arise from the non-symmetric profile of SR.

Asymmetric magnetic circular dichroism

In this section, we study the circular dichroism for MI transitions of ^{85}Rb and ^{87}Rb D_2 lines. The complete calculated spectra of the D_2 lines of the Rb for σ^+ (top panels) and σ^- (lower panels) polarizations are shown in Fig. 3.7. While the left panels of Fig. 3.7 represent the low-frequency parts of the D_2 lines containing the second group transitions at 500 G, the right panels of Fig. 3.8 represent the high-frequency part of the D_2 lines containing the first group transitions at 650 G. Only the strongest eight out of 24 MI transitions are labeled corresponding to the transition diagrams in the insets. The curves are obtained using the procedure described in section 3.2.1. It was verified in [47] that the mismatch of the theory and experiment is less than 5%.

At zero and $B \gg B_0$ magnetic fields, the intensities of the labeled transitions are almost zero, while in the presence of intermediate magnetic fields, as we see, some of them are strongly enhanced. From the comparison between left top and bottom panels of Fig. 3.7, one obviously sees that the intensities of the $\Delta F = -2$ group MI transitions at 500 G for σ^- polarization are about 10^5 times bigger than for σ^+ polarization, whereas comparing panels (b) and (d) the

intensities of the $\Delta F = +2$ group MI transitions at 650 G for σ^+ polarization are greater about 4 times than for σ^- polarization. These two observations lead to a conclusion that there is a definite range of magnetic field when evident asymmetric circular dichroism exists.

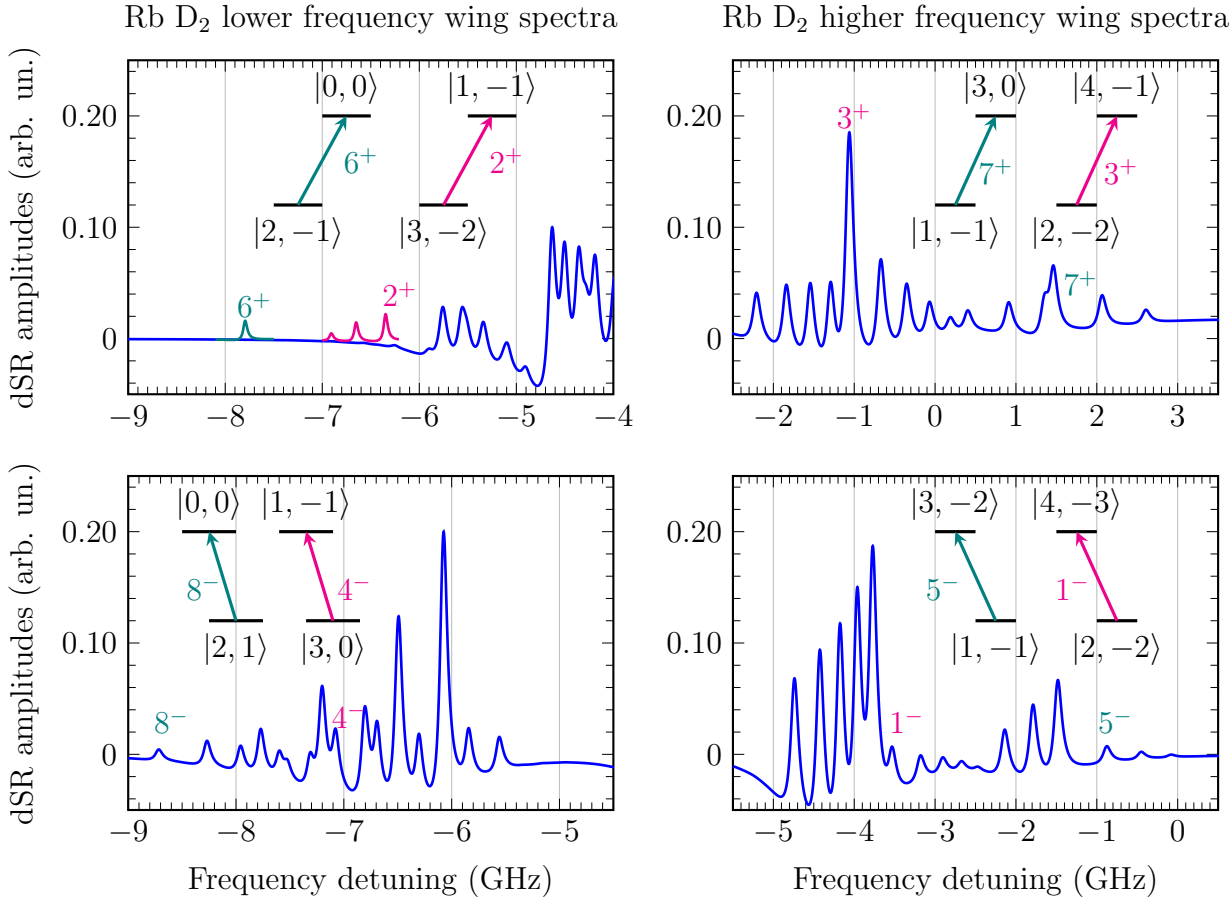

Figure 3.7: Theoretical dSR spectra of Rb D_2 line. The labels + and − stand for σ^+ and σ^- transitions, respectively. Odd numbers stand for the $\Delta F = -2$ group, even numbers for the $\Delta F = +2$ group. Peaks are labeled according to the diagrams. The low-frequency part of the spectra (left panels) for σ^+ (top) and σ^- (bottom) polarization is calculated for $B = 500$ G; the high-frequency part of the spectra (right panels) for σ^+ (top) and σ^- (bottom) calculated for $B = 650$ G. The insets of the top left panel show three MI transitions of ^{85}Rb $F_g = 3 \to F_e = 1$ (magenta), and one MI transition of ^{87}Rb $F_g = 2 \to F_e = 0$ (dark green), which appear in the theoretical spectrum only when magnified by 10^5 and 10^4 respectively.

We emphasize the distinctions between σ^+ and σ^- excited MI transition probabilities in each group by showing the dynamics of the ratios of transition probabilities depending on the B-field in Fig. 3.8(a). The magenta lines correspond to the ratio of the probabilities $3^+/1^-$ and $4^-/2^+$ MI transitions for ^{85}Rb and the dark green lines correspond to the ratio of the $7^+/5^-$ and $8^-/6^+$ transitions probabilities for ^{87}Rb. A^+ and A^- stand for the transitions intensities for the σ^+ and σ^- excitations, respectively. We should note that for the observed range of magnetic fields, when there is a mixing of states, neither $|F, m_F\rangle$, nor $|m_I, m_J\rangle$ bases are appropriate to denote these

transitions, however, $\Delta F = \pm 2$ notation allows to follow the behavior of specific transitions.

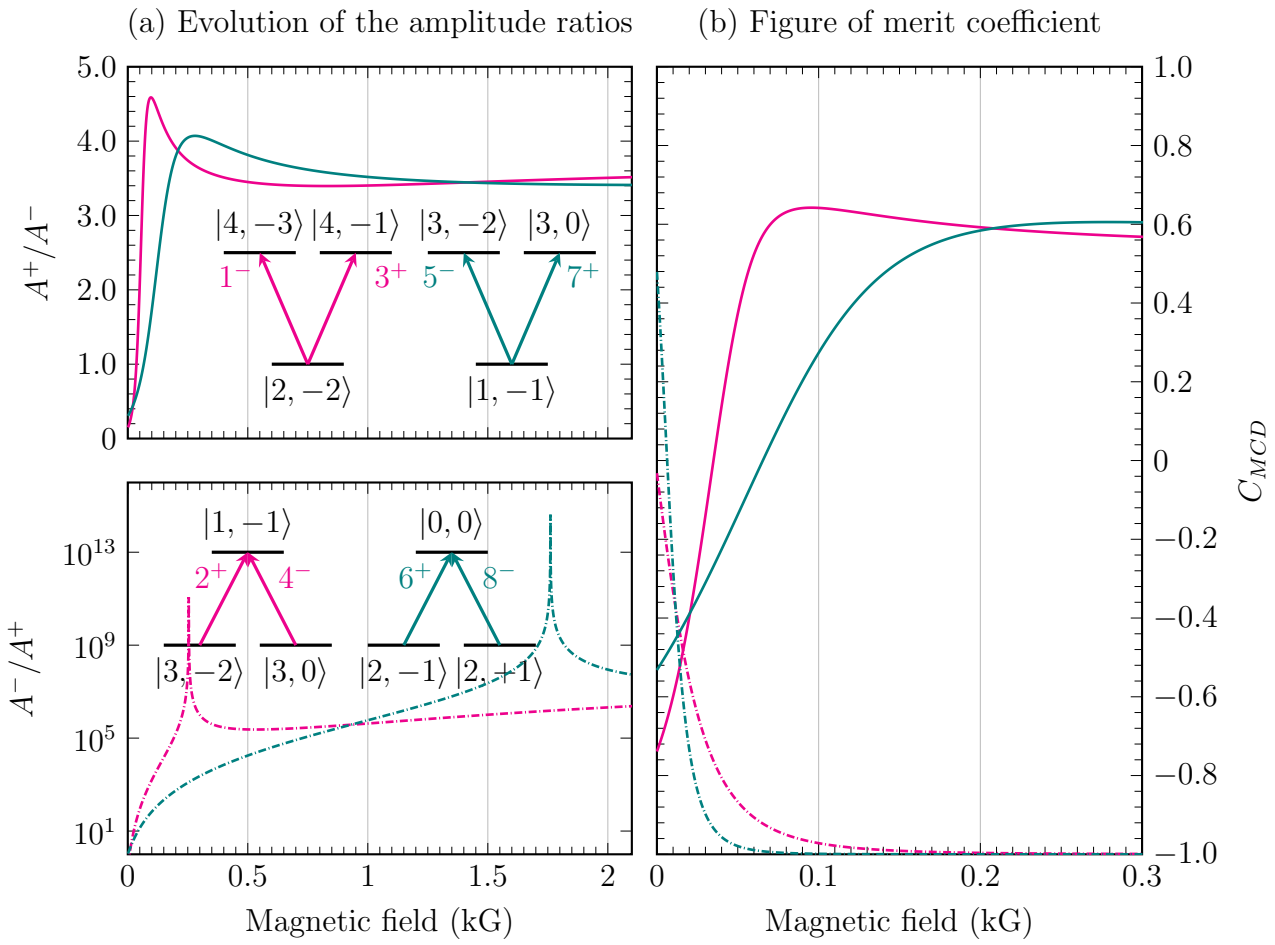

Figure 3.8: (a) Theoretical B-field dependence of the ratio of the strongest in its group MI transition probabilities. Magenta and dark green lines are for ^{85}Rb and ^{87}Rb, respectively. (a) $A^+(3^+)/A^-(1^-)$ and $A^+(7^+)/A^-(5^-)$ (top panel); $A^-(4^-)/A^+(2^+)$ and $A^-(8^-)/A^+(6^+)$ (bottom panel). The diagrams of the corresponding MI transitions of ^{85}Rb and ^{87}Rb are shown in the insets. (b) Magnetic-field dependence of the MCD figure of merit coefficient C_{MCD} for the strongest in its group magnetic-induced transitions of ^{85}Rb and ^{87}Rb.

The ratio A^+/A^- of the transition probabilities for the first group reaches almost five, demonstrating the existence of dichroism; moreover, for the second group the ratio A^-/A^+ reaches up to 10^{14}. Such difference in each group results in circular dichroism. The revealed phenomenon is termed as "frequency-controllable MCD", since by varying the laser field frequency and polarization, it is possible to switch the dominating transition intensity from σ^+ (for $\Delta F = +2$ MI transitions) to σ^- (for $\Delta F = -2$ MI transitions).

To describe the dichroism quantitatively, we introduce the figure of merit coefficient C_{MCD}, defined as

$$C_{MCD} = \frac{A^+ - A^-}{A^+ + A^-}. \tag{3.45}$$

The magnetic-field dependence of C_{MCD} for each group and for ^{85}Rb (magenta) and ^{87}Rb (dark green) are plotted in Fig. 3.8(b). The solid lines correspond to the $\Delta F = +2$ groups and the dashed lines correspond to the $\Delta F = -2$ groups. The value $C_{MCD} = 0$ demonstrates the equality or symmetry of the σ^+ and σ^- transitions intensities, while $C_{MCD} > 0$ or $C_{MCD} < 0$ indicates the presence of a stronger transition intensity for the σ^+ or σ^- excitation, respectively, *i.e.*, asymmetry. The outermost values $C_{MCD} = \pm 1$ correspond to the complete suppression of the transition intensity to zero for the σ^- or σ^+ excitations, accordingly. The highest negative value $C_{MCD} = -1$ is reached at $B > 80$ G for the transition $F_g = 3 \rightarrow F_e = 1$ transition of ^{85}Rb, and at $B > 200$ G for the $F_g = 2 \rightarrow F_e = 0$ transition of ^{87}Rb, manifesting complete vanishing of the σ^+ MI transition. The highest positive value of C_{MCD} for the $F_g = 2 \rightarrow F_e = 4$ transition of ^{85}Rb and the $F_g = 1 \rightarrow F_e = 3$ transition of ^{87}Rb always stays below +1, approaching only to 0.6.

Dipole moment cancellation

In Fig 3.8, we have unveiled a very particular behavior of the ratio of MI transitions: the ratio $A^-(4^-)/A + (2^+)$ reaches up to 10^{14}. To reach such a high value, the only physical solution is for the denominator to be extremely small. Indeed, the squared transfer coefficient (3.38) is bounded by unity.

To go further, we have plotted in Fig. 3.9, the squared transfer coefficients of ^{87}Rb D_2 line transitions, which are part of transitions we have discarded in Figs. 3.5 due to their small amplitudes, as a function of the magnetic field. We limit our analysis to the case of ^{87}Rb D_2 line σ^+ transitions which has less transitions than that of ^{85}Rb. One can see that some of the transitions exhibit an extremely sharp dip below 10^{-2}. While decreasing the sampling of magnetic field (*e.g.* increasing the step of calculations, we have seen that the amplitude of the peak reduces, which seems to be linked with clipping. In the opposite case, increasing the sampling of magnetic field increases the amplitude of the peaks: it thus seems that for a particular value of magnetic field, the dipole moment cancels. We also observe that it occurs at different values for each of these specific transitions. It is however not possible to go much below 10^{-15} as all the constants used to perform the calculations, e.g. the Bohr magneton, are known with a finite precision.

To verify that this behavior has a physical meaning and is not caused by peculiarities of numerical calculation, we have carefully checked that the evolution of the transfer coefficient (without the square) crosses the abscissa axis (change of sign). This behavior was indeed observed, which confirms that the predicted dipole moment cancellation is not a numerical artifact. Unfortunately, it was not possible to show the axis crossing explicitly with a log plot as the transfer coefficient changes to negative values.

To propose a physical explanation of this phenomenon, let us first examine the expression of the transfer coefficients. As the phenomenon occurs for a given value of the magnetic field, what trigger the cancellation should also be magnetic field dependent. From Eq. (3.38) and (3.39), one sees that only the mixing coefficient $\chi_{F'F}$ is function of the magnetic field. Thus the dipole moment cancels for a very particular mixing of states, which could be viewed as quantum interference.

As was seen, the value of the dipole moment can reach extremely small value, tunable by

magnetic field. This effect can be used to refine fundamental constants such as the Bohr magneton. However such a small signal can never be recorded in the experiment knowing the real signal-to-noise ratio.

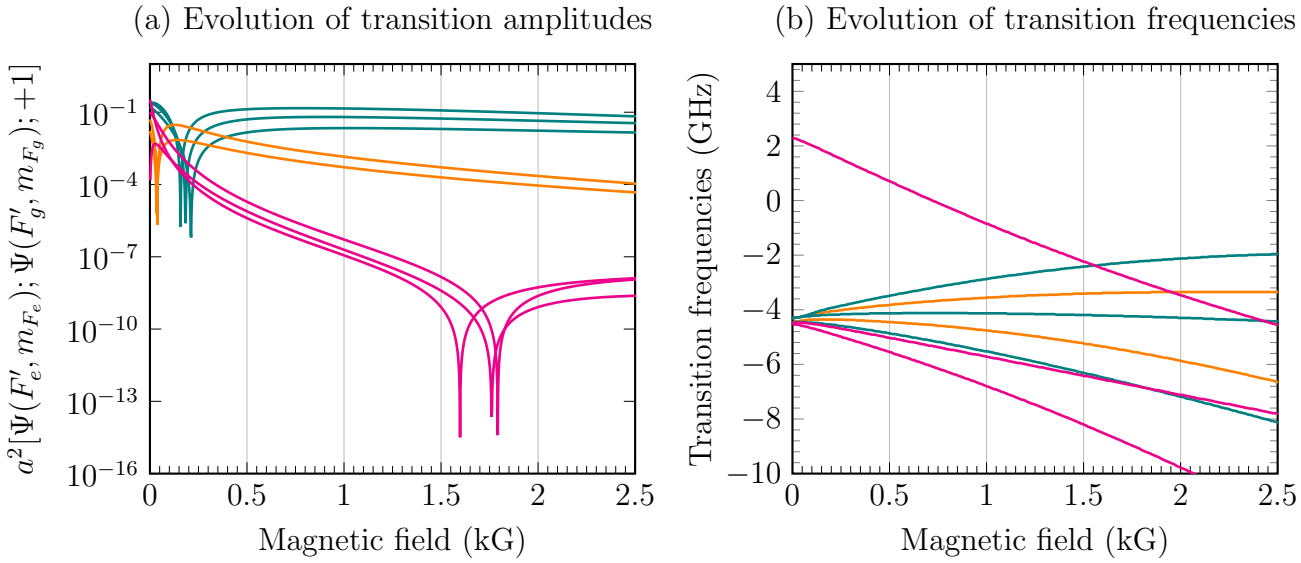

Figure 3.9: (a) Evolution of the ^{87}Rb D_2 line σ^+ transition dipole moments as a function of the magnetic field. These transitions experience a cancellation at around 0.05 kG, 0.2 kG and 1.7 kG. (b) Evolution of the frequencies of transitions experiencing a cancellations.

3.3 Experimental study

We now focus our attention toward experimental investigations of alkali vapor spectra, particularly Rb and K vapors confined in NC, when a longitudinal magnetic field is applied. We present a typical experimental layout allowing to explore alkali atom – magnetic field interaction covering the range from Zeeman to Paschen-Back regime. Following the discussion of section 3.2.3, we study experimentally the behavior of Rb MI transitions for intermediate magnetic fields. Later, we make a complete polarization study of K D_2 line HPB regime, and show that the HPB regime is achieved at relatively low magnetic field as compare to other alkalis.

The magnetic field can be applied in various ways; a pair of Helmholtz coils is convenient as the created magnetic field in between can be quite homogeneous, but this system usually fails to produce higher magnetic fields than 200 G due to the need of high electric current. To achieve stronger magnetic fields, the easiest way is to bring a strong permanent magnet close to the cell. However, let us recall that we have supposed a uniform magnetic field in the model of section 3.1. In the case of strong permanent magnet, one can question this assumption. Nonetheless, the interaction of atoms with a laser radiation field in NC occurs in a nanometric-thickness size in a longitudinal direction, and one may consider this hypothesis of uniformity as valid. The quality of the agreement of theory with experiment will let us conclude on this assumption.

3.3.1 Experimental arrangement

Figure 3.10(a) shows the layout of the experimental setup. A VitaWave© frequency-tunable cw narrowband extended cavity diode laser protected by a Faraday isolator, emits a linearly polarized radiation directed at normal incidence onto a NC mounted inside the oven. A quarter-wave plate, placed in between the FI and the NC, allows to switch between left-hand and right-hand circularly-polarized radiation. The necessary vapor density $N \sim 10^{13}$ cm^{-3} is attained by heating the cell's thin sapphire reservoir containing metallic alkali to $\Theta_r \sim 150$ °C [25] while keeping the window temperature some 20 °C higher.

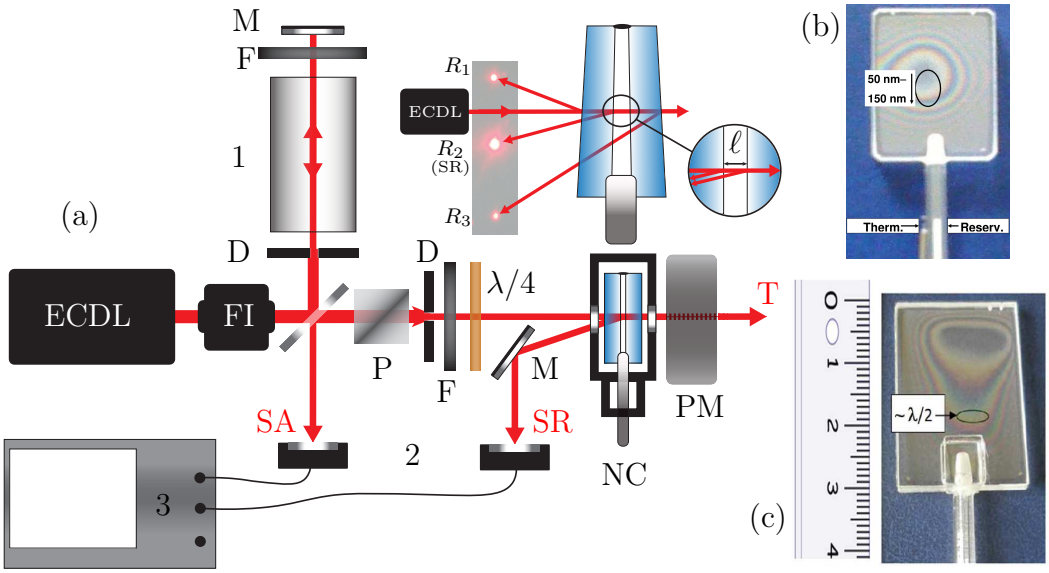

Figure 3.10: (a) Layout of the experimental setup: ECDL – cw tunable extended cavity diode laser, FI – Faraday insulator, NC – nanocell in the oven, 1 – frequency reference cm-long cell, 2 – photodetectors, 3 – oscilloscope, P – polarizer, D – diaphragm, F – filter, $\lambda/4$ – quarter-wave-plate, SR – selective reflection channel, SA – saturated absorption channel, T – transmitted beam. The inset shows the geometry of three reflected beams from the NC; the selective reflection beam propagates in the direction of R_2. (b) Photograph of a K-filled nanocell; the oval marks the region 50 – 150 nm. (c) Photograph of a Rb-filled nanocell where the region $\ell \sim \lambda/2$ is marked. The cm-graduated ruler on the side roughly gives the size of the NC.

A longitudinal magnetic field $\mathbf{B} \parallel \mathbf{k}$, where $\mathbf{k}$ is the wavevector of the laser radiation, is applied using a permanent neodymium-iron-boron alloy ring magnet placed near the output window of the NC. In this configuration, the magnetic field in the NC could reach up to 2 kG using a translation stage. The variation of the field strength was achieved by axial displacement of the magnet system and was monitored by a calibrated magnetometer "Teslameter HT201". In spite of a strong spatial gradient of the field produced by the permanent magnet, the variation of B-field inside the interaction region is negligible as compared to the amplitude of B [105]. The right insets of Fig. 3.10 show the photographs of the K (b) and Rb (c) NC where one can see interference fringes formed by light reflection from the inner surfaces of the windows because

of variable thickness ℓ of the vapor column across the aperture. The inset of Fig. 3.10(a) shows geometry of the reflected laser beams.

Although the decrease of ℓ improves the spatial resolution, which is very important when using high-gradient field permanent magnets, it simultaneously results in a broadening of the SR spectral linewidth; therefore the thickness $\ell \sim 350$ nm appears as the optimal thickness. This additional broadening is a result of atom-wall collisions: the reduction of the thickness ℓ between the windows shortens the flight time of atoms toward the surface, making atom-wall collisions more frequent and leading to additional broadening. To form a frequency reference, a part of the laser radiation was branched to an auxiliary SA setup formed in a cm-long cell filled with the same alkali as the NC.

3.3.2 Modification of selection rules for Rb D_2 line

For moderate magnetic field, the splitting of atomic energy levels to Zeeman sublevels deviates from the linear behavior, and the atomic transition probabilities undergo significant changes, see section 3.2.2. The most simple technique to monitor and study such modification is laser spectroscopy of atoms contained in an atomic vapor cell. For magnetic fields up to 1 kG, the Zeeman split hyperfine transitions remain overlapped because of Doppler broadening, and sub-Doppler techniques are required to spectrally resolve transition probabilities of individual components [88].

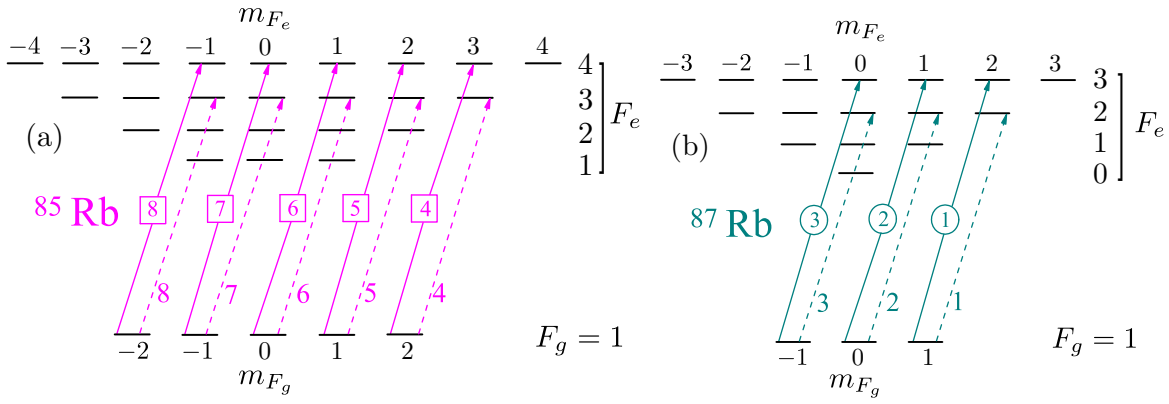

Figure 3.11: Diagram of the relevant transitions between the Zeeman sub-levels of Rb D_2 line with σ^+ laser excitation for the case of (a) ^{85}Rb (nuclear spin $I = 5/2$), and (b) ^{87}Rb (nuclear spin $I = 3/2$). Each transition is labeled to facilitate identification in the following graphs.

In chapter 2, we have seen that the dSR method achieves strong line narrowing and yields signal proportional to atomic transition probabilities. In addition, the dSR resonance linewidth is practically immune against 10% deviation of the cell thickness. These benefits make the dSR-method convenient for studies of closely-spaced individual atomic transition components in a magnetic field. We demonstrate here-after that the dSR linewidth for Rb D_2 line is about 50 MHz FWHM as opposed to 500 MHz Doppler absorption linewidth in ordinary cells, allowing frequency separation of individual Zeeman components of hyperfine transitions and studying their transition probabilities in an external magnetic field. We monitor the dynamics of giant

modification of transition probabilities of $5S_{1/2} \rightarrow 5P_{3/2}$, $F_g = 2 \rightarrow F_e = 4$ and $F_g = 1 \rightarrow F_e = 3$ MI transitions of Rb D_2 line induced by a magnetic field varied in a large range up to 1 kG. These particular transitions should receive interest since they are forbidden at $B = 0$ according to $\Delta F = 0, \pm 1$ selection rule for the total momentum of atom.

To perform this study, we have used the setup of Fig. 3.10, where a circularly polarized laser radiation beam ($\lambda = 780$ nm, $P_L = 0.2$ mW, $\Delta\nu_L = 1$ MHz) resonant with Rb D_2 line was focused ($\varnothing = 0.5$ mm) at normal incidence angle onto a Rb NC with a vapor column thickness $\ell \approx 300$ nm filled with natural Rb (72.8% of ^{85}Rb and 27.2% ^{87}Rb). This optimum thickness was chosen to combine high spatial resolution, which is very important when using high-gradient field from permanent magnet, with acceptable broadening of the SR spectral linewidth (the latter increases with reduction of ℓ).

The diagram of relevant σ^+ components of ^{85}Rb D_2 line transitions $F_g = 2 \rightarrow F_e = 3$ labeled 4 – 8, and $F_g = 2 \rightarrow F_e = 4$ labeled $\boxed{4} - \boxed{8}$ are shown in Fig. 3.11(a), where the transitions $\boxed{4}$–$\boxed{8}$ are MI transitions. Equivalent diagram for ^{87}Rb transitions is shown in Fig. 3.11(b), where ① – ③ are MI transitions. The transitions $F_g = 2 \rightarrow F_e = 1, 2$ (^{85}Rb) and $F_g = 1 \rightarrow F_e = 0, 1$ (^{87}Rb) are not shown in Fig. 3.11, since for $B > 300$ G their probabilities strongly reduce, making them practically undetectable in the dSR spectra. Note that in the case of σ^- excitation, the $F_g = 2 \rightarrow F_e = 4$ transitions of ^{85}Rb and $F_g = 1 \rightarrow F_e = 3$ transitions of ^{87}Rb have smaller dSR amplitudes than for the case of σ^+ for the same B values.

Figure 3.12 shows the recorded dSR spectra (red dots) from the Rb NC with thickness $\ell \approx 300$ nm for a σ^+ laser excitation, for $B = 335$ G, 450 G, 580 G and 855 G. The corresponding theoretical curves are plotted with blue solid lines. The sixteen transition components (for labeling, see Fig. 3.11) appear with a 60 MHz linewidth, being very well resolved. As it is seen, the amplitudes of transitions $\boxed{7}$ and $\boxed{8}$ are the strongest among the transitions of ^{85}Rb $F_g = 2 \rightarrow F_e = 1, 2, 3, 4$ up to $B \approx 600$ G. Magnetic field dependences of the frequency shifts and the relative probabilities of $\boxed{4} - \boxed{8}$ and 4 – 8 transitions of ^{85}Rb, as well as of ① – ③ and 1 – 3 transitions of ^{87}Rb for the case of σ^+ excitation are shown in Fig. 3.13.

When $B \gg B_0$, the coupling of $\mathbf{J}$ and $\mathbf{I}$ ceases, and the splitting is better described by the projections m_J and m_I. The latter manifests the onset of hyperfine Paschen-Back regime characterized by a number of peculiarities [3, 104, 106], see also section 3.3.3. Particularly, probabilities of the eight above mentioned MI transitions reduce back to zero when $B \gg B_0$, so they are absent in the m_J and m_I basis. Note that the probabilities of ^{85}Rb transitions labeled $\boxed{4} - \boxed{8}$ reduce faster with B than the transitions ① – ③ of ^{87}Rb (see Fig. 3.13). This is caused by the fact that B_0 value for ^{87}Rb is larger that for ^{85}Rb, consequently HPB regime for ^{87}Rb occurs at larger magnetic fields. In total twenty atomic transitions remain in the complete HPB regime, 12 belonging to ^{85}Rb, and 8 belonging to ^{87}Rb [104].

Good agreement between the theory and experiment is observed throughout the whole explored range of magnetic fields, which proves complete consistency of the theoretical model. It should be noted that the calculations performed for other forbidden transitions of Rb D_2 line ($F_g = 3 \rightarrow F_e = 1$ of ^{85}Rb and $F_g = 2 \rightarrow F_e = 0$ of ^{87}Rb) show a weak modification of the transition probabilities, several orders less than that for $F_g = 2 \rightarrow F_e = 4$ of ^{85}Rb and $F_g = 1 \rightarrow F_e = 3$ of ^{87}Rb, so that their experimental study is restricted by extremely small signal-to-noise ratio. Let us remember that we have explored their behavior theoretically in section 3.2.3, and unveiled an asymmetric magnetic circular dischroism and a dipole moment

cancellation effect.

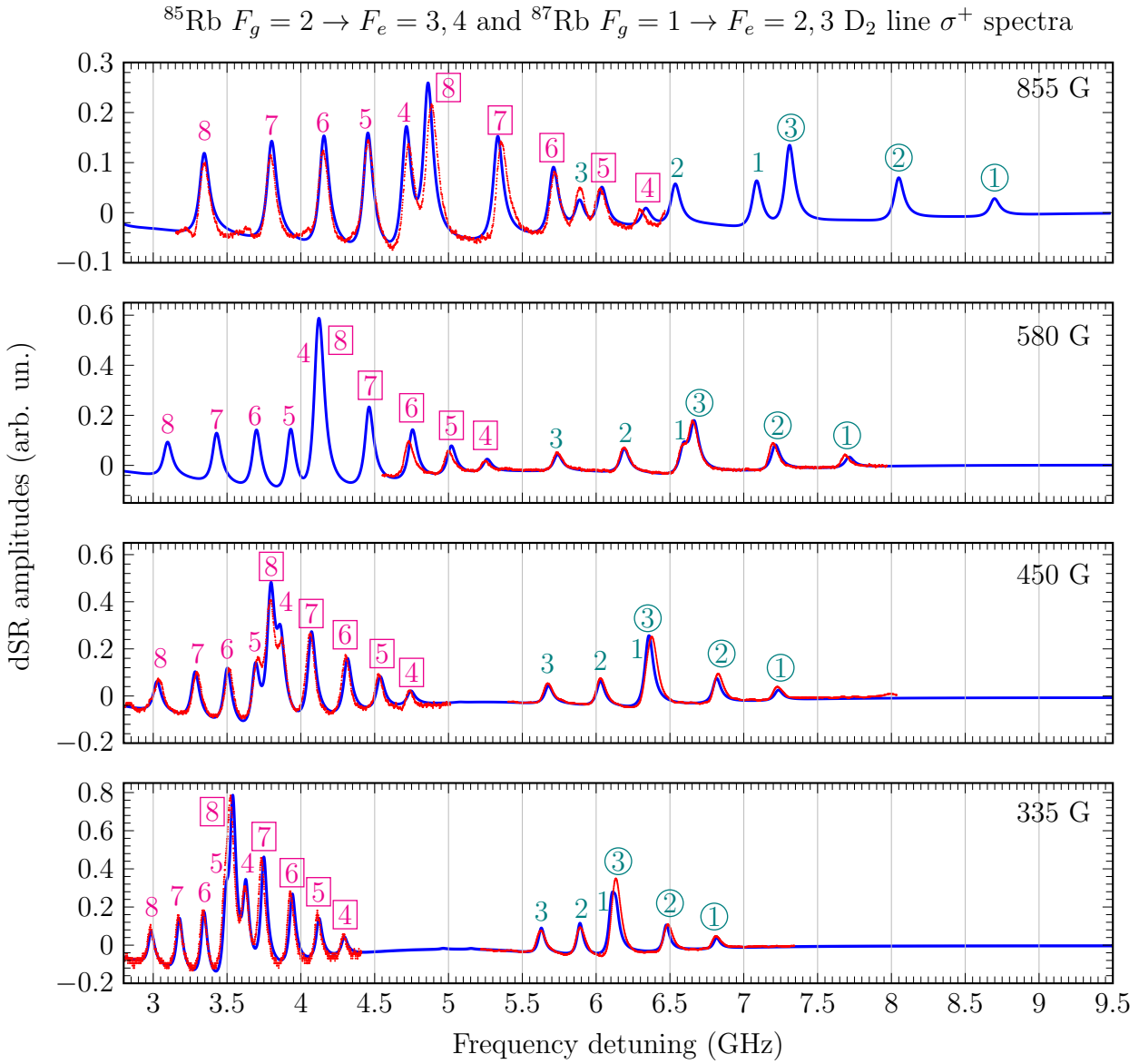

Figure 3.12: Experimental (red dots) and calculated (blue lines) Rb D_2 line dSR spectra for the thickness $\ell \approx 300$ nm, excited with σ^+ polarized laser radiation ($P_L = 0.1$ mW). The values of applied B-field are: 335 G, 450 G, 580 G and 855 G (bottom to top). For labeling, see Fig. 3.11. Fragmentary presentation of experimental spectra is caused by mode hop-restricted continuity of the laser frequency scanning, verified with a Fabry-Pérot cavity signal (not shown). The small discrepancies, visible for example on peak $\boxed{6}$ (580 G), could arise from slight non-linearity in the experimental frequency scanning of the laser diode. The frequency inaccuracy between experiment and theory is about 2%, while the inaccuracy of the line intensities is about 5%.

The results of this study can be used for developing hardware and software solutions for wide-range optical magnetometers with sub-μm local spatial resolution, as well as widely tunable

frequency reference system based on a NC and strong permanent magnets. Besides, formation of narrow optical resonances far away from the atomic transition (up to 20 GHz for strong B-field) allows realization of widely tunable laser frequency lock [67, 107]. Owing to small divergence of selective reflection radiation beam, which follows the divergence of incident radiation, the dSR signal can be easily detected at large distance ($\sim$ 10 m) from the NC, which could be used for the remote optical monitoring of magnetic field.

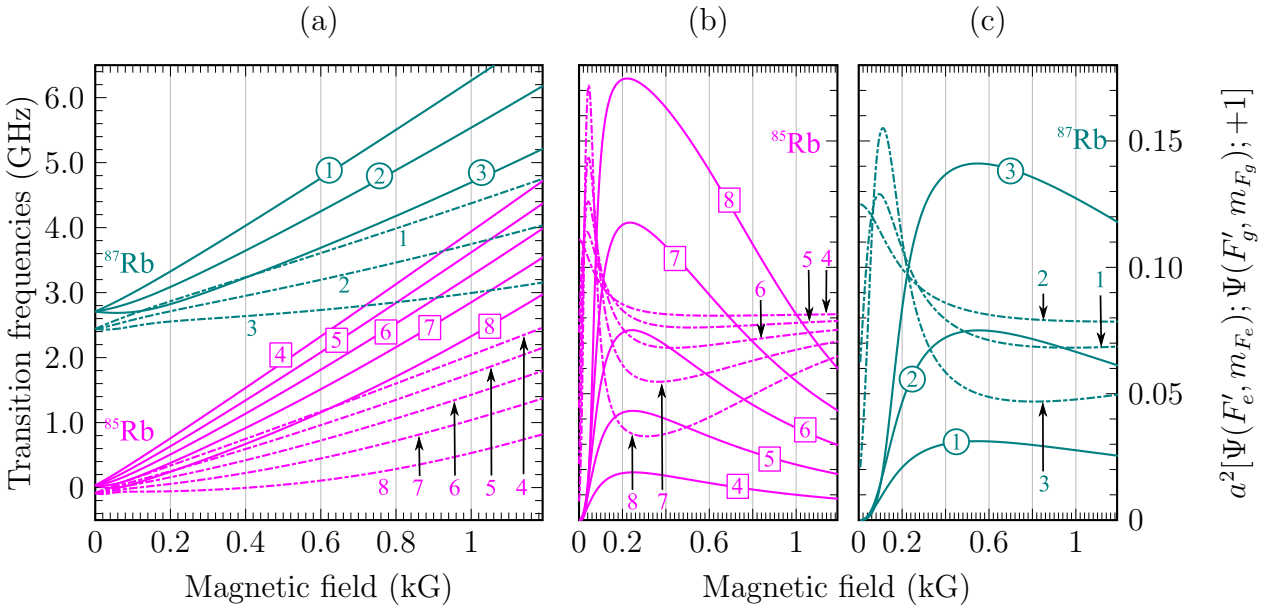

Figure 3.13: (a) Calculated magnetic field dependence of frequency shifts for Zeeman components of $F_g = 2 \to F_e = 3, 4$ transitions of ^{85}Rb D_2 line and $F_g = 1 \to F_e = 2, 3$ transitions of ^{87}Rb D_2 line for the case of σ^+ excitation. (b) Theoretical evolution of probabilities for Zeeman components of $F_g = 2 \to F_e = 3, 4$ transitions (^{85}Rb) versus B-field for σ^+ excitation. (c) Theoretical evolution of probabilities for Zeeman components of $F_g = 1 \to F_e = 2, 3$ transitions (^{87}Rb) versus B-field for σ^+ excitation. For labeling, see Fig. 3.11.

3.3.3 K D_2 line in the Paschen-Back regime

For a temperature about 100 °C, the Doppler-broadening of K vapors is around 0.9 GHz exceeding the hyperfine splitting of the ground and excited levels such that the transitions $F_g = 1, 2 \to F_e = 0, 1, 2, 3$ of ^{39}K are completely masked by the Doppler-profile. Therefore, K atomic vapor usually receive less interest as compared to Rb or Cs ones and only a small number of papers can be found: the accurate identification of atomic transitions of K was reported in [108, 109]; saturated absorption spectra of the D_1 line of potassium atoms have been studied in details both theoretically and experimentally in [63]. Potassium vapors were used for the investigation of nonlinear magneto-optical Faraday rotation in an antirelaxation paraffin-coated cell [110], polarization spectroscopy and magnetically-induced dichroism for magnetic fields in the range of 1 – 50 G [111], formation of dark resonance having a sub-natural linewidth [112],

electromagnetically induced transparency [113] and four-wave mixing process [114]. A theory describing the transmission of Faraday filters based on sodium and potassium vapors is presented in [115]. Feshbach resonances in ultracold ^{39}K have been reported in [116].

In external magnetic field, the additional splitting of energy levels causes the formation of a number of atomic transitions spaced by a frequency interval of 100 MHz in the HPB regime. Besides, the particularity of ^{39}K is a small characteristic value of magnetic field $B_0 = 165$ G in contrast to other alkalis such as ^{133}Cs ($B_0 = 1700$ G) and ^{85}Rb ($B_0 = 700$ G), ^{87}Rb ($B_0 = 2400$ G) isotopes [3, 106, 117, 118]. Hence, there is a significant change in atomic transition probabilities of ^{39}K D_2 line for relatively small magnetic fields, at least by an order of magnitude smaller as compared to other alkalis. That is why a Doppler-free method must be implemented to perform an efficient study of atomic transitions of K vapors.

Investigation of the modification of the transition frequencies and probabilities for K D_1 line using absportion spectroscopy from a NC was reported in [119]. The small number of atomic transitions (four for each circular polarisation) and the narrowing of the spectra occuring at $\ell = \lambda/2 = 385$ nm [79] (coherent Dicke narrowing, see section 2.2.2) were the reasons why the resolution of the recorded spectra was sufficient. However, due to a larger number of atomic transitions (eight) formed by circularly-polarized laser radiation, absorption spectra of K D_2 line in NC are strongly broadened.

For these reasons, we investigate here-after the HPB of K D_2 line using the dSR-method. We make use of the experimental setup depicted on Fig. 3.10 to perform a complete polarization analysis of the K D_2 line in HPB regime, where a quarter-wave plate allows to select either σ^+ or σ^- polarizations in the $\mathbf{B} \parallel \mathbf{k}$ configuration; the π polarization analysis is achieved in the $\mathbf{B} \parallel \mathbf{E}$ configuration while removing the quarter-wave plate. The NC used in the experiments was filled with natural potassium vapors (93.3% of ^{39}K and 6.7% of ^{41}K).

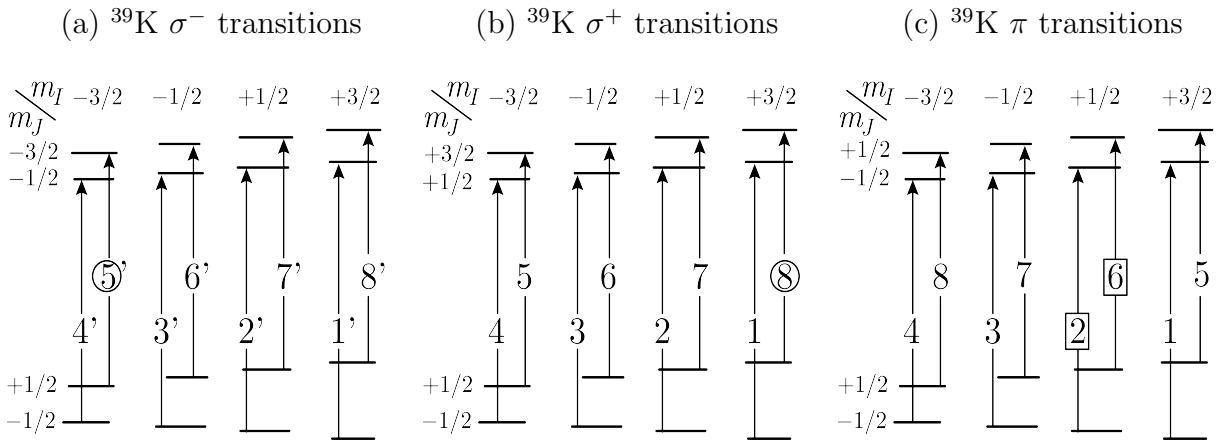

Figure 3.14: Potassium 39 D_2 line transition diagrams in the case of (a) σ^- polarization, (b) σ^+ polarization and (c) π polarization. Diagrams are drawn for the uncoupled basis.

Circular polarization analysis

Left panels of figure 3.15 show the experimental (red dots) and theoretical (blue solid lines) spectra in the case of σ^- polarized laser radiation for five different values of the applied longitudinal

magnetic field, from bottom to top: 500, 690, 720 and 780 G.

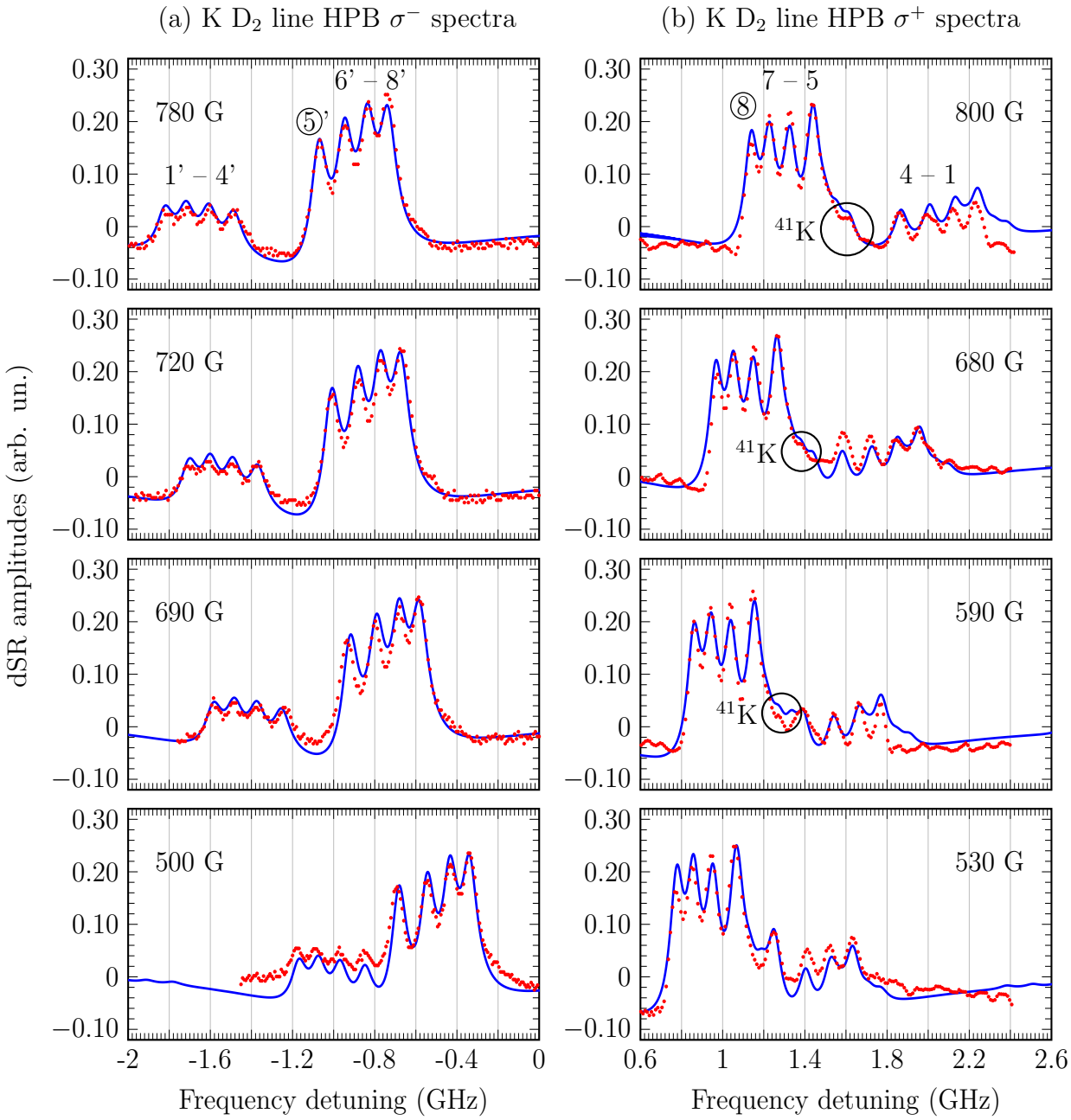

Figure 3.15: ^{39}K D_2 line recorded (red dots) and calculated (blue solid lines) spectra for (a) σ^- polarized light at $B = 500,\ 690,\ 720,\ 780$ G; and (b) σ^+-polarized laser radiation at $B = 530,\ 590,\ 680,\ 800$ G. Experimental parameters: transition linewidth ~ 100 MHz, NC thickness $\ell = 350$ nm, laser power $P_L = 0.1$ mW, reservoir temperature $\Theta_r = 150$ °C. In each case, all eight atomic transitions are well spectrally resolved. Although the abundance of ^{41}K in the cell is small (6.7%), a portion of its spectra can be seen; the peaks circled in the graphs are caused by the presence of ^{41}K isotope.

The complementary study with a σ^+ polarized excitation for the B-field values of 530, 590, 680 and 800 G is shown on the right panels of Fig. 3.15. The spectra are recorded for a reservoir temperature $\Theta_r \sim 150$ °C, a laser power $P_L \sim 0.1$ mW, and atomic transitions linewidth about 80 MHz FWHM.

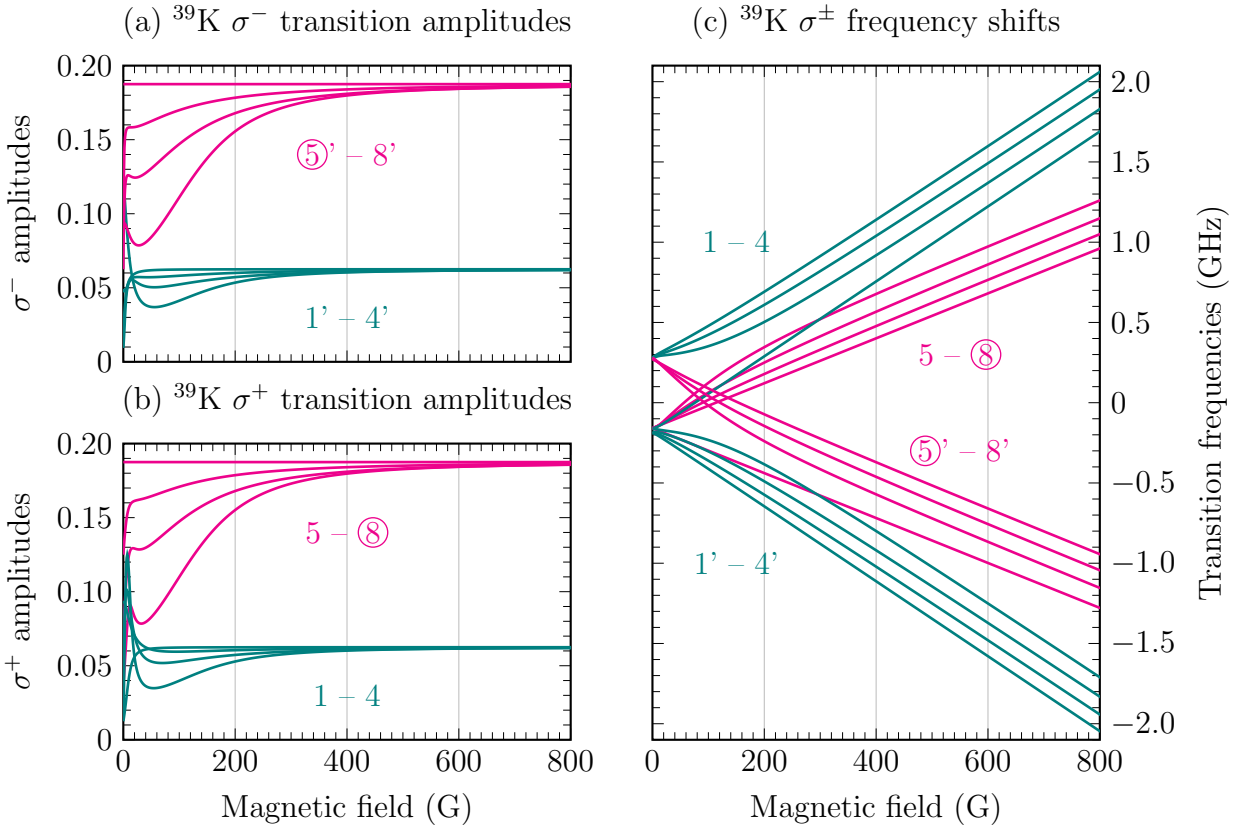

Figure 3.16: (a) Evolution of the probabilities of 1'–4' (dark green) and ⑤'–8' (magenta) transitions versus B-field for a σ^- polarized excitation. (b) Evolution of the probabilities of 1–4 (dark green) and 5–⑧ (magenta) transitions versus B-field for a σ^+ polarized excitation. For simplicity, only the transitions that remain in the spectrum for strong magnetic field are presented. (c) Evolution of transition frequencies as a function of the magnetic field for both circular polatizations.

As is seen from Fig. 3.15(a), there are two groups formed by transitions 1'–4' and ⑤'–8' and all these eight transitions, whose diagram (uncoupled basis) is shown in Fig. 3.14(a), are well seen. The same remark holds for transitions 1–⑧ from Fig. 3.15(b). Note that for a given group, the amplitudes of the transitions are equal to each other with the frequency intervals between them beeing nearly equidistant. These peculiarities as well as the strict number of atomic transitions which remain the same with increasing magnetic field are evidences of the establishment of Paschen-Back regime. Transitions labeled ⑤' and ⑧ are the so-called "guiding" transitions (GT) [66, 119]: their probability as well as their frequency shift slope remain invariable ($s^\pm = \pm 1.4$ MHz G^{-1}) in the whole range of applied B-fields.

A frequency reference was formed with a SA spectra (not shown) recorded for $B = 0$. As

was demonstrated in [120], the existence of crossover resonances makes the SA technique useless for a spectroscopic analysis for $B > 100$ G. The blue curves in Fig. 3.15 show the calculated dSR spectra of ^{39}K and ^{41}K isotopes with the linewidth of 80 MHz for σ^- (left panels) and σ^+ (right panels) polarized laser radiations, which were performed using the transition frequencies and amplitudes whose evolution as a function of the magnetic field is shown in Fig. 3.16. A very good agreement between the experiment and the theory can be seen. Although there is only 6.7% of ^{41}K isotope in natural K, a much better agreement with the experiment is realized when ^{41}K levels are also included into theoretical consideration; particularly the peaks circled in Fig. 3.15 are caused by the presence of ^{41}K isotope. A very good agreement between the experiment and the theory can be seen for both polarizations and all applied magnetic fields.

It is important to note that at a relatively small magnetic field about 400 G, the two groups are already well formed and separated which is, as previously mentioned, a consequence of the small value of $B_0(^{39}\mathrm{K}) = 165$ G. In order to detect similar well formed groups for ^{87}Rb atoms, one must apply a much stronger magnetic field of $B \sim 6$ kG since $B_0(^{87}\mathrm{Rb})/B_0(^{39}\mathrm{K}) \sim 15$ [3, 81]. It is also interesting to note that the total number of atomic transitions for both circularly-polarized laser excitations is 44 when $B \sim B_0(^{39}\mathrm{K}) \sim 150$ G, while for $B \gg B_0(^{39}\mathrm{K})$ only 16 transitions remain: this is the manifestation of the HPB regime.

Linear polarization analysis

To achieve a linear (π) polarization excitation of the K vapor, the experimental setup presented on Fig. 3.10 has been slightly modified: the B-field is directed along the laser electric field $\mathbf{E}$ ($\mathbf{B} \perp \mathbf{k}$), the $\lambda/4$ plate is removed and two permanent magnets are used to set the $\mathbf{B} \parallel \mathbf{E}$ configuration.

In Fig. 3.17(a), the red dotted curves represent dSR experimental spectra obtained for $B =$ 300, 380, 480, 680 G (bottom to top), with $\Theta_r \sim 150$ °C and a π polarised laser radiation having a power $P_L = 0.1$ mW. The blue solid lines show the theoretical calculations with the corresponding experimental parameters. As we see, there are eight well resolved transitions, labeled 1–8, having amplitudes that tend asymptotically to the same value, see Fig. 3.17(b). Note that, in this case, the transition linewidth is somewhat larger ($\sim$ 120 MHz) which is caused by inhomogeneities of the transverse magnetic field across the laser beam diameter of 1 mm.

The transitions $\boxed{2}$ and $\boxed{6}$ are $|1,0\rangle \rightarrow |1,0\rangle$ and $|2,0\rangle \rightarrow |2,0\rangle$ transitions (coupled basis). For zero magnetic field, the dipole matrix elements for these π transitions are zero, see e.g. [28]; in other words they are "forbidden": for these transitions neither resonant absorption nor resonant fluorescence is detectable. Their transition probabilities start from zero and undergo a significant enhancement with increasing magnetic field which is the reason why we call them MI^r (remain). They however differ from the MI transitions which appear thanks to the mixing induced by the B-field and verify the selection rule $\Delta F = \pm 2$, see section 3.3.2.
For strong magnetic fields such that $B \gg B_0$, the probabilities of MI transitions tend to zero, likewise we could name them MI^v (vanish), while transitions $\boxed{2}$ and $\boxed{6}$ asymptotically tend to their maximum with increasing B-field. We have confirmed this statement using a magnetic field of 500 G and MI transitions of the ^{39}K, $F_g = 1 \rightarrow F_e = 3$ with σ^+ excitation. While transitions $\boxed{2}$ and $\boxed{6}$ already have big amplitudes, see Fig. 3.17(b), the MI transitions are not detectable.

Note that for the confirmation of this statement one must apply a magnetic field of 5–6 kG on ^{87}Rb atoms.

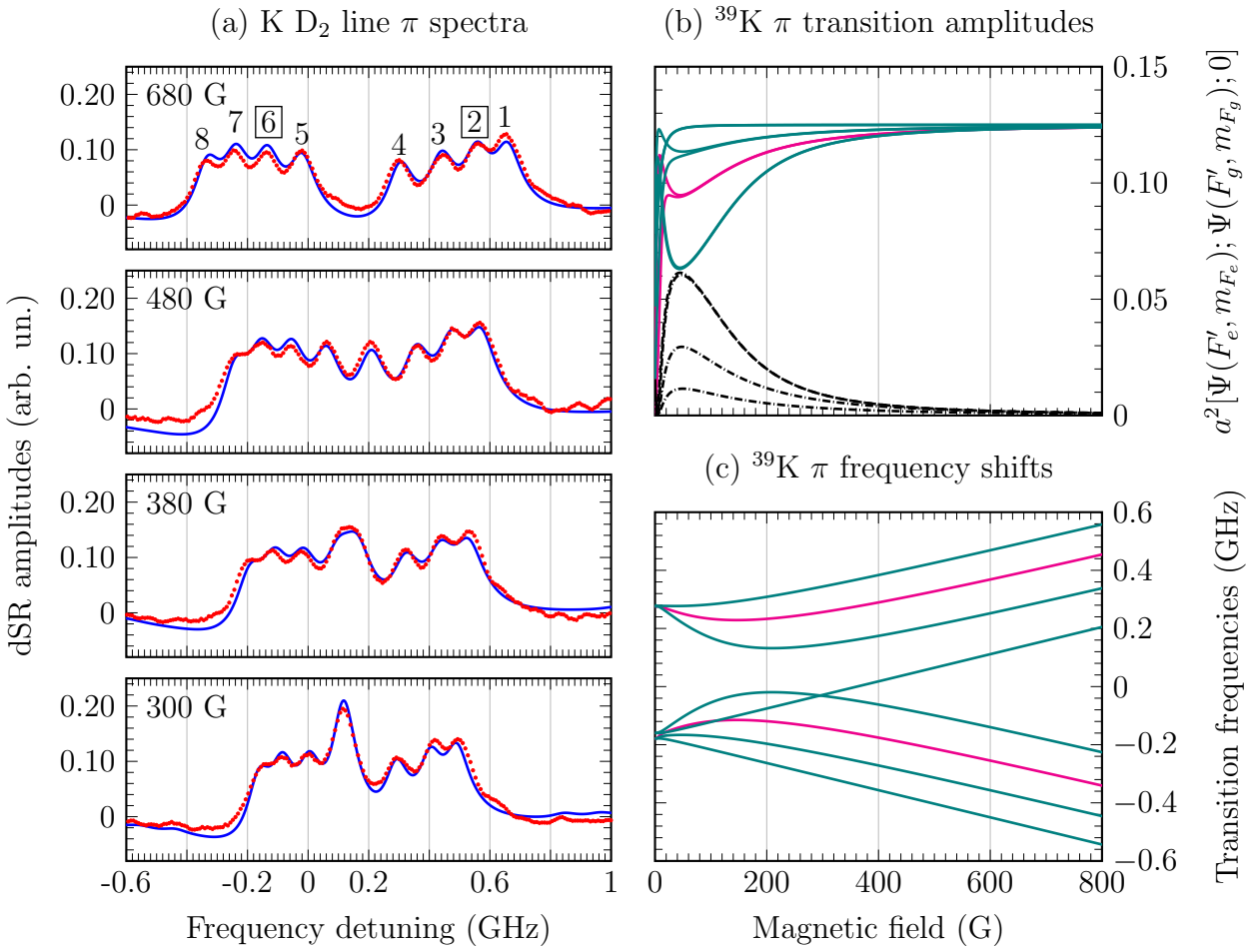

Figure 3.17: (a) K D$_2$ line, for π polarized radiation recorded and calculated for $B = 300$, 380, 480, 680 G. The red and blue traces show respectively the experimental and theoretical dSR spectra of ^{39}K and ^{41}K atoms, with a linewidth about 120 MHz, NC thickness $\ell = 350$ nm, $P_L = 0.1$ mW, and $\Theta_r \sim 150$ °C. (b) Evolution of π transition amplitudes as a function of the magnetic field; (c) Evolution of π transition frequencies as a function of the magnetic field. Curves associated with the transitions $\boxed{2}$ and $\boxed{6}$ are plotted in magenta, for the other transitions curves are plotted with a dark green color.

The peculiarities of the atomic transitions behavior of K in the HPB regime is different in the case of D$_1$ and D$_2$ lines: (*i*) as previously mentioned, there are two groups of eight transitions formed either by σ^+ and σ^- circularly-polarized light for the D$_2$ line and each of these group contains one GT. Meanwhile, in the case of D$_1$ line there are two groups of only four transitions, one for each circularly-polarized light, and the GT are absent; (*ii*) in the case of π polarized laser radiation, the spectrum of K D$_2$ is composed of eight atomic transitions, including two MI^r transitions, meanwhile the one of the D$_1$ line counts two GT and two MI^r transitions.

As mentioned earlier, a remarkable property of K atoms is that the HPB regime occurs at very small magnetic field as compared to widely used Rb and Cs atoms, and magneto-optical studies using the HPB regime can be realized with a much smaller magnetic field. Particularly, in [106], a complete HPB regime was achieved for ^{133}Cs D_2 line with a magnetic field $B = 27$ kG. Using an additional laser and optical pumping process of the ground-state sub-level, a high polarization of nuclear momentum was achieved. Similar results could be obtained with K atomic vapor for 10 times smaller magnetic field $B \sim 2.5$ kG, because $B_0(^{39}\text{K})/B_0(^{133}\text{Cs}) \sim 10$.

Let us note that the energy level structure for the isotope ^{41}K is very similar to that of ^{39}K, while the hyperfine splitting for the ground and excited levels are smaller [28, 121]. Particularly, the hyperfine splitting of the ground $4S_{1/2}$ level is 254 MHz, which is 1.8 times smaller than the one of ^{39}K (*i.e.* $B_0(^{41}\text{K}) \sim 90$ G). Consequently, the HPB regime is achieved at smaller magnetic field. In addition, the structure of ^{41}K spectrum in strong longitudinal magnetic field is the same as for ^{39}K: two groups of eight transitions are recorded for circularly-polarized excitation, each of these groups containing one GT. In the case of π polarized radiation, one can count eight transitions from which two are MI^r transitions. Transitions of ^{41}K follow the same behavior than the ones of ^{39}K, while equivalent probabilities are reached at a smaller magnetic field strength.

Summary

Starting from the time-independent Dirac equation applied to a single electron placed within an electromagnetic field, we derived a model describing the interaction between this electron and a homogeneous magnetic field. We have thus expressed energy levels, transition frequencies and dipole moment of alkali atoms as a function of the magnetic field and discussed the necessity of diagonalizing the Hamiltonian matrix except in rare cases.

Numerical simulations have shown particular behaviors of alkali D line transitions with respect to the magnetic field. Particularly, we have seen that the presence of magnetic field induces an asymmetric circular dichroism with respect to weighted center of $nS_{1/2} \rightarrow nP_{3/2}$ lines frequency for intermediate values of B around B_0, while the symmetry is recovered when the HPB regime is established. In addition, we have shown that some transitions experience a dipole moment cancelation for a precise value of B, different for each of these transitions, which contributes to the asymmetry of the MCD. We have stated a quantum interference effect occurrence to explain the dipole moment cancelations.

We have later performed experiments on Rb and K vapor and demonstrated a particular behavior of Rb D_2 line transitions in an intermediate range of magnetic fields validating our numerical results. Note that a similar behavior was observed in Cs D_2 line transmission spectra recorded with a half-wavelength-thick NC, see [122]. Besides, the coincidence between experiments and theory lead us to conclude on the validity of the hypothesis of B-field uniformity within the cell. The last experimental study concerned the investigation of the HPB regime of K D_2 line, where we made a complete polarization analysis of the spectra recorded by the dSR technique. We have verified that in the case of K vapors, the HPB regime occurs at relatively small magnetic fields as compared with other alkalis. Finally, it seems possible to use the spectrum of alkali atoms recorded by dSR from a NC to extract the value of the magnetic field interacting with the vapor.

Chapter 4

Sensing Applications

Contents

Introduction

Atomic spectroscopy of thermal alkali metal vapors exposed to magnetic fields underlying the optical magnetometry has been intensively studied and explored in the past decades (for the reviews, see [9, 27, 123]). Modern state-of-the-art magnetometers allow to achieve a remarkable sensitivity [124], and are mostly focused on the measurement of extremely low fields in shielded environment. They are successively used for measurements of biomagnetic fields [125, 126], revealing hidden ferromagnetic objects [127], etc. But besides, there are many other applications such as measurement and mapping of high gradient magnetic field in nuclear magnetic tomography, remote monitoring of nuclear reactors, alignment of particle accelerators, etc., where high spatial resolution, immunity against external perturbations, large dynamic range of measurement, and robust, autonomous, unshielded operation are of key priority, rather than unprecedented sensitivity attained by implementing sophisticated and expensive measurement schemes.

While Hall gauges are the most employed sensors to perform magnetometry of fields ranging from tens to thousands of Gauss, they are not suitable for performing remote sensing and measurement in strongly perturbed radiation environment such as in nuclear reactors [128]. This task can be done using optical magnetometers, which are immune against electric perturbations and thermal drift.

The results from chapter 3 suggest the possibility to use the alkali spectra recorded from a NC in order to extract the value of magnetic field to which the vapor is exposed. Particularly, we have presented a theoretical model which combines the interaction of atomic vapors confined in NC with an incident laser light (chapter 2) with the behavior of alkali D lines in magnetic field (chapter 3). We have also shown that this model predicts with a great accuracy the evolution of alkali spectra exposed to a magnetic field. Furthermore, our experimental study has also demonstrated the immunity of recorded spectra against inhomogeneities of the produced magnetic field thanks to a sub-μm thickness of the vapor column, where the interaction takes place.

In this chapter, we depict a scheme performing optical magnetometry based on nanocell spectroscopy of alkali vapors exposed to the magnetic field to be measured. We first propose a concept and based on the results obtained in chapters 2 and 3, we discuss the most suitable operation parameters and limiting factors. At last, we provide a proof of feasibility and make a performance analysis of the magnetometer, addressing precision, response time, and performance limitations.

4.1 Outline of a NC-based magnetometer

In this section, we propose a scheme performing optical magnetometry based on consecutive fittings of experimental data recorded by dSR from a NC. With the help of the results obtained in the previous chapters, we discuss suitable operation parameters for the scheme to be efficient, such as optimal cell thickness or laser polarization.

4.1.1 Proposition

The results presented in chapter 3 show that dSR spectra experience large changes versus magnetic field, thus we propose to use the spectral profile of dSR from alkali vapors contained in NC as a measuring quantity to determine the value of applied magnetic field. Figure 4.1 presents a possible operation principle scheme of this NC-based optical magnetometer. The evolution transition frequencies and amplitudes calculated with the model of section 3.1 can be pre-calculated and used as data to successively calculate theoretical dSR spectra and find the one that fits the most the experimentally recorded spectrum using the model presented in section 2.1 (see also section 3.2.1).

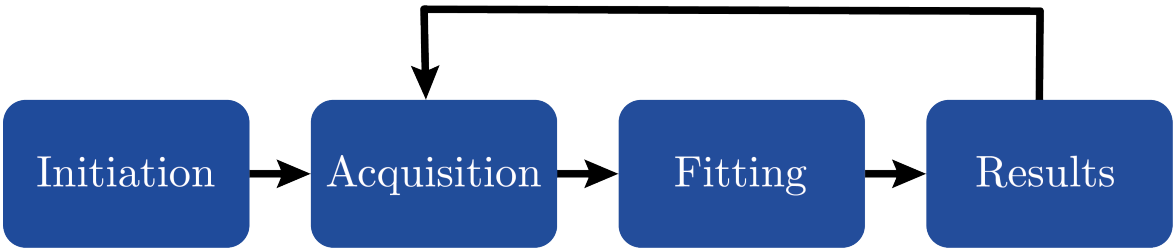

Figure 4.1: Operating principle of the magnetometer. During the initiation step, transition frequencies and amplitudes are loaded as data. The software driving the magnetometer then commands the acquisition of an experimental SR spectrum from the NC, where an unknown longitudinal magnetic field is applied. This spectrum is saved and fitted using the developed model, which returns the value of the magnetic field interacting with the vapor.

After this initiation step, the driving software proceed to the acquisition of an experimental spectrum from a NC placed in the B-field to measure. The derivation of the SR spectrum can be achieved after recording, by numerical differentiation or directly in the course of measurement using lock-in detection. At this step, signal processing can also be applied to the experimental spectrum to make it smoother or to filter the signal from a noisy component.

The fitting procedure can be straightforward by calculations of the residuals between experiments and theory for a given magnetic field value and all or part of the frequencies scanned by the laser, returning the B-field value for which the residuals are the smallest, *i.e.* corresponding to the theoretical spectrum fitting the best the experimental one. After yielding results, the procedure may be repeated, starting off from the acquisition step, to perform continuous measurement of the magnetic field.

4.1.2 Suitable operation parameters

Atomic line

At the Institute for Physical Research of Ashtarak, nanocells filled with K, Rb and Cs are available. The first question that we should answer is what atomic vapor and what line are the most suitable to perform magnetometry.

In the previous chapter, we have focused our studies on the first two alkalis, and we have shown that the HPB occurs for B-fields much greater than $A_{hfs}/\hbar$. We have thus been able to observe that the Paschen-Back regime occurs for much smaller magnetic fields in the case of K vapors (see section 3.3.3) than for Rb vapors (see section 3.3.2). As noted in section 3.3.3, HPB spectra consist of groups of transitions with the same amplitudes and the same frequency spacings with respect to each other. It is worth to note that in this regime, the B-field-induced frequency shift slope is the same among each group of transitions. Hence, only absolute measurements of the transition frequencies can be used to extract the magnetic field value, since each group of transitions has a constant amplitude with further increase of magnetic field. Thus, the sensitivity of the magnetometer drops in the HPB regime, especially if a precise frequency reference cannot be provided. In this regime, extraction of the B-field value from the characteristically symmetric absorption spectra is a more convenient method [129].

With a naturally present isotope having a B_0 value more than twice bigger than that for the main isotope, Rb vapors seem more suitable to be used as the atomic sensors for magnetic field as the isotopes will switch regime of interaction at different B-field values. This particularity is not the case for Cs vapors whose only natural isotope is ^{133}Cs. In addition, in section 3.3.2 we have shown a very particular behavior of some of the transition of Rb D_2 line and seen a good agreement with our theoretical model. The evolution of the transitions beeing more sophisticated than that for the D_1 line should allow a better sensitivity. Hence, Rb D_2 line seems to be the better atomic line to perform magnetometry.

Cell thickness

In figure 2.4(c), we have shown the evolution of the lineshape of dSR spectra when the cell thickness varies from $\ell = \lambda/8$ to $5\lambda/4$. Oscillations in the lineshape with a periodicity of $\lambda/2$ were observed, while vanishing of the signal occurred for $\ell = (2m+1)\lambda/2$. In section 3.3.1 we have discussed the importance to combine spatial resolution (increased by decreasing ℓ) and spectral resolution (increased by increasing ℓ). Besides, and even thought we have not stated it yet, NC with tapered gap is very sensible to vibrations which drive the beam around the incidence spot across scanning of the laser frequency. Hence, vibrations may cause non negligible random distortion of the profile. In order to verify which range of thicknesses are less influenced by vibrations, we have plotted on Fig. 4.2 the absolute value of the derivative of dSR profile with respect to ℓ for a unique transition. One can observe several regions where a minimal variation ($< 5 \cdot \lambda^{-1}$) for the center of line is achieved: around $\ell = 0.4$, 0.6, 0.9 and 1.1λ. Besides, the non-symmetric profile of the dSR causes the mininum of variation to not be achieved for the same thickness for both wings, say e.g. around 0.5λ for the lower frequency wing of the spectrum (that is $\Delta/\gamma < -1$) as compared with the higher frequency wing which is achieved at about 0.3λ ($\Delta/\gamma > 1$). Let us recall that most of the information is contained within a spectral range $\Delta/\gamma \sim \pm 3$, see Fig. 2.4(c).

From these results, the thicknesses $\ell \sim 0.4\lambda$ and $\ell \sim 0.6\lambda$ appear as the most convenient ones to perform magnetic field measurements using the dSR profile of alkali vapors contained in NC. The choice in between the two will be motivated by the following experimental considerations: it will be better to shine the part of the NC which has the most homogeneous region of thickness (only if using a NC with tapered gap). In addition, one should pay attention that dSR signals can

be either positive ($\ell < \lambda/2$) or negative ($\lambda/2 < \ell < \lambda$) which, depending on the response of photodetector, may not meet the requirements of most simple Analog-to-Digital converters (A/D) without applying offset voltage. Noteworthy, due to strong dependency on cell thickness, the profile of dSR can be used to perform measurements of cell thicknesses for which the sensitivity follows that presented in Fig. 4.2.

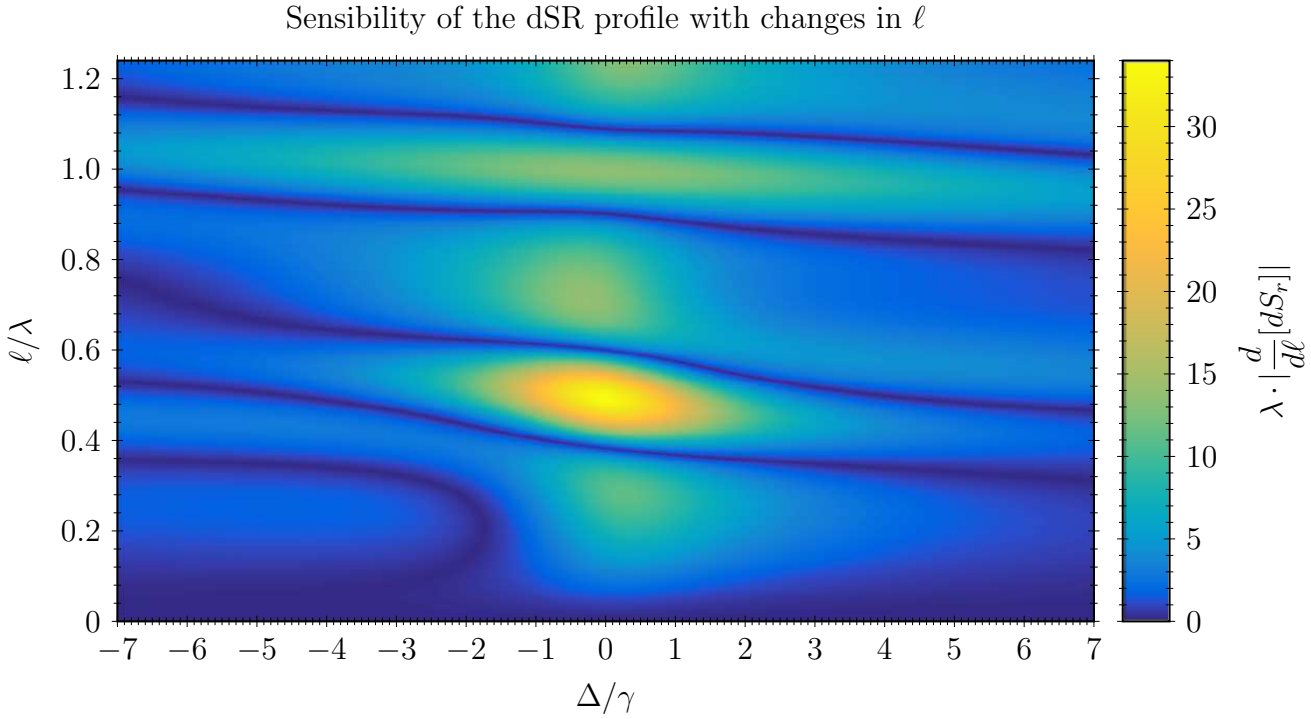

Figure 4.2: Absolute sensitivity of the dSR profile with respect to the cell thickness as a function of the frequency detuning of the transition (normalized over the homogeneous linewidth, x-axis) and the cell thickness (normalized over the laser wavelength, y-axis). The bright yellow color marks regions of maximum sensitivity while the dark blue color marks the ones with minimum sensitivity. For readability, the color scale is slightly non-linear.

Laser polarization

Making use of the results obtained in the previous chapters, we have calculated the evolution of the natural (72% of ^{85}Rb, 28% of ^{87}Rb) Rb D_2 line dSR spectrum sensitivity to B-field changes as a function of the laser frequency and the magnetic field. The results are presented in Fig. 4.3(a) for σ^- polarization, Fig. 4.3(b) for π polarization and Fig. 4.3(c) for σ^+ polarization; where the magnetic field varies from 0 to 2.8 kG. The frequency span of calculations has been set to 8 GHz in order to coincide with typical mode-hop free tuning range of ECDL.

We can see completely distinct spectral behavior depending on the laser polarization: with the increase of magnetic field, the transitions slowly shift toward higher (respectively lower) frequencies for left-circularly polarized light (respectively right-circularly polarized), while the transitions mostly remain in the same frequency window for linearly-polarized light.

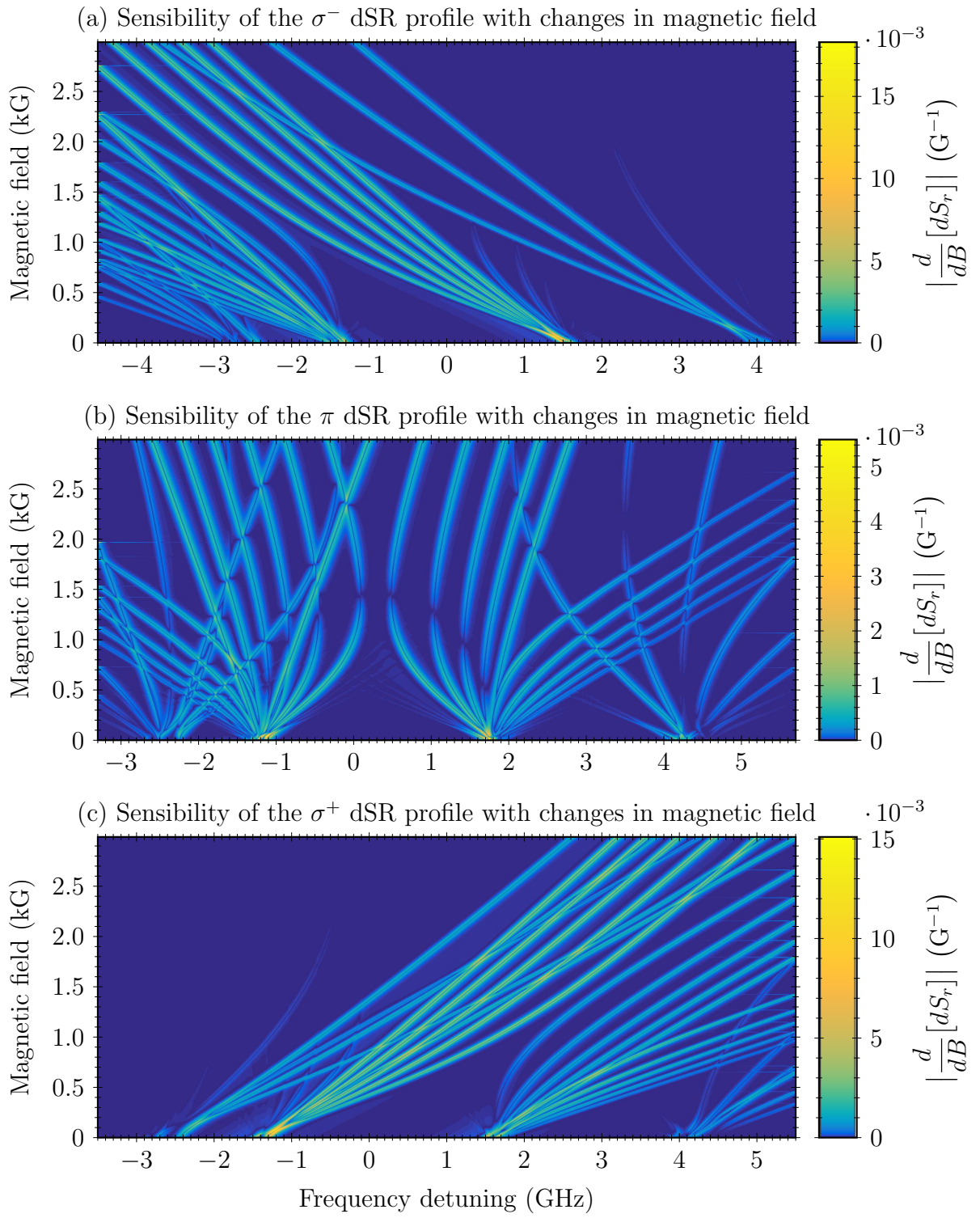

Figure 4.3: Absolute sensitivity of the Rb D_2 line dSR profile with respect to the magnetic field as a function of the laser frequency (x-axis) and the magnetic field (y-axis) in the case of (a) σ^-, (b) π and (c) σ^+ polarizations. The bright yellow color marks regions of maximum sensitivity while the dark blue color marks the ones with minimum sensitivity. For readability, the color scale is non-linear.

Although π polarization seems to be more convenient for the measurements as the transitions remain in the same frequency window with increasing B-field, the average sensibility is lower than that for $\sigma^{\pm}$ (about 3 times less). Note also that the π excitation requires to have a $\mathbf{B} \perp \mathbf{k}$ configuration to preserve the advantage of the NC (propagation trough the nanometer-thick slab); which in this case means that the magnetic field is applied along the cm-long sides of the cell (*i.e.* either along the x-axis or y-axis, see e.g. Fig. 2.1). As a consequence the technique will be much more affected by possible gradient of B-field across the beam, impacting the spatial resolution of the magnetometer. Hence, circularly-polarized excitation is preferable to perform scalar magnetometry from NC. Besides, linearly polarized light in the $\mathbf{B} \parallel \mathbf{k}$ configuration will give rise to simultaneous $\sigma^{\pm}$ excitations, which can also be interesting, but will require twice more calculations.

4.2 Proof of feasibility

In this section, we present the proof of concept for an optical magnetometer based on spectroscopy of Rb vapor contained in a NC. A performance analysis of the developed laboratory prototype magnetometer is presented, realized by exposing the NC to the inhomogeneous magnetic field produced by a permanent neodymium-iron-boron alloy ring magnet at different distances. In Section 4.2.1, we present the optical and electronic scheme of the magnetometer, as well as the measurement procedure and corresponding algorithms. Performance analysis of the magnetometer is presented in Section 4.2.2, addressing precision, response time, and performance limitations.

4.2.1 Measurement technique

The employed measurement technique combines optical, electronic and programming components. Here we give a step by step description of the experimental assembly, methodology, and measurement algorithms. It is worth noting that the proposed system can only measure magnetic field component directed along the laser beam.

Experimental arrangement

Optical elements. The measurement of magnetic fields was carried out on the setup presented in Fig. 4.4. An externally controlled extended cavity diode laser emits a linearly-polarized light ($\lambda_L = 780$ nm, $\Delta\omega_L \simeq 2\pi \times 1$ MHz) tuned to the Rb D_2 line. A fraction of the light was sent to an auxiliary branch to form a saturated absorption frequency reference, recorded with a photodetector (SA) equipped with a cylindrical guiding pipe to prevent contribution from residual ambient light to the detected signal. The polarization of the light in the main branch was purified by a polarizer (P) and then converted to a left-hand circularly-polarized light using a quarter-wave-plate ($\lambda/4$) in order to excite σ^+ transitions in the Rb vapor. The beam was directed at normal incidence onto the NC. The arising selective reflection beam was carefully separated from other backward beams and sent to the second photodetector (SR) using a mirror.

In order to reach sufficient atomic density of $2.0{\times}10^{13}$ cm^{-3}, the sidearm of the cell was heated to 125 °C using a 3 cm-thick oven, while keeping the temperature of the cell windows at

least 25 °C higher to prevent condensation of vapor on the sapphire windows. A set of filters was used to adjust the power of the laser light to ∼ 1 mW for the SA branch, and ∼ 100 µW for the beam directed onto the NC. Pinholes were used to keep the incident beam diameter small enough (∼ 1 mm) for covering a uniform thickness area of the cell.

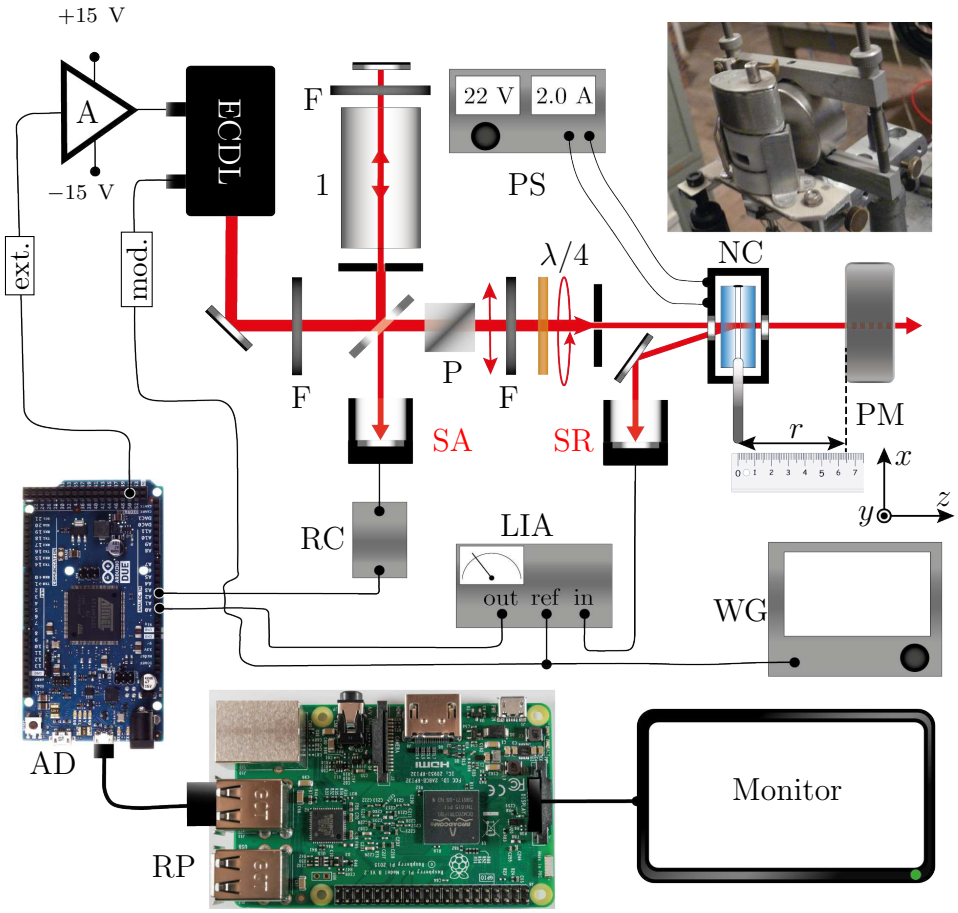

Figure 4.4: Experimental arrangement of the magnetometer. ECDL – extended cavity diode laser; F – filters; 1 – reference Rb cell; P – polarizer; $\lambda/4$ – quarter-wave-plate; PS – DC power supply; NC – nanocell + oven assembly; PM – ring magnet; WG – waveform generator; LIA – lock-in amplifier; RC – RC circuit; A – amplification circuit; AD – Arduino Due board; RP – Raspberry Pi computer; SA and SR – photodetectors recording saturated absorption and selective reflection signals. Upper-right inset: photograph of the nanocell in the oven and the magnet.

A neodymium-iron-boron alloy ring magnet (PM) with an axis aligned along the laser beam was placed at the rear side of the NC-oven assembly to apply a longitudinal magnetic field. The magnet was mounted on a translation stage, and the magnet–NC distance r was measured using a simple ruler. The strength of the magnetic field applied to the vapor column was changed by a simple longitudinal translation of the magnet. We have carefully checked that the beam was completely transmitted through the center of a 6 mm-diameter hole of the ring magnet for all the positions of the magnet, which enables to minimize the residual transverse magnetic field

components.

Electronics. The linear scanning of the laser radiation frequency across the Rb D_2 line was controlled by an Arduino Due board (AD), which outputs a 0 to +3.3 V voltage with a 12 bit resolution (0.80 mV steps), followed by a self-made amplification circuit (A), which was used for signal conditioning to extend the voltage range to −7 to +7 V needed for the external ramping control of ECDL. In addition to scanning, the laser frequency was also modulated by a 5 kHz sine wave of 300 mV amplitude generated by a Siglent SDG 5082 waveform generator (WG). This modulation signal served as a reference for the SRS SR510 lock-in amplifier (LIA), which picked the signal from the SR photodetector and directly generated the dSR signal on the output. The time constant of the LIA was set to the minimum to prevent broadening distortion of the dSR spectrum.

Both the SA and SR signals were processed by an analog-to-digital converter of the AD board, and sent to the Raspberry Pi (RP) computer via USB port. The output voltage of the SA photodetector was kept between 0 and +3.3 V to meet the AD range. This was done by the use of an RC circuit serving simultaneously for attenuation of the output voltage of the SA photodetector, and for filtering the high-frequency components arising because of the sine modulation of the laser frequency. The output voltage of the lock-in amplifier was also carefully adjusted to fit 0 to +3.3 V range, which was realized by applying offset voltage (dSR signal can be slightly negative) and choosing an appropriate sensitivity level.

Measurement procedure

The procedure of measurement can be summarized by the following actions: initiation, acquisition, and fitting. The interaction between the user and the magnetometer relies on a Mathematica-based program processed on the RP computer and displayed on a monitor. A summary of the main program is shown in figure 4.5. This simple program is based on four different functional blocks that we have developed in Mathematica, and which we detail here-after.

```
PROGRAM Magnetometer.nb

dataIni = initiation();
recordedSpectrum = getSpectrum();
rescaledSpectrum = rescaleFrequency(recordedSpectrum);
magneticFieldValue = fitMagneticField(dataIni,rescaledSpectrum);
return magneticFieldValue
```

Figure 4.5: Outline of the Mathematica algorithm performing the measurement. A brief description of each functional block is given in the text.

`Initiation()`. The initiation function can be summarized as follows. First, four data files containing the transition frequency shifts and transition amplitudes versus magnetic field (two for ^{85}Rb, and two for ^{87}Rb) are imported. We have limited the magnetic field span to a realistic range of 0.1 – 2 kG conditioned by particular magnet, oven, and translation stage used in our

experiment. The step of magnetic field variation is set to 5 G, such that the number of lines per file (590) does not overload the RAM of the RP computer. Furthermore, an additional file is being loaded to interpolate the lineshape of the dSR signal versus the laser frequency, see `fitMagneticField()` function for more details.

`getSpectrum()`. Upon the user demand, the RP computer commands a single-shot scanning of the laser frequency across the Rb D_2 line to AD, which is executed by generating a sweep voltage. For each value of the generated sweep voltage, AD reads the analog input signal to save the output voltage from the SA photodetector and the dSR signal from the LIA.

After each step of voltage sweeping generated by the AD digital-to-analog converter, the AD makes a 60 ms pause before reading the SA and dSR signals in order to let the atom-light interaction regime to be established. This procedure ensures obtaining as narrow spectra as possible, taking into account that a too long interaction time leads to optical pumping, which is not accounted in the fitting procedure. At the end of the sweep, the saved values are retrieved by the RP.

`rescaleFrequency()`. The re-scaling step is necessary in order to get a common x-axis for the experimental and the theoretical spectra (as the variable is voltage for the first case, and frequency in the second). For that the program requests data from the SA channel: using the FindPeaks routine of Mathematica, the program identifies the strongest crossover resonances of the group of transitions ^{85}Rb $F_g = 3 \rightarrow F_e = 2, 3, 4$ and ^{85}Rb $F_g = 2 \rightarrow F_e = 1, 2, 3$.

The zeroing of the frequency axis is also needed in order to fit correctly the experimental signal, and for that we thus choose the strongest crossover resonance of ^{85}Rb $F_g = 2 \rightarrow F_e = 1, 2, 3$, located at $\omega = 2\pi \times 384.232125082$ THz from the ground state 5 $^2S_{1/2}$, as the zero detuning.

`fitMagneticField()`. The fitting procedure relies on the theoretical analysis presented in [49], where a modeling of the optical interaction of the laser with Rb atoms in a NC in the presence of magnetic field was presented. As one can see from Eq. (19) in [49], the accounting of the atomic velocity distribution in the NC for calculating SR spectrum can be extremely time consuming, as it is not possible to get analytic solutions. However, assuming that all the transitions in the spectrum have the same lineshape (which in the case of a NC is neither Loretzian/Gaussian nor Voigt), the selective reflection signal (Eq. (14) in [49]) can be re-written as

$$S_r(\omega, B) = \sum_j d_j(B) \times S(\omega - \omega_j(B)), \tag{4.1}$$

likewise the dSR signal can simply be expressed as

$$dS_r(\omega, B) \equiv \frac{d}{d\omega} S_r(\omega, B) = \sum_j d_j(B) \times \frac{\partial}{\partial\omega} S(\omega - \omega_j(B)), \tag{4.2}$$

where $d_j(B)$ and $\omega_j(B)$ are part of the data obtained with the initiation function. The summation on j is done for each transition present in the frequency window returned by `rescaleFrequency`. The lineshape $S(\omega, \ell, \Gamma)$ of each individual transitions was pre-calculated using successively Eqs. (19), (18) and (14) from [49], setting $d_{eg} = 1$ and $\Delta = 0$, while the cell thickness $\ell = 490 \pm 10$ nm and the linewidth $\Gamma = 50 \pm 5$ MHz were fit to that of a recorded experimental Rb D_2 spectrum (without magnetic field). These simplifications lead to a large enhancement of the calculations speed and, in this way, we estimate the calculation time to be reduced by a factor 100.

Using the acquired dSR spectrum with a re-scaled x-axis and the data from the initiation, the program recursively calculates theoretical spectra (natural Rb: 72% of ^{85}Rb; 28% of ^{87}Rb) in the given frequency window, by changing the magnetic field with a step of 5 G. For every calculated spectrum, the program looks for a qualitative agreement between experiment and theory by making differences of the signals for all scanned frequencies, and calculates their average. The returned magnetic field value by the routine is the one having the smallest averaged residuals. To get a slightly better precision than 5 G on the returned value, we made use of the interpolation function of Mathematica on the B-field dependence of the averaged residuals.

4.2.2 Performance analysis

The following methodology was implemented in order to test the magnetometer and evaluate its performance. The distance r between the ring magnet and the NC was varied from 20 mm to 80 mm with a 3 mm step using translation stage, preserving co-axial alignment of the magnet in respect to the laser beam. The distance was monitored with a 1 mm graduated ruler ($\Delta r \simeq$ 4 mm). For each value of r, the measurement procedure described in the previous section was employed, returning the measured B value. The results of these measurements showing the response of our setup to the longitudinal magnetic field are presented in Fig. 4.6.

The examples of spectra recorded and processed during the measurement procedure are presented in the insets (i), (ii) of the figure, corresponding to $r = 35$ and 20 mm, respectively. The traces of red dots represent experimentally recorded spectra, and the best fitting simulations are shown by blue lines. Based on such fitting runs performed for 17 values of r, we have built a B-field calibration curve, see Fig. 4.6(a). Red dots on this graph indicate the B-field averaged over 20 values obtained by our measurement procedure, the green triangles correspond to a calibration curve obtained with a "Teslameter HT201" magnetometer, and the solid line is the calculated dependence following [130]

$$B(r) = \frac{B_{res}}{2}\left[\frac{r}{\sqrt{r^2+R_{out}^2}} - \frac{r-h}{\sqrt{r^2-h^2+R_{out}^2}} - \frac{r}{\sqrt{r^2+R_{in}^2}} + \frac{r-h}{\sqrt{r^2-h^2+R_{in}^2}}\right], \tag{4.3}$$

where $R_{in} = 3$ mm and $R_{out} = 25$ mm are the inner and outer radius respectively, $h = 30$ mm is the height and the producer-specified residual induction B_{res} at the magnet surface of 1.45 T. An obvious consistency of the measured magnetic field with the calibration curve of the magnet justify applicability of the proposed concept.

Precision

To estimate the precision and repeatability of the measurement technique, we have calculated the standard deviation σ and the coefficient of variation $C_v = \sigma/\mu$ where μ is the mean of B, determined for each positions of the magnet from the results of twenty consecutively recorded and fitted spectra, see Fig. 4.6(b). For measured B-fields over 0.4 kG, we get $C_v < 5\%$, which is a good value for a non-optimized table-top laboratory setup. Higher precision is expected for stronger magnetic field, as the establishment of a hyperfine Paschen-Back regime leads to equalization of the amplitudes of individual transitions and increases their frequency shift [48].

As expected, the deviation increases with the decrease of the magnetic field, caused by transition overlapping. But even in this case, the relative deviation still remains below 10%.

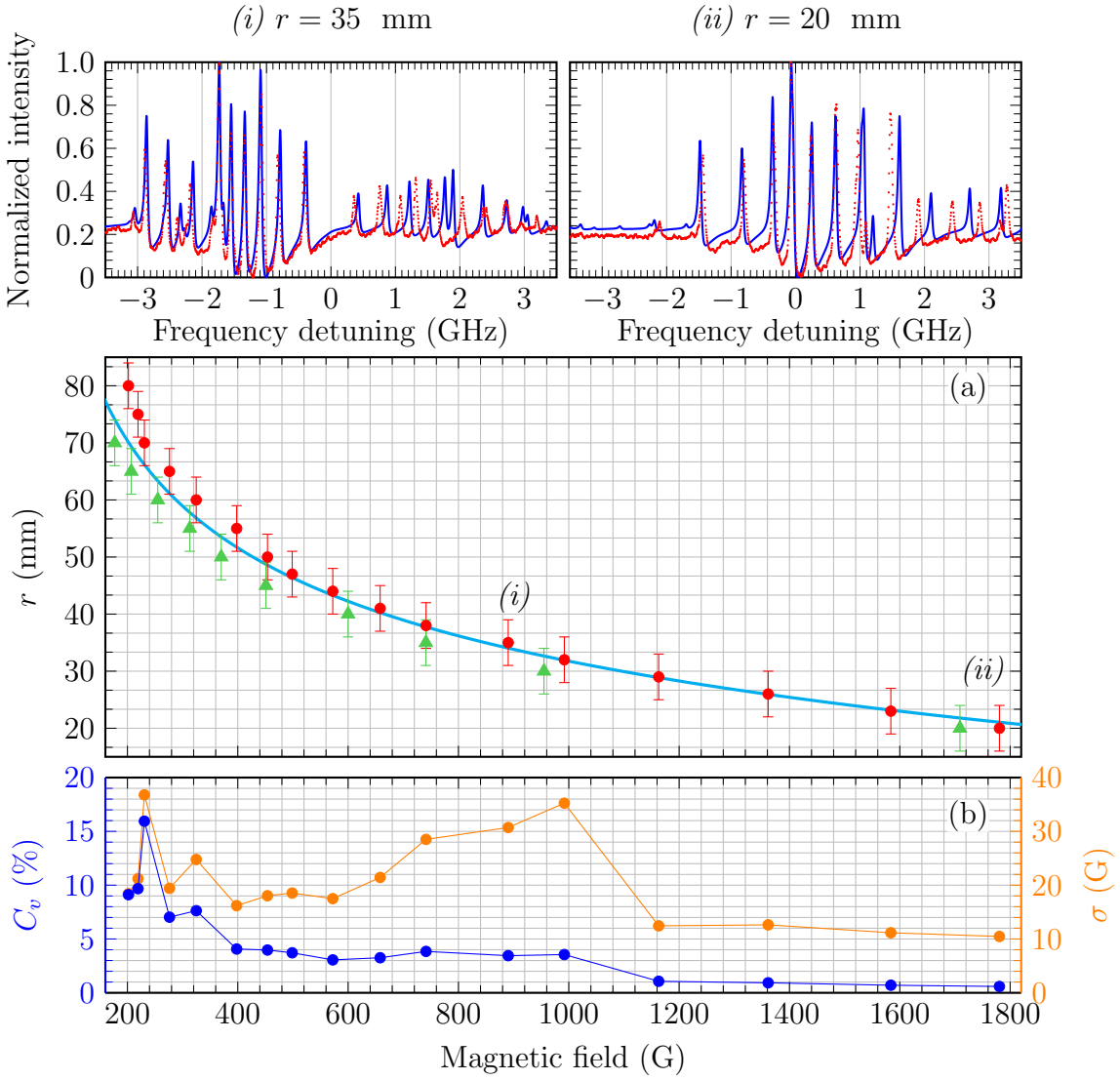

Figure 4.6: (a) Measured magnetic field (x axis) as a function of the cell-magnet distance r (y axis) averaged over 20 measurements. Red dots: experimentally measured with NC; green triangles: measured with a Hall gauge; solid line: calculated. (b) Evolution of the standard deviation σ (orange line, right y-axis), and the coefficient of variation C_v (blue line, left y-axis) as a function of the measured magnetic field. The insets (i, ii) show two obtained spectra (red dots) and their respective fits (blue solid lines) recorded for $r = 35$, 20 mm and corresponding to the measured value of $B = 0.895$ and 1.79 kG, respectively. Both the experimental and theoretical spectra are plotted with an increment $n = 2$, see the text.

Response time

Another important characteristic of the magnetometer is its temporal resolution. In the case of the proposed measurement technique, the overall response time is the time needed to return the measurement result. After measuring the response time of each routine, it appeared that the recording and rescaling are taking about 30 s, while the fitting routine itself lasts tens of minutes.

To accelerate the temporal response of the magnetometer, we have checked the behavior of the fitting routine when increasing the increment n for the laser frequency sampling. For $n = 1$, the measurement readout is taken from all the 4096 frequency points separated by ≈ 2.2 MHz. For $n = 2$, the readout is taken at every second point (2048 points in total), etc. Increasing the increment allows to reduce the overall number of operations, thus reducing the response time in a close to linear way for small values of n: $\tau(n) \approx \tau(n = 1)/n$. For $n = 1$, the measured response time was about 20 minutes. The measurement process can be accelerated by increasing the sampling interval. But the increase of the n value eventually leads to distortion of the recorded spectral lineshape, thus reducing the overall measurement precision. Our studies have shown that no difference in returned results (recorded spectra) is observed for $n \leqslant 18$ in the explored range of magnetic field; non-negligible differences appear for $n > 20$. At the same time, the above mentioned initial nearly-linear reduction of measurement time with the increase of sampling interval saturates for $n \geqslant 10$ on the level of $\tau \lesssim 2$ minutes.

Limitations

Precision and sensitivity of the proposed magnetometer are limited by random and systematic errors. The main sources of random errors are: *(i)* electrical noises in measurement circuits; *(ii)* mechanical vibrations; *(iii)* thermal convection of air in the vicinity of NC windows. Among the most impacting sources of systematic errors are: *(i)* non-linearity in laser frequency scanning; *(ii)* non-perfect circular polarization of the input laser radiation; *(iii)* non-uniformity of the NC thickness across the incident laser beam; *(iv)* imperfect normal incidence angle and/or large divergence of the laser beam. Less contribution is expected from variation of the NC temperature. Nevertheless, we should note that most of these errors can be strongly reduced in a final design of a magnetometer device.

As most table-top systems, our magnetometer suffers from the environmental perturbances. Shielded wiring, integration of electronics in a chip device and connection matching can strongly suppress electric noise. The impact of mechanical (acoustical) vibrations causing laser beam walk across the tapered gap of the NC, resulting in change of the cell thickness during the scanning and impacting the signal lineshape, can be strongly reduced in the case of a compact design and low-height rigid mounting of optical components. Moreover, this impact can be reduced using a NC with a large homogeneous thickness, or a NC with pressure-controlled thickness [131].

Similarly, solutions can be found to overcome influence of systematic effects. Non-linearity of the laser frequency scanning, which is obviously seen in the upper insets of Fig. 4.6, is caused by imperfect grating control of the ECDL and can be avoided with the use of a free-running laser diode, which will also be a cost-effective solution. However, in this case the measurement precision can be lowered for small magnetic fields due to the $10 - 20$ MHz linewidth of such lasers. Alternatively, a Fabry-Pérot etalon could be used to perform the frequency re-scaling. Proper

polarization control can be easily reached by using commercially available good-quality polarizer and quarter-wave plate. As to the non-uniformity of the cell thickness in the region of laser beam and improper incidence angle or beam divergence, these problems will be mostly solved when implementing a proper design of the compact device, as was mentioned above. Although rising the NC side arm temperature over 130 °C could improve the signal-to-noise ratio, it also leads to additional spectral broadening of the atomic lines, which mostly impacts the lower B-field measurement limit ($B < 0.3$ kG), when most of individual lines overlap. Finally, the possible light intensity fluctuations can also be suppressed in a cheap way by implementing a feedback control, as is shown in [132].

Summary

To summarize, we have proposed a robust method to perform scalar optical magnetometry using alkali spectra recorded by dSR from a NC. We have discussed suitable operation parameters, and likewise propose to use a NC filled with natural Rb as the magnetic field sensor. The incident laser polarization influences the sensitivity of the measurement: it is preferable to use a circular polarization rather than a linear one. To minimize the influence of acoustic vibrations, it is better to shine either the region $\ell \sim 0.4\lambda = 312$ nm or the region $\ell \sim 0.6\lambda = 468$ nm in the case of Rb D_2 line ($\lambda = 780$ nm).

In order to make a proof of principle, we have built a user-friendly magnetometer that we have tested by applying an inhomogeneous magnetic field with the help of a permanent ring magnet, showing that NCs filled with Rb are a good tool to perform scalar magnetometry. Indeed, the performance analysis yielded a coefficient of variation less than 5% in the range 0.4 – 2.0 kG which should be unchanged for magnetic fields of several kG. To make a comparison, the proof-of-concept of an optical magnetometer based on the non-linear Hanle effect taking place in a cm-long Rb vapor cell was recently reported in [133], where the estimated precision was about ±5 mG in the range ±1.5 G.

Adjusting the increment of the frequency axis sampling, we have effectively reduced the response time to the order of the minute. We have also made an analysis of the limiting factors including random errors, for which the main sources are electrical noises, acoustic vibrations and thermal convection; and systematic errors: non-linearity of the laser scanning, impurity of circular polarization, non-uniformity of the cell thickness across the laser beam and non-perfect normal incidence of the beam onto the cell. We have proposed few solutions to limit the influences of these random and systematic errors.

Conclusion & Outlook

To summarize, we have presented a theoretical model describing the interaction of near resonant laser light with alkali vapors confined in NC in the presence of an external static magnetic field. Experimental verifications of the model have shown excellent agreement between recorded and calculated spectra in a wide range of magnetic fields covering Zeeman to Paschen-Back regimes. Robustness of the technique and quality of the agreement suggested to use the derivative of selective reflection from a NC to perform optical vapor magnetometry. We have thus proposed, in chapter 4, a concept to perform optical magnetometry based on NC, making use of the results of chapters 2 and 3. Following the discussion of most suitable operation parameters, we have built a magnetometer extracting the magnetic field value from Rb D_2 line dSR spectra, tested by applying an inhomogeneous magnetic field produced by a permanent ring magnet, serving as a proof of principle. Indeed, our performance analysis has shown a coefficient of variation less than 5% in the range $0.4 - 2$ kG with a measurement time of the order of the minute (acquisition and fitting). Even though the tested range of magnetic fields was limited by the size of the oven and the strength of the ring magnet used in our experiments, the coefficient of variation should be unchanged for magnetic fields of several kG. The calibration curve of the magnetic field as a function of the axial observation distance obtained with our NC-based magnetometer was in a very good agreement with predication of a simple theoretical model as well as measurement realized with a commercial Hall gauge.

Such magnetometer could be applied for numerous physical problems and beyond. Indeed, one of the advantages of NC-magnetometry is the possibility to measure high-gradient fields with a sub-μm spatial resolution thanks to the ultra-small thickness of the vapor column. For example, using the derivative of Selective Reflection from a nanocell with ℓ less than 100 nm could allow to perform the mapping of strongly inhomogeneous magnetic fields, such as for the very high gradient fields (40 kG/mm) used in [134]. One would have however to take van der Waals interactions into account. From the fundamental side, one could make use of the advantages of the NC to perform precise measurement of other alkali lines in a magnetic field, or measurements of linear and non-linear refractive indices of nanometric-thick vapor layers. Having a proper theoretical model, it will be also possible to measure static electric fields (Stark effect) using the same procedure. In addition, it is worth mentioning that the selective reflection signal can be reliably detected at a far distance (tens of meters) from the NC thanks to a low beam divergence, which also proves that this magnetometer is a good candidate for remote sensing magnetic fields, for instance in the difficult environments faced in high energy physics, space and civil engineering.

Outlook of this work include optimization of the magnetometer, for which specific limiting

factors have been addressed in chapter 4 and possible solutions discussed. Particularly, we envisage converting the Mathematica procedure to an open source programming language such as Python. One would thus be able to use A/D pins of the RP computer to perform the recording, lowering the response time of the magnetometer by discarding the serial communication between AD and RP. In addition, optical vapor magnetometry in the Voigt configuration using a mm-long cell was reported in [135] using Stokes polarimetry [129]. Carrying out similar measurements using NC is a natural outlook of this work. Indeed, it should be possible, using the same scheme as presented in this thesis, to measure the magnetic field applied in the plane of polarization of the laser beam. Besides, extending our fitting procedure to the second circularly polarized component should allow revealing also the sign of the measured B-field: for left-hand circularly polarized incident light, σ^+ (σ^-) excitation occurs for positive (negative) projection of B-field along the light propagation axis correspondingly, and vice-versa for the right-hand circularly polarized incident light.

Miniaturization of spectroscopic kits for metrological applications has recently received a lot of attention [136]. In our work we have used relatively cheap electronic components, which is a good step towards development of a compact low-cost commercial device. We should note that also optical nanocells are becoming more affordable as new techniques for their manufacturing are being developed [137].

Appendices

Appendix A

Density matrix and laser field interaction Hamiltonian

A.1 Density matrix

The well-known Schrödinger equation

$$i\hbar\frac{d}{dt}|\Psi\rangle = \mathcal{H}|\Psi\rangle, \tag{A.1}$$

where $\mathcal{H}$ is the Hamiltonian of the system, allows one to express the time dependence of a state vector's projection coefficients (also called probability amplitudes) $c_n(t)$ in a given basis $\{|\psi_n\rangle\}$ such that

$$|\Psi\rangle = \sum_i c_n(t)|\psi_n\rangle, \tag{A.2}$$

where the probability to find the system in the state $|\psi_n\rangle$ at a time t is given by

$$p_n = |c_n(t)|^2 = |\langle\psi_n|\Psi\rangle|^2. \tag{A.3}$$

This picture works very well with for example single atom, however when dealing with an ensemble of atoms it becomes difficult to track each atom individual wave function $|\Psi_i\rangle$. Thus, for a large number of atoms, say N, it is better to use a statistical method, which the density matrix formalism provides [56, 57].

A.1.1 Definition and properties

For a pure state, the density matrix is defined as

$$\rho = |\Psi\rangle\langle\Psi|, \qquad \rho_{nm} = \langle\psi_n|\rho|\psi_m\rangle = c_n \cdot c_m^*, \tag{A.4}$$

where we have omitted the time dependence of the probabilities. From (A.4), one can see that the diagonal elements of the density matrix represent the probabilities to find the system in a

given state; the off-diagonal terms are called as coherence. The density matrix for a mixed state (ensemble of N particles) is usually defined as

$$\rho = \sum_i p_i |\Psi_i\rangle\langle\Psi_i|, \tag{A.5}$$

where p_i is the probability to be in the state $|\Psi_i\rangle$.The density matrix allows to calculate statistical average of a given observable. In experiments, the measured value correspond to the expectation value of the observable one wishes to measure. Let us consider an observable $\mathcal{A}$, the expectation value of $\mathcal{A}$ is given by

$$\langle\mathcal{A}\rangle = \sum_i p_i \langle\Psi_i|\mathcal{A}|\Psi_i\rangle. \tag{A.6}$$

For any complete set of basis vector $\{\psi_n\}$, one has

$$\sum_n |\psi_n\rangle\langle\psi_n| = \mathbb{1}, \tag{A.7}$$

where $\mathbb{1}$ is the identity. Coming back to Eq. (A.6), we have

$$\begin{aligned}\langle\mathcal{A}\rangle &= \sum_i p_i \langle\Psi_i|\mathcal{A}\sum_n |\psi_n\rangle\langle\psi_n||\Psi_i\rangle \\ &= \sum_n \sum_i p_i \langle\Psi_i|\psi_n\rangle\langle\psi_n|\mathcal{A}|\Psi_i\rangle, \\ &= \mathrm{Tr}\left(\rho\mathcal{A}\right),\end{aligned} \tag{A.8}$$

where $\mathrm{Tr}(\rho) = \sum_n \langle\psi_n|\rho|\psi_n\rangle$ is the trace.

A.1.2 Time evolution

The time evolution of the density matrix is found using the Schrödinger equation (A.1) and its conjugate is

$$-i\hbar\frac{d}{dt}\langle\Psi| = \langle\Psi|\mathcal{H}. \tag{A.9}$$

Taking the time derivative of Eq. (A.5), we have

$$\frac{d}{dt}\rho = \sum_i p_i \left(\frac{d}{dt}|\Psi_i\rangle\cdot\langle\Psi_i| + |\Psi_i\rangle\cdot\frac{d}{dt}\langle\Psi_i|\right), \tag{A.10}$$

which using Eqs. (A.1) and (A.9) yields

$$i\hbar\frac{d}{dt}\rho = [\mathcal{H},\rho], \tag{A.11}$$

where $[a,b] = ab - ba$ is the commutator between a and b. This equation is called the (quantum) Liouville equation, which is better suited than the Schrödinger equation for inclusion of statistical distribution. Particularly, when considering moving atoms, one can make use of statistical

averages, say over a Maxwell-Boltzmann distribution of speed. The atomic ensemble will then be described by the density matrix $\rho(v,t)$ and its time evolution is given by the Liouville equation. The only change occurs for the expectation values of operators [56]:

$$\langle \mathcal{A} \rangle = \int_v M(v) \mathrm{Tr}\left(\rho \mathcal{A}\right), \tag{A.12}$$

where $M(v)$ is, for example, the Maxwell-Boltzmann distribution. The density matrix is also extremely convenient, as compared to the Schrödinger equation, for the possibility of including phenomenological processes, such as the relaxation or repopulation. To account these processes, the Liouville equation is then rewritten as [57]

$$i\hbar \frac{d}{dt}\rho = [\mathcal{H}, \rho] - i\hbar \frac{1}{2}\big\{\mathcal{R}, \rho\big\} + i\hbar\Lambda, \tag{A.13}$$

where $\{a,b\} = ab + ba$ is the anti-commutator, $\mathcal{R}$ accounts for relaxation (spontaneous decay, collision, transit, *etc.*) and Λ accounts for repopulation (spontaneous transfer of population, transit, *etc.*).

A.1.3 Useful formulas

To build the density matrix, one may use the formulas from [56]. The equations for the population reads

$$\frac{\partial}{\partial t}\rho_{mm} = -\frac{i}{\hbar}\sum_n \Big[H_{mn}\rho_{nm} - \rho_{mn}H_{nm}\Big] - R_{mm}\rho_{mm} + \sum_{n\neq m}\Gamma_{nm}\rho_{nn} \tag{A.14}$$

and for the coherences

$$\frac{\partial}{\partial t}\rho_{m'm} = -\frac{i}{\hbar}\sum_n \Big(H_{m'n}\rho_{nm} - \rho_{m'n}H_{nm}\Big) - R_{m'm}\rho_{m'm} \tag{A.15}$$

where $\Gamma_{m'm}$ is given by

$$R_{m'm} = \frac{1}{2}\Big(\sum_{n\neq m'}\Gamma_{m'n} + \sum_{n\neq m}\Gamma_{mn}\Big) + [1-\delta(m,m')]\gamma^c_{m'm}. \tag{A.16}$$

In this equation, Γ_{nm} parametrize the flow of population from the state $|n\rangle$ to the state $|m\rangle$ at a rate $\tau_{nm} = 1/\Gamma_{nm}$; $\gamma^c_{m'm}$ represent an additional decoherence rate, due for example to collisions. Let us note that (for a closed system) $R_{nn} = \sum_{m\neq n}\Gamma_{nm}$.

A.2 Laser field interaction Hamiltonian expression

Let us consider an atomic system interacting with a laser light described by an oscillating electric field $\mathbf{E}$. The interaction between the cw light with a frequency $\nu = 2\pi/\omega$ and the atomic system is usually written as

$$\mathcal{H}_L = -\mathbf{d}\cdot\mathbf{E} = \sum_{i\neq j}\mathbf{V}_{ij}|i\rangle\langle j|, \tag{A.17}$$

where $\mathbf{d} = e\mathbf{r}$ is the dipole operator and the electric field of the laser is assumed to have the form

$$\mathbf{E}(\mathbf{r},t) = 2\mathcal{E}\cos(\omega t - \mathbf{k}\cdot\mathbf{r})\,\hat{\mathbf{e}} = \mathcal{E}\exp[-i(\omega t - \mathbf{k}\cdot\mathbf{r})]\,\hat{\mathbf{e}} + c.c., \tag{A.18}$$

with $\mathcal{E}$ its complex amplitude; the vector $\hat{\mathbf{e}}$ describes the polarization of the field. Let us note that when more than one electric field interacts with the atom, Eq. (A.17) is replaced by

$$\mathcal{H}_L = -\mathbf{d}\cdot\sum_n \mathbf{E}_n. \tag{A.19}$$

We want to find a simple expression for the interaction Hamiltonian $\mathcal{H}_L$. The first step consist in making use of the electric dipole approximation.

A.2.1 Electric dipole approximation

The electric dipole approximation, sometimes denoted as E_1, consist in neglecting the spatial phase shift of the wave over the effective atomic space. Here-after, we explain the electric dipole approximation in a simple way; for a more elaborated discussion, see e.g. [138, section 24.5]. The second argument of the cosine function of Eq. (A.18) is $\mathbf{k}\cdot\mathbf{r} = 2\pi r/\lambda$. The energy levels involved in our studies are such that $r \sim r_a$, where $r_a \approx 0.26$ nm is the atomic radius of Cs; obviously one has $r_a^{\mathrm{K}} < r_a^{\mathrm{Rb}} < r_a^{\mathrm{Cs}}$. For optical and near infrared wavelengths, we thus have $r/\lambda \ll 1$, and

$$\exp(i\mathbf{k}\cdot\mathbf{r}) \sim 1, \qquad \mathbf{E}(\mathbf{r},t) \simeq 2\mathcal{E}\cos(\omega t)\,\hat{\mathbf{e}}. \tag{A.20}$$

In fact, one would have arrived at the same conclusion if taking the Bohr radius, the covalent radius, the van der Waal radius or the atomic radius as they range from 0.05 to 0.3 nm, still much smaller than optical wavelengths. The matrix elements V_{ij} of the interaction Hamiltonian thus reduces to

$$V_{ij} = -d_{ij}\cdot\mathcal{E}\big[\exp(-i\omega t) + \exp(i\omega t)\big]\hat{\mathbf{e}}_d\cdot\hat{\mathbf{e}}, \tag{A.21}$$

with $\hat{\mathbf{e}}_d\cdot\hat{\mathbf{e}} \cong 1$ if we suppose alignment of the dipole moment with the incident electric field. The matrix elements of the dipole moment d_{ij} is

$$d_{ij} \equiv \langle j|d|i\rangle = e\langle j|r|i\rangle = e\int d\tau\Psi_j^* r\Psi_i = \exp\left[-i\omega_{ij}t\right]|d_{ij}|, \tag{A.22}$$

with $\omega_{ji} = (E_j - E_i)/\hbar$ and $|d_{ij}| = \int d\tau\varphi_j^*(r)r\varphi_i(r)$. Let us note that as the dipole operator is an odd function, the only possibility for the previous integral to be non-zero is to be evaluated between states of opposite parity.

A.2.2 Rotating wave approximation

Using (A.22) we can rewrite (A.21) as

$$V_{ij} = -|d_{ij}|\big(\mathcal{E}\exp[-i(\omega+\omega_{ij})t] + \mathcal{E}^*\exp[i(\omega-\omega_{ij})t]\big). \tag{A.23}$$

For near-resonant light, one has $\omega - \omega_{ij} \ll 1$, while the term $\exp[-i(\omega + \omega_{ij})t]$ oscillate much faster than $\exp[i(\omega - \omega_{ij})t]$ because $\omega - \omega_{ij} \ll \omega + \omega_{ij}$. The Rotating Wave Approximation (RWA), see e.g. [139, section V.A.3], then consist in neglecting the fast oscillating terms as they will average to zero on any physical time scale. Thus, Eq. (A.23) may be simplified to

$$V_{ij} = -\hbar\Omega_{ij} \exp[i\Delta t] \tag{A.24}$$

where $\Delta = \omega - \omega_{ij}$ is the detuning between the laser field and the atom. In the previous equation, we have defined the Rabi frequency Ω as

$$\Omega_{ij} = \frac{|d_{ij}|\mathcal{E}}{\hbar}. \tag{A.25}$$

Note that if not considering a lossy system, we can assume the Rabi frequency to be real. One should keep in mind that by applying the RWA, one loses some physical effects such as the Bloch-Siegert shift of resonances.

To remove to time dependence in the system Hamiltonian $\mathcal{H} = \mathcal{H}_0 + \mathcal{H}_L$, one can find a unitary transformation $\mathcal{U}$ transforming the eigenbasis into $|\tilde{\Psi}\rangle = \mathcal{U}|\Psi\rangle$, which verify the "new" Schrödinger equation

$$i\hbar\frac{\partial}{\partial t}|\tilde{\Psi}\rangle = \tilde{\mathcal{H}}|\tilde{\Psi}\rangle, \tag{A.26}$$

where transformed Hamiltonian is

$$\tilde{\mathcal{H}} = \mathcal{U}\mathcal{H}\mathcal{U}^\dagger + i\hbar\frac{\partial}{\partial t}\mathcal{U}\cdot\mathcal{U}^\dagger. \tag{A.27}$$

Appendix B

Notes on quantum angular momentum

B.1 Angular momentum, eigenvalues

B.1.1 Definition

We consider a quantum system having an angular momentum $\mathbf{J}$. By the definition of an angular momentum, one has

$$[J_x, J_y] = i\hbar J_z, \tag{B.1}$$

and all others relations by circular permutation (CP) of x, y, z, that is

$$[J_\alpha, J_\beta] = i\hbar\varepsilon(\alpha\beta\gamma)J_\gamma, \quad \varepsilon(\alpha\beta\gamma) = \begin{cases} +1 & \text{if } \alpha\beta\gamma \text{ is a CP of } xyz, \\ -1 & \text{if } \alpha\beta\gamma \text{ is not a CP of } xyz, \\ 0 & \text{in other cases.} \end{cases} \tag{B.2}$$

From these relation, one easily deduces the commutation relation:

$$\left[\mathbf{J}^2, J_z\right] = \left[J_x^2, J_z\right] + \left[J_y^2, J_z\right] = 0. \tag{B.3}$$

Of course we obtain the same relation with J_x and J_y but it is usually the lhs of relation (B.3), *i.e.* J_z, which is chosen (quantization axis choice).

B.1.2 Eigenvalues

As $\mathbf{J}^2$ and J_z commute, it exists a basis simultaneouslty eigenbasis of $\mathbf{J}^2$ and J_z such that

$$\mathbf{J}^2|(k), \lambda, m\rangle = \lambda\hbar^2|(k), \lambda, m\rangle, \tag{B.4a}$$

$$J_z|(k), \lambda, m\rangle = m\hbar|(k), \lambda, m\rangle, \tag{B.4b}$$

where λ and m are real, (k) denotes a set of quantum numbers needed to completely characterized the quantum system, which we later omit. In what follows, we determine λ and m. The definition of the variance of a discrete variable x imposes

$$\langle x^2\rangle \geqslant \langle x\rangle^2. \tag{B.5}$$

With the definition of the expectation value, $\langle \mathcal{A} \rangle = \langle \Psi | \mathcal{A} | \Psi \rangle$ for a normalized state $|\Psi\rangle$, one has

$$\langle \lambda, m | \mathbf{J}^2 | \lambda, m \rangle = \langle \mathbf{J}^2 \rangle = \lambda \hbar^2 \tag{B.6a}$$
$$\langle \lambda, m | J_z | \lambda, m \rangle = \langle J_z \rangle = m\hbar. \tag{B.6b}$$

We thus deduce $\lambda \geqslant m^2$. Let us define new operators from a combination of J_x and J_y:

$$J_+ = J_x + iJ_y, \qquad J_- = J_x - iJ_y, \tag{B.7}$$

which verify the commutation relations

$$[J_z, J_\pm] = \hbar J_\pm, \qquad [J_+, J_-] = 2\hbar J_z, \tag{B.8}$$

and

$$J_\pm \, J_\mp = \mathbf{J}^2 - J_z^2 \pm \hbar J_z, \qquad \mathbf{J}^2 = J_z^2 \tfrac{1}{2}\big(J_+ J_- + J_- J_+\big). \tag{B.9}$$

Let us calculate

$$\begin{aligned} J_z \, J_+ |\lambda, m\rangle &= (J_+ J_z + \hbar J_+) |\lambda, m\rangle \\ &= (m+1)\hbar \, J_+ |\lambda, m\rangle, \end{aligned} \tag{B.10}$$

thus $J_+|\lambda, m\rangle$ is also an eigenvector of J_z. Similarly, $J_-|\lambda, m\rangle$ is also eigenvector of J_z and

$$J_z \, J_- |\lambda, m\rangle = (m-1)\hbar \, J_- |\lambda, m\rangle. \tag{B.11}$$

Making use of Eq. (B.4b), we have

$$\begin{aligned} J_z |\lambda, m \pm 1\rangle &= (m \pm 1)\hbar |\lambda, m \pm 1\rangle, \\ J_z\big(J_\pm |\lambda, m\rangle\big) &= (m \pm 1)\hbar |\lambda, m\rangle. \end{aligned} \tag{B.12}$$

It thus exist a function $C_\pm(\lambda, m)$ such that

$$J_\pm |\lambda, m\rangle = C_\pm(\lambda, m) |\lambda, m \pm 1\rangle, \tag{B.13}$$

which we want to determine. As $\lambda \geqslant m^2$, it exists a maximal value of m, denoted J, such that $J_+|\lambda, J\rangle = 0$. Applying J_- to this relation yields

$$\big(\mathbf{J}^2 - J_z^2 - \hbar J_z\big)|\lambda, J\rangle = 0 \quad \Longrightarrow \quad \hbar^2\lambda^2 - \hbar^2 J^2 - \hbar^2 J = 0, \tag{B.14}$$

thus $\lambda = J(J+1)$. On a similar fashion, it exists a minimal value of m such that $J_-|\lambda, J'\rangle = 0$, and applying J_+ yields $\lambda = J'(J'-1)$. These two relations involving λ are compatible only if $J' = -J$ or $J' = J+1$, which the later is not possible since J' is smaller than J by definition. We thus deduce

$$\lambda = J(J+1), \qquad -J \leqslant m \leqslant J. \tag{B.15}$$

By applying J_- a sufficient amount of time, one passes from $|\lambda, J\rangle$ to $|\lambda, -J\rangle$:

$$\big(J_-\big)^{2J} |\lambda, J\rangle = \big(C_-(\lambda, m)\big)^{2J} |\lambda, -J\rangle, \tag{B.16}$$

hence J is an integer or half-integer. It remains to find the expression of $C_\pm(\lambda, m)$; let us calculate $|J_+|\lambda, m\rangle|^2$:

$$\begin{aligned} & \big(J_+|\lambda,m\rangle\big)^*\big(J_+|\lambda,m\rangle\big) = \big(C_+(\lambda,m)\hbar|\lambda,m+1\rangle\big)^*\big(C_+(\lambda,m)\hbar|\lambda,m+1\rangle\big) \\ \Longrightarrow \quad & \langle\lambda,m|J_-J_+|\lambda,m\rangle = \hbar^2\,|C_+(\lambda,m)|^2\langle\lambda,m+1|\lambda,m+1\rangle \\ \Longrightarrow \quad & \langle\lambda,m|\mathbf{J}^2 - J_z^2 - \hbar J_z|\lambda,m\rangle = \hbar^2|C_+(\lambda,m)|^2. \end{aligned} \tag{B.17}$$

One thus arrives at

$$\langle\mathbf{J}^2\rangle - \langle J_z^2\rangle - \hbar\langle J_z\rangle = |C_+(\lambda,m)|^2, \tag{B.18}$$

which yields $|C_+(\lambda,m)|^2 = J(J+1) - m^2 - m$. In a similar way, one finds $|C_-(\lambda,m)|^2 = J(J+1) - m^2 + m$. Finally, the most natural choice leads to

$$C_\pm(\lambda,m) = \sqrt{J(J+1) - m(m\pm1)}. \tag{B.19}$$

To summarize:

$$\mathbf{J}^2|J,m\rangle = J(J+1)\hbar^2\,|J,m\rangle, \tag{B.20a}$$
$$J_z|J,m\rangle = m\hbar\,|J,m\rangle, \tag{B.20b}$$
$$J_+|J,m\rangle = \hbar\sqrt{J(J+1) - m(m+1)}\,|J,m+1\rangle, \tag{B.20c}$$
$$J_-|J,m\rangle = \hbar\sqrt{J(J+1) - m(m-1)}\,|J,m-1\rangle, \tag{B.20d}$$

with $-J \leqslant m \leqslant J$. One could have denoted $|J(J+1),m\rangle$ the common basis, but as there is a bijective relation $J \leftrightarrow J(J+1)$, it is thus simpler to denote it $|J,m\rangle$.

B.2 Coupling of two angular momenta

B.2.1 Generalities

Let us consider two sub-quantum systems described by the angular momenta $\mathbf{J}_1$ and $\mathbf{J}_2$, verifying the relations derived in section B.1. A possible basis of the the total quantum system is formed by the tensorial product of the $(2J_1+1)$ kets $|J_1,m_1\rangle$, of the first sub-system, by the $(2J_2+1)$ $|J_2,m_2\rangle$, of the second sub-system. We thus obtain $(2J_1+1)(2J_2+1)$ common eigenkets of J_1^2, J_2^2, J_{1z}, J_{2z}:

$$|J_1,m_1\rangle|J_2,m_2\rangle \equiv |J_1,m_1,J_2,m_2\rangle \equiv |J_1J_2,m_1m_2\rangle. \tag{B.21}$$

But one may also consider the total angular momentum $\mathbf{J}$ of the total quantum system:

$$\mathbf{J} = \mathbf{J}_1 + \mathbf{J}_2. \tag{B.22}$$

The four operators $\mathbf{J}^2$, $J_z, \mathbf{J}_1^2, \mathbf{J}_2^2$ are all commuting operators. Hence, it necessarily exists a common basis to these four operators: $\{|J_1J_2,Jm\rangle\}$ with

$$|J_1 - J_2| \leqslant J \leqslant J_1 + J_2 \tag{B.23a}$$
$$-J \leqslant m \leqslant J. \tag{B.23b}$$

The dimension of the basis is obviously $(2J_1+1)(2J_2+1)$ as it describes the same quantum system. It also exists an unitary transformation from the basis $\{|J_1m_1, J_2m_2\rangle\}$ to the basis $\{|J_1J_2, Jm\rangle\}$ which can be denoted as:

$$\begin{aligned}|J_1J_2, Jm\rangle &= \mathbb{1}|J_1J_2, Jm\rangle \\ &= \sum_{m_1=-J_1}^{+J_1}\sum_{m_2=-J_2}^{+J_2} |J_1m_1, J_2m_2\rangle\langle J_1m_1, J_2m_2||J_1J_2, Jm\rangle \\ &= \sum_{m_1=-J_1}^{+J_1}\sum_{m_2=-J_2}^{+J_2} \langle J_1m_1, J_2m_2|J_1J_2, Jm\rangle|J_1m_1, J_2m_2\rangle.\end{aligned} \tag{B.24}$$

The symbols $\langle J_1m_1, J_2m_2|J_1J_2, Jm\rangle$, sometimes denoted as $\langle J_1m_1, J_2m_2|Jm\rangle$, are called Clebsh-Gordan coefficients (CG).

B.2.2 Some properties and notations of CG, 3-j and 6-j symbols

By choice, all CG are real, particularly, the coefficient

$$\langle J_1J_2, m_1 = J_1\ m_2 = J_2|J_1J_2, J\ m = J\rangle = \langle J_1J_2, J_1J - J_1|JJ\rangle \tag{B.25}$$

is chosen real and positive. Obviously, $J_z = J_{1z} + J_{2z}$, that is to say $m = m_1 + m_2$ (called Δm rule for CG). One often uses the the 3-j symbol of Wigner defined as follows

$$\begin{pmatrix} J_1 & J_2 & J \\ m_1 & m_2 & -m \end{pmatrix} = \frac{(-1)^{J_1-J_2+m}}{\sqrt{2J+1}}\langle J_1m_1, J_2m_2|J_1J_2, Jm\rangle. \tag{B.26}$$

For the 3-j symbols of Wigner, the Δm rule reads $m + m_1 + m_2 = 0$. It is also interesting to note the following properties: a 3-j symbol is invariant in a circular permutation of columns; for non circular permutations, the 3-j symbol is multiplied by $(-1)^{J_1+J_2+J}$. The 3-j symbols can be computed using the Racah formula, see e.g. [140, 141].

In (B.24), one goes from uncoupled basis $|J_1m_1, J_2m_2\rangle$ to coupled basis $|J_1J_2, Jm\rangle$ (coupled basis because one has coupled $\mathbf{J}_1$ and $\mathbf{J}_2$ such that $\mathbf{J} = \mathbf{J}_1 + \mathbf{J}_2$). The inverse transformation is obviously possible, that is

$$|J_1m_1, J_2m_2\rangle = \sum_{J=|J_1-J_2|}^{J_1+J_2}\sum_{m=-J}^{+J} \langle J_1J_2, Jm|J_1m_1, J_2m_2\rangle|J_1J_2, Jm\rangle. \tag{B.27}$$

The coefficients which allow the passage from coupled basis $|J_1J_2, Jm\rangle$ to uncoupled one are thus $\langle J_1J_2, Jm|J_1m_1, J_2m_2\rangle$. By definition, $\langle\Phi|\Psi\rangle^* = \langle\Psi|\Phi\rangle$, so

$$\begin{aligned}\langle J_1m_1, J_2m_2|J_1J_2, Jm\rangle^* &= \langle J_1J_2, Jm|J_1m_1, J_2m_2\rangle \\ &= \langle J_1m_1, J_2m_2|J_1J_2, Jm\rangle,\end{aligned}$$

where we have used the fact that CG coefficients are real. Consequently, these coefficients allow the passage from the coupled basis to the uncoupled one.

In an analogous way as in section B.2.1, one can couple three angular momenta together. In this case, 3-j symbols will be replaced by 6-j symbols having the following definition:

$$\begin{Bmatrix} J_1 & J_2 & J_3 \\ J_4 & J_5 & J_6 \end{Bmatrix} = \sum_{m_1,\ldots,m_6} (-1)^{\alpha} \begin{pmatrix} J_1 & J_2 & J_3 \\ -m_1 & -m_2 & -m_3 \end{pmatrix} \begin{pmatrix} J_1 & J_5 & J_6 \\ m_1 & -m_5 & m_6 \end{pmatrix} \times \begin{pmatrix} J_4 & J_2 & J_6 \\ m_4 & m_2 & -m_6 \end{pmatrix} \begin{pmatrix} J_4 & J_5 & J_3 \\ -m_4 & m_5 & m_3 \end{pmatrix}, \tag{B.28}$$

where $\alpha = \sum_{k=1}^{6}(J_k - m_k)$; the summation is done over all six m_i value allowed by 3-j symbol selection rules. Computation of 6-j symbols can also be acheived with Racah formulas, see [140, 141].

B.3 Tensorial operators, Wigner-Eckart Theorem and applications

B.3.1 Definition

The standard components of a vectorial operator $\mathbf{V}$, also called tensorial operator of order 1 verify the following relations:

$$\left[J_{\pm}, V_q^{(1)}\right] = \hbar\sqrt{1(1+1) - q(q\pm 1)}V_{q\pm 1}^{(1)}, \tag{B.29a}$$

$$\left[J_z, V_q^{(1)}\right] = \hbar q V_q^{(1)}, \tag{B.29b}$$

with $q = -1, 0, 1$. These relations can be generalized for the $(2k+1)$ components of an Irreductible Tensorial Operator (ITO) of order k:

$$\left[J_{\pm}, T_q^{(k)}\right] = \hbar\sqrt{k(k+k) - q(q\pm 1)}T_{q\pm 1}^{(k)}, \tag{B.30a}$$

$$\left[J_z, T_q^{(k)}\right] = \hbar q T_q^{(k)}, \tag{B.30b}$$

with $-k \leqslant q \leqslant k$.

B.3.2 The Wigner-Eckart Theorem

An important theorem when dealing with tensorial operators is the so-called Wigner-Eckart (WE) theorem [92, 142, 143]. Its importance lies in the fact that when evaluating matrix elements of tensorial operators it allows one to separate factors depending on the quantization axis (*i.e.* depending on the geometry of the system) from those representing the physical content. This theorem results from a comparison between the relations satisfied by the matrix elements of tensorial operators and CG coefficients. In the literature, one often finds the WE theorem written as

$$\langle \alpha J m_J | T_q^{(k)} | \alpha' J' m'_J \rangle = (-1)^{J-m_J} \begin{pmatrix} J & k & J' \\ -m_J & q & m'_J \end{pmatrix} \langle \alpha J || T^{(k)} || \alpha' J' \rangle \tag{B.31}$$

where T_q^k is an ITO whose matrix elements are calculated between the sates $|\alpha J m_J\rangle$ and $|\alpha' J' m'_J\rangle$; the (reduced matrix element) term $\langle \alpha, j || T^k || \alpha', j' \rangle$ expresses a term independent of

m'_J, m_J and q. Direct consequences of this theorem, and the $3j$ symbol it contains, are the selection rules. Using the properties of the $3j$ symbols and the WE theorem, one finds that

$$\langle \alpha J m_J | T^{(k)}_q | \alpha' J' m'_J \rangle \neq 0 \tag{B.32}$$

only if $\Delta m_J = q$, $J - k \leqslant J' \leqslant J + k$ and $J' + J \geqslant k$. In the case of a rank 1 ITO ($k = 1$, $q = 0, \pm 1$), we have the following selection rules

$$\Delta J = 0, \pm 1, \qquad \Delta m_J = 0, \pm 1, \qquad J' + J \geqslant 1. \tag{B.33}$$

B.3.3 Applications of the Wigner-Eckart Theorem

We want to calculate the reduced matrix element of an ITO. Let us consider a tensorial operator of rank 1 such that $T^{(1)}_0 = J^{(1)}_0$ the application of the WE theorem yields

$$\langle J m_J | J^{(1)}_0 | J' m'_J \rangle = (-1)^{J - m_J} \begin{pmatrix} J & 1 & J' \\ -m_J & 0 & m'_J \end{pmatrix} \langle J || J^{(1)} || J' \rangle. \tag{B.34}$$

By definition, we have $\langle J m_J | J^{(1)}_0 | J' m'_J \rangle = \hbar m \delta_{JJ'} \delta_{m_J m'_J}$. Noting that

$$\begin{pmatrix} J & 1 & J \\ -m_J & 0 & m'_J \end{pmatrix} = (-1)^{J - m_J} \frac{m}{\sqrt{J(J+1)(2J+1)}} \delta_{m_J m'_J}, \tag{B.35}$$

we find that the expression of the reduced matrix element of $J^{(1)}_0$ is given by

$$\langle J || J^{(1)} || J' \rangle = \sqrt{J(J+1)(2J+1)} \delta_{JJ'}. \tag{B.36}$$

This last relation is independent of q, thus we can generalize for every component of J. Hence

$$\langle J m_J | J^{(1)}_q | J' m'_J \rangle = (-1)^{J - m_J} \begin{pmatrix} J & 1 & J' \\ -m_J & q & m'_J \end{pmatrix} \sqrt{J(J+1)(2J+1)} \delta_{JJ'}. \tag{B.37}$$

As of particular cases, one can note

$$\langle L || L^{(1)} || L \rangle = \sqrt{L(L+1)(2L+1)}, \qquad \langle S || S^{(1)} || S \rangle = \sqrt{S(S+1)(2S+1)}. \tag{B.38}$$

Another useful formula arising from the WE theorem allows to decouple the reduced matrix elements. Let us consider an ITO $T^{(k)}$ which only acts on $|\alpha_1 J_1 m_1\rangle$. One can demonstrate (see for example [143]) that the reduced matrix element expressed in the coupled basis reads

$$\begin{aligned} \langle \alpha_1 J_1 \alpha_2 J_2, J || T^{(k)} || \alpha'_1 J'_1 \alpha'_2 J'_2, J' \rangle &= (-1)^{J_1 + J_2 + J' + k} \sqrt{2J+1} \sqrt{2J'+1} \\ &\times \delta(\alpha_2 J_2, \alpha'_2 J'_2) \begin{Bmatrix} J_1 & J_2 & J \\ J' & k & J'_1 \end{Bmatrix} \langle \alpha_1 J_1 || T^{(k)} || \alpha'_1 J'_1 \rangle, \end{aligned} \tag{B.39}$$

where the curly brace matrix denotes a 6-j symbol. In the previous relation's lhs, we have omitted the projections as the reduced matrix elements are independent of m_J.

Bibliography

[1] T. H. Maiman. *Stimulated Optical Radiation in Ruby*. Nature **187**(4736), (1960) 493. 2

[2] W. Demtröder. *Laser spectroscopy: basic concepts and instrumentation*. Springer (2003). 2, 5, 6, 7

[3] L. Weller, K. S. Kleinbach, M. A. Zentile, S. Knappe, I. G. Hughes, and C. S. Adams. *Optical isolator using an atomic vapor in the hyperfine Paschen-Back regime*. Opt. Lett. **37**(16), (2012) 3405. 2, 70, 73, 76

[4] W. Kiefer, R. Löw, J. Wrachtrup, and I. Gerhardt. *Na-Faraday rotation filtering: The optimal point*. Sci. Rep. **4**, (2014) 6552. 2

[5] D.-Q. Su, T.-F. Meng, Z.-H. Ji, J.-P. Yuan, Y.-T. Zhao, L.-T. Xiao, and S.-T. Jia. *Application of sub-Doppler DAVLL to laser frequency stabilization in atomic cesium*. Appl. Opt. **53**(30), (2014) 7011. 2

[6] G. W. Truong, J. D. Anstie, E. F. May, T. M. Stace, and A. N. Luiten. *Accurate lineshape spectroscopy and the Boltzmann constant*. Nat. Commun. **6**, (2015) 8345. 2

[7] A. D. Ludlow, M. M. Boyd, J. Ye, E. Peik, and P. O. Schmidt. *Optical atomic clocks*. Rev. Mod. Phys. **87**, (2015) 637. 2

[8] J. Kitching, S. Knappe, and E. A. Donley. *Atomic Sensors – A Review*. IEEE Sens. J. **11**(9), (2011) 1749. 2

[9] D. Budker and D. Kimball. *Optical Magnetometry*. Cambridge Univ. Press, Cambridge (2013). 2, 80

[10] W. Yang, D. B. Conkey, B. Wu, D. Yin, A. R. Hawkins, and H. Schmidt. *Atomic spectroscopy on a chip*. Nat. Photon. **1**, (2007) 331. 2

[11] M. H. Anderson, J. R. Ensher, M. R. Matthews, C. E. Wieman, and E. A. Cornell. *Observation of Bose-Einstein Condensation in a Dilute Atomic Vapor*. Science **269**(5221), (1995) 198. 2

[12] K. B. Davis, M. O. Mewes, M. R. Andrews, N. J. van Druten, D. S. Durfee, D. M. Kurn, and W. Ketterle. *Bose-Einstein Condensation in a Gas of Sodium Atoms*. Phys. Rev. Lett. **75**, (1995) 3969. 2

[13] M. Saffman, T. G. Walker, and K. Mølmer. *Quantum information with Rydberg atoms*. Rev. Mod. Phys. **82**, (2010) 2313. 2

[14] C. Carr, R. Ritter, C. G. Wade, C. S. Adams, and K. J. Weatherill. *Nonequilibrium Phase Transition in a Dilute Rydberg Ensemble*. Phys. Rev. Lett. **111**, (2013) 113901. 2

[15] J. J. Maki, M. S. Malcuit, J. E. Sipe, and R. W. Boyd. *Linear and nonlinear optical measurements of the Lorentz local field*. Phys. Rev. Lett. **67**, (1991) 972. 2

[16] J. Keaveney, A. Sargsyan, U. Krohn, I. G. Hughes, D. Sarkisyan, and C. S. Adams. *Cooperative Lamb Shift in an Atomic Vapor Layer of Nanometer Thickness*. Phys. Rev. Lett. **108**, (2012) 173601. 2, 25, 40

[17] J. Keaveney. *Cooperative interactions in dense thermal Rb vapour confined in nm-scale cells*. Ph.D. thesis, Durham University (2013). 2, 9, 43

[18] K. A. Whittaker, J. Keaveney, I. G. Hughes, A. Sargsyan, D. Sarkisyan, and C. S. Adams. *Optical Response of Gas-Phase Atoms at Less than $\lambda/80$ from a Dielectric Surface*. Phys. Rev. Lett. **112**, (2014) 253201. 2

[19] M. Marinescu, H. R. Sadeghpour, and A. Dalgarno. *Dispersion coefficients for alkali-metal dimers*. Phys. Rev. A **49**, (1994) 982. 2

[20] S. Vdović, D. Sarkisyan, and G. Pichler. *Absorption spectrum of rubidium and cesium dimers by compact computer operated spectrometer*. Opt. Commun. **268**(1), (2006) 58. 2

[21] R. Miles and S. Harris. *Optical third-harmonic generation in alkali metal vapors*. IEEE J. Quantum Electron. **9**(4), (1973) 470. 2

[22] N. Šantić, A. Fusaro, S. Salem, J. Garnier, A. Picozzi, and R. Kaiser. *Nonequilibrium Precondensation of Classical Waves in Two Dimensions Propagating through Atomic Vapors*. Phys. Rev. Lett. **120**, (2018) 055301. 2

[23] R. W. Boyd and P. Narum. *Slow- and fast-light: fundamental limitations*. J. Mod. Opt. **54**(16-17), (2007) 2403. 2

[24] R. W. Boyd, L. Hau, H. Wang, G. Eisenstein, S. Noda, and J. Moerk. *Slow Light and Its Applications*. J. Opt. Soc. Am. B **25**(12), (2008) 136. 2

[25] C. B. Alcock, V. P. Itkin, and M. K. Horrigan. *Vapour Pressure Equations for the Metallic Elements: 298–2500K*. Can. Metal. Quart. **23**(3), (1984) 309. 3, 68

[26] W. Demtröder. *Atoms, molecules and photons*. Springer (2010). 3, 7

[27] E. Arimondo, M. Inguscio, and P. Violino. *Experimental determinations of the hyperfine structure in the alkali atoms*. Rev. Mod. Phys. **49**, (1977) 31. 4, 51, 80

[28] T. Tiecke. *Properties of potassium* (2019). 5, 30, 54, 76, 78

[29] D. A. Steck. *Rubidium 85 D line data* (2013). 5, 30, 54

[30] D. A. Steck. *Cesium D line data* (2010). 5, 30

[31] J. R. Beacham and K. L. Andrew. *Optical Study of the Hyperfine Structure of the Rubidium Resonance Lines.* J. Opt. Soc. Am. **61**(2), (1971) 231. 7

[32] R. Wood. *The selective reflection of monochromatic light by mercury vapor.* Phil. Mag. **18**, (1909) 187. 8

[33] M. Schuurmans. *Spectral narrowing of selective reflection.* J. Phys. France **37**(5), (1976) 469. 9

[34] M. Ducloy and M. Fichet. *General theory of frequency modulated selective reflection. Influence of atom surface interactions.* J. Phys. II France **1**(12), (1991) 1429. 9, 26

[35] A. Akul'Shin, V. Velichanskii, A. Zibrov, V. Nikitin, V. Sautenkov, E. Yurkin, and N. Senkov. *Collisional broadening of intra-Doppler resonances of selective reflection on the D2 line of cesium.* J. Exp. Theor. Phys. Lett. **36**(303), (1982) 59. 9

[36] J. Guo, J. Cooper, and A. Gallagher. *Selective reflection from a dense atomic vapor.* Phys. Rev. A **53**, (1996) 1130. 9

[37] M. Chevrollier, M. Fichet, M. Oria, G. Rahmat, D. Bloch, and M. Ducloy. *High resolution selective reflection spectroscopy as a probe of long-range surface interaction: measurement of the surface van der Waals attraction exerted on excited Cs atoms.* J. Phys. II France **2**(4), (1992) 631. 9

[38] S. Briaudeau, D. Bloch, and M. Ducloy. *Detection of slow atoms in laser spectroscopy of a thin vapor film.* Eur. Phys. Lett. **35**(5), (1996) 337. 9

[39] D. Sarkisyan, D. Bloch, A. Papoyan, and M. Ducloy. *Sub-Doppler spectroscopy by sub-micron thin Cs vapour layer.* Opt. Commun. **200**(1), (2001) 201. 9

[40] K. A. Whittaker, J. Keaveney, I. G. Hughes, A. Sargsyan, D. Sarkisyan, and C. S. Adams. *Optical Response of Gas-Phase Atoms at Less than $\lambda/80$ from a Dielectric Surface.* Phys. Rev. Lett. **112**, (2014) 253201. 9, 40

[41] H. Hakhumyan. *Study of optical and magneto processes in Rb atomic vapor layer of nanometric thickness.* Ph.D. thesis, Université de Bourgogne (2012). 9

[42] J.-M. Hartmann, X. Landsheere, C. Boulet, D. Sarkisyan, A. S. Sarkisyan, C. Leroy, and E. Pangui. *Infrared look at the spectral effects of submicron confinements of CO_2 gas.* Phys. Rev. A **93**, (2016) 012516. 9

[43] A. Sargsyan, E. Klinger, Y. Pashayan-Leroy, C. Leroy, A. Papoyan, and D. Sarkisyan. *Selective reflection from Rb vapor in half- and quarter-wave cells: Features and possible applications.* J. Exp. Theor. Phys. Lett. **104**(4), (2016) 224. 12, 26, 41

[44] A. Sargsyan, E. Klinger, G. Hakhumyan, A. Tonoyan, A. Papoyan, C. Leroy, and D. Sarkisyan. *Decoupling of hyperfine structure of Cs D_1 line in strong magnetic field studied by selective reflection from a nanocell.* J. Opt. Soc. Am. B **34**(4), (2017) 776. 12, 26

[45] E. Klinger, A. Sargsyan, A. Tonoyan, G. Hakhumyan, A. Papoyan, C. Leroy, and D. Sarkisyan. *Magnetic field-induced modification of selection rules for Rb D_2 line monitored by selective reflection from a vapor nanocell.* Eur. Phys. J. D **71**(8), (2017) 216. 12, 26

[46] E. Klinger, A. Sargsyan, C. Leroy, and D. Sarkisyan. *Selective reflection of laser radiation from submicron layers of Rb and Cs atomic vapors: Applications in atomic spectroscopy.* J. Exp. Theor. Phys. **125**(4), (2017) 543. 12, 26, 41

[47] A. Tonoyan, A. Sargsyan, E. Klinger, G. Hakhumyan, C. Leroy, M. Auzinsh, A. Papoyan, and D. Sarkisyan. *Circular dichroism of magnetically induced transitions for D_2 lines of alkali atoms.* Eur. Phys. Lett. **121**(5), (2018) 53001. 12, 62, 63

[48] A. Sargsyan, E. Klinger, A. Tonoyan, C. Leroy, and D. Sarkisyan. *Hyperfine Paschen-Back regime of potassium D_2 line observed by Doppler-free spectroscopy.* J. Phys. B: At. Mol. Opt. Phys. **51**(14), (2018) 145001. 12, 89

[49] E. Klinger. *Concept of an Optical Magnetometer Based on the Spectroscopy of Alkali Vapors Confined in Nanometric-Thick Cells.* J. Contem. Phys. (Armenian Ac. Sci.) **53**(4), (2018) 313. 12, 88

[50] A. Sargsyan, E. Klinger, C. Leroy, T. A. Vartanyan, and D. Sarkisyan. *Circular Dichroism of Atomic Transitions of the Rb D_1 Line in Magnetic Fields.* Opt. Spectrosc. **125**(6), (2018) 833. 12

[51] R. H. Romer and R. H. Dicke. *New Technique for High-Resolution Microwave Spectroscopy.* Phys. Rev. **99**, (1955) 532. 16, 29

[52] T. A. Vartanyan and D. L. Lin. *Enhanced selective reflection from a thin layer of a dilute gaseous medium.* Phys. Rev. A **51**, (1995) 1959. 16

[53] B. Zambon and G. Nienhuis. *Reflection and transmission of light by thin vapor layers.* Opt. Commun. **143**(4), (1997) 308. 16, 21, 28

[54] G. Dutier, S. Saltiel, D. Bloch, and M. Ducloy. *Revisiting optical spectroscopy in a thin vapor cell: mixing of reflection and transmission as a Fabry–Perot microcavity effect.* J. Opt. Soc. Am. B **20**(5), (2003) 793. 16, 23, 26

[55] T. Peyrot, Y. R. P. Sortais, J.-J. Greffet, A. Browaeys, A. Sargsyan, J. Keaveney, I. G. Hughes, and C. S. Adams. *Optical Transmission of an Atomic Vapor in the Mesoscopic Regime.* Phys. Rev. Lett. **122**, (2019) 113401. 16

[56] B. W. Shore. *The Theory of Coherent Atomic Excitation, Volume 1, Simple Atoms and Fields* (1990). 20, 97, 99

[57] M. Auzinsh, D. Budker, and S. Rochester. *Optically polarized atoms: understanding light-atom interactions*. Oxford University Press (2010). 20, 97, 99

[58] P. Todorov and D. Bloch. *Testing the limits of the Maxwell distribution of velocities for atoms flying nearly parallel to the walls of a thin cell*. J. Chem. Phys. **147**(19), (2017) 194202. 21

[59] Y. Pashayan-Leroy, C. Leroy, A. Sargsyan, A. Papoyan, and D. Sarkisyan. *Electromagnetically induced transparency: the thickness of the vapor column is of the order of a light wavelength*. J. Opt. Soc. Am. B **24**(8), (2007) 1829. 21

[60] S. Briaudeau, D. Bloch, and M. Ducloy. *Sub-Doppler spectroscopy in a thin film of resonant vapor*. Phys. Rev. A **59**, (1999) 3723. 26

[61] D. A. Steck. *Rubidium 87 D line data* (2015). 30, 54

[62] A. D. Sargsyan, G. T. Hakhumyan, A. S. Sarkisyan, A. O. Amiryan, and D. Sarkisyan. *Frequency reference for atomic transitions of Rb D_2 line based on the effect of selective reflection*. J. Contemp. Phys. (Armenian Ac. Sci.) **51**(4), (2016) 312. 32

[63] D. Bloch, M. Ducloy, N. Senkov, V. Velichansky, and V. Yudin. *Doppler-Free Spectroscopy of the D1 Line of Potassium*. Laser Phys. **6**, (1996) 670. 32, 72

[64] W. T. Silfvast. *Laser fundamentals*. Cambridge university press (2004). 32

[65] G. Dutier. *Cavité nanométrique de vapeur de Césium: spectroscopie à haute résolution et interaction de surface de type van der Waals*. Ph.D. thesis, Université Paris-Nord-Paris XIII (2003). 33

[66] A. Sargsyan, Y. Pashayan-Leroy, C. Leroy, Y. Malakyan, and D. Sarkisyan. *Features of faraday rotation in cs atomic vapor in a cell thinner than the wavelength of light*. J. Exp. Theor. Phys. Lett. **102**(8), (2015) 487. 35, 75

[67] A. Sargsyan, A. Tonoyan, R. Mirzoyan, D. Sarkisyan, A. M. Wojciechowski, A. Stabrawa, and W. Gawlik. *Saturated-absorption spectroscopy revisited: atomic transitions in strong magnetic fields ($>$ 20 mT) with a micrometer-thin cell*. Opt. Lett. **39**(8), (2014) 2270. 37, 72

[68] D. E. Thornton, G. T. Phillips, and G. P. Perram. *Velocity changing collisions in the laser saturation spectra of ^{87}Rb D_2 $F'' = 2$*. Opt. Commun. **284**(12), (2011) 2890. 38

[69] G. Hakhumyan, A. Sargsyan, C. Leroy, Y. Pashayan-Leroy, A. Papoyan, and D. Sarkisyan. *Essential features of optical processes in neon-buffered submicron-thin Rb vapor cell*. Opt. Express **18**(14), (2010) 14577. 38, 39

[70] W. Happer. *Optical Pumping*. Rev. Mod. Phys. **44**, (1972) 169. 39

[71] J. Kitching. *Chip-scale atomic devices*. Appl. Phys. Rev. **5**(3), (2018) 031302. 39

[72] D. Bloch and M. Ducloy. *Atom-wall interaction.* Adv. At. Mol. Opt. Phys. **50**, (2005) 91. 40, 43

[73] V. Sandoghdar, C. I. Sukenik, E. A. Hinds, and S. Haroche. *Direct measurement of the van der Waals interaction between an atom and its images in a micron-sized cavity.* Phys. Rev. Lett. **68**, (1992) 3432. 40

[74] T. Peyrot, N. Šibalić, Y. Sortais, A. Browaeys, A. Sargsyan, D. Sarkisyan, I. Hughes, and C. Adams. *Measurement of the atom-surface van der Waals interaction by transmission spectroscopy in a wedged nano-cell.* arXiv:0805.2613 (arXiv preprint), (2019) 1. 40

[75] H. B. G. Casimir and D. Polder. *The Influence of Retardation on the London-van der Waals Forces.* Phys. Rev. **73**, (1948) 360. 40

[76] A. Laliotis, T. P. de Silans, I. Maurin, M. Ducloy, and D. Bloch. *Casimir–Polder interactions in the presence of thermally excited surface modes.* Nat. Commun. **5**, (2014) 4364. 40

[77] M. Fichet, G. Dutier, A. Yarovitsky, P. Todorov, I. Hamdi, I. Maurin, S. Saltiel, D. Sarkisyan, M.-P. Gorza, D. Bloch, and M. Ducloy. *Exploring the van der Waals atom-surface attraction in the nanometric range.* Eur. Phys. Lett. **77**(5), (2007) 54001. 40

[78] K. A. Whittaker, J. Keaveney, I. G. Hughes, A. Sargsyan, D. Sarkisyan, and C. S. Adams. *Spectroscopic detection of atom-surface interactions in an atomic-vapor layer with nanoscale thickness.* Phys. Rev. A **92**, (2015) 052706. 40, 43

[79] A. Sargsyan, Y. Pashayan-Leroy, C. Leroy, and D. Sarkisyan. *Collapse and revival of a Dicke-type coherent narrowing in potassium vapor confined in a nanometric thin cell.* J. Phys. B: At. Mol. Opt. Phys. **49**(7), (2016) 075001. 40, 73

[80] A. Sargsyan, A. Tonoyan, J. Keaveney, I. Hughes, C. Adams, and D. Sarkisyan. *Selective reflection of potassium vapor nanolayers in a magnetic field.* J. Exp. Theor. Phys. **126**(3), (2018) 293. 41

[81] A. Sargsyan, A. Papoyan, I. G. Hughes, C. S. Adams, and D. Sarkisyan. *Selective reflection from an Rb layer with a thickness below $\lambda/12$ and applications.* Opt. Lett. **42**(8), (2017) 1476. 41, 76

[82] T. Peyrot, Y. R. P. Sortais, A. Browaeys, A. Sargsyan, D. Sarkisyan, J. Keaveney, I. G. Hughes, and C. S. Adams. *Collective Lamb Shift of a Nanoscale Atomic Vapor Layer within a Sapphire Cavity.* Phys. Rev. Lett. **120**, (2018) 243401. 43

[83] W. D. Phillips. *Nobel Lecture: Laser cooling and trapping of neutral atoms.* Rev. Mod. Phys. **70**, (1998) 721. 46

[84] K. L. Corwin, Z.-T. Lu, C. F. Hand, R. J. Epstein, and C. E. Wieman. *Frequency-stabilized diode laser with the Zeeman shift in an atomic vapor.* Appl. Opt. **37**(15), (1998) 3295. 46

[85] G. E. Santyr, R. M. Henkelman, and M. J. Bronskill. *Spin locking for magnetic resonance imaging with application to human breast.* Magn. Reson. Med. **12**(1), (1989) 25. 46

[86] W. P. Aue, E. Bartholdi, and R. R. Ernst. *Two-dimensional spectroscopy. Application to nuclear magnetic resonance.* J. Chem. Phys. **64**(5), (1976) 2229. 46

[87] T. D. Barrett, D. Stuart, O. Barter, and A. Kuhn. *Nonlinear Zeeman effects in the cavity-enhanced emission of polarised photons.* New J. Phys. **20**(7), (2018) 073030. 46

[88] P. Tremblay, A. Michaud, M. Levesque, S. Thériault, M. Breton, J. Beaubien, and N. Cyr. *Absorption profiles of alkali-metal D lines in the presence of a static magnetic field.* Phys. Rev. A **42**, (1990) 2766. 46, 51, 55, 62, 69

[89] C. Cohen-Tannoudji, B. Diu, and F. Laloë. *Quantum Mechanics I.* (Paris: Hermann) (1977). 47

[90] W. Johnson and G. Soff. *The lamb shift in hydrogen-like atoms* $1 \leq Z \leq 110$. Atomic Data and Nuclear Data Tables **33**(3), (1985) 405. 49

[91] D. Hanneke, S. Fogwell, and G. Gabrielse. *New measurement of the electron magnetic moment and the fine structure constant.* Phys. Rev. Lett. **100**(12), (2008) 120801. 49

[92] E. Biémont. *Spectroscopie atomique: Instrumentation et structures atomiques.* De Boeck Supérieur (2006). 50, 107

[93] D. A. Varshalovich, A. N. Moskalev, and V. K. M. Khersonskii. *Quantum theory of angular momentum.* World Scientific (1988). 50

[94] V. Gerginov, A. Derevianko, and C. E. Tanner. *Observation of the Nuclear Magnetic Octupole Moment of* ^{133}Cs. Phys. Rev. Lett. **91**, (2003) 072501. 51

[95] A. Corney. *Atomic and laser spectroscopy.* Clarendon Press Oxford (1978). 52

[96] E. B. Aleksandrov, G. I. Khvostenko, and M. P. Chaika. *Interference of atomic states.* Springer-Verlag, Berlin (1993). 52

[97] G. Breit and I. I. Rabi. *Measurement of Nuclear Spin.* Phys. Rev. **38**, (1931) 2082. 52

[98] E. de Clercq, M. de Labachellerie, G. Avila, P. Cerez, and M. Tetu. *Laser diode optically pumped caesium beam.* J. Phys. France **45**(2), (1984) 239. 53

[99] F. W. Olver, D. W. Lozier, R. F. Boisvert, and C. W. Clark. *NIST handbook of mathematical functions hardback.* Cambridge university press (2010). 55

[100] M. Ilchen, N. Douguet, T. Mazza, A. J. Rafipoor, C. Callegari, P. Finetti, O. Plekan, K. C. Prince, A. Demidovich, C. Grazioli, L. Avaldi, P. Bolognesi, M. Coreno, M. Di Fraia, M. Devetta, Y. Ovcharenko, S. Düsterer, K. Ueda, K. Bartschat, A. N. Grum-Grzhimailo, A. V. Bozhevolnov, A. K. Kazansky, N. M. Kabachnik, and M. Meyer. *Circular Dichroism in Multiphoton Ionization of Resonantly Excited* He^+ *Ions.* Phys. Rev. Lett. **118**, (2017) 013002. 62

[101] Bouchiat, M. A., Poirier, M., and Bouchiat, C. *New possible manifestations of parity violation in forbidden magnetic transitions : chiral absorption of plane polarized light and circular dichroism in crossed transverse dc electric and magnetic fields.* J. Phys. France **40**(12), (1979) 1127. 62

[102] J. Guéna, D. Chauvat, P. Jacquier, E. Jahier, M. Lintz, S. Sanguinetti, A. Wasan, M. A. Bouchiat, A. V. Papoyan, and D. Sarkisyan. *New Manifestation of Atomic Parity Violation in Cesium: A Chiral Optical Gain Induced by Linearly Polarized* $6S-7S$ *Excitation.* Phys. Rev. Lett. **90**, (2003) 143001. 62

[103] E. J. Angstmann, T. H. Dinh, and V. V. Flambaum. *Parity nonconservation in atomic Zeeman transitions.* Phys. Rev. A **72**, (2005) 052108. 62

[104] A. Sargsyan, A. Tonoyan, G. Hakhumyan, C. Leroy, Y. Pashayan-Leroy, and D. Sarkisyan. *Atomic transitions of Rb, D2 line in strong magnetic fields: Hyperfine Paschen–Back regime D2 line in strong magnetic fields: Hyperfine Paschen–Back regime.* Opt. Commun. **334**, (2015) 208. 62, 70

[105] A. Sargsyan, G. Hakhumyan, A. Papoyan, D. Sarkisyan, A. Atvars, and M. Auzinsh. *A novel approach to quantitative spectroscopy of atoms in a magnetic field and applications based on an atomic vapor cell with* $L = \lambda$. Appl. Phys. Lett. **93**(2), (2008) 021119. 68

[106] B. A. Olsen, B. Patton, Y.-Y. Jau, and W. Happer. *Optical pumping and spectroscopy of Cs vapor at high magnetic field.* Phys. Rev. A **84**, (2011) 063410. 70, 73, 78

[107] R. Müller and A. Weis. *Laser frequency stabilization using selective reflection spectroscopy.* Appl. Phys. B **66**(3), (1998) 323. 72

[108] D. Das and V. Natarajan. *High-precision measurement of hyperfine structure in the D lines of alkali atoms.* J. Phys. B: At. Mol. Opt. Phys. **41**(3), (2008) 035001. 72

[109] R. K. Hanley, P. D. Gregory, I. G. Hughes, and S. L. Cornish. *Absolute absorption on the potassium D lines: theory and experiment.* J. Phys. B: At. Mol. Opt. Phys. **48**(19), (2015) 195004. 72

[110] J. S. Guzman, A. Wojciechowski, J. E. Stalnaker, K. Tsigutkin, V. V. Yashchuk, and D. Budker. *Nonlinear magneto-optical rotation and Zeeman and hyperfine relaxation of potassium atoms in a paraffin-coated cell.* Phys. Rev. A **74**, (2006) 053415. 72

[111] K. Pahwa, L. Mudarikwa, and J. Goldwin. *Polarization spectroscopy and magnetically-induced dichroism of the potassium D2 lines.* Opt. Express **20**(16), (2012) 17456. 72

[112] A. Lampis, R. Culver, B. Megyeri, and J. Goldwin. *Coherent control of group index and magneto-optical anisotropy in a multilevel atomic vapor.* Opt. Express **24**(14), (2016) 15494. 72

[113] A. Sargsyan, A. Amiryan, C. Leroy, T. A. Vartanyan, and D. Sarkisyan. *The effect of electromagnetically induced transparency in a potassium nanocell.* Opt. Spectrosc. **123**(1), (2017) 139. 73

[114] B. Zlatković, A. J. Krmpot, N. Šibalić, M. Radonjić, and B. M. Jelenković. *Efficient parametric non-degenerate four-wave mixing in hot potassium vapor*. Laser Phys. Lett. **13**(1), (2015) 015205. 73

[115] S. D. Harrell, C.-Y. She, T. Yuan, D. A. Krueger, H. Chen, S. S. Chen, and Z. L. Hu. *Sodium and potassium vapor Faraday filters revisited: theory and applications*. J. Opt. Soc. Am. B **26**(4), (2009) 659. 73

[116] C. D'Errico, M. Zaccanti, M. Fattori, G. Roati, M. Inguscio, G. Modugno, and A. Simoni. *Feshbach resonances in ultracold* ^{39}K. New J. Phys. **9**(7), (2007) 223. 73

[117] A. Sargsyan, G. Hakhumyan, C. Leroy, Y. Pashayan-Leroy, A. Papoyan, and D. Sarkisyan. *Hyperfine Paschen-Back regime realized in Rb nanocell*. Opt. Lett. **37**(8), (2012) 1379. 73

[118] M. A. Zentile, J. Keaveney, L. Weller, D. J. Whiting, C. S. Adams, and I. G. Hughes. *ElecSus: A program to calculate the electric susceptibility of an atomic ensemble*. Comp. Phys. Commun. **189**, (2015) 162. 73

[119] A. Sargsyan, A. Tonoyan, G. Hakhumyan, C. Leroy, Y. Pashayan-Leroy, and D. Sarkisyan. *Complete hyperfine Paschen-Back regime at relatively small magnetic fields realized in potassium nano-cell*. Eur. Phys. Lett. **110**(2), (2015) 23001. 73, 75

[120] J. A. Zielińska, F. A. Beduini, N. Godbout, and M. W. Mitchell. *Ultranarrow Faraday rotation filter at the Rb D1 line*. Opt. Lett. **37**(4), (2012) 524. 76

[121] N. Bendali, H. T. Duong, and J. L. Vialle. *High-resolution laser spectroscopy on the D1 and D2 lines of* $^{39,\ 40,\ 41}K$ *using RF modulated laser light*. J. Phys. B: At. Mol. Opt. Phys. **14**(22), (1981) 4231. 78

[122] A. Sargsyan, A. Tonoyan, G. Hakhumyan, A. Papoyan, E. Mariotti, and D. Sarkisyan. *Giant modification of atomic transition probabilities induced by a magnetic field: forbidden transitions become predominant*. Laser Physics Letters **11**(5), (2014) 055701. 78

[123] D. Budker, W. Gawlik, D. F. Kimball, S. M. Rochester, V. V. Yashchuk, and A. Weis. *Resonant nonlinear magneto-optical effects in atoms*. Rev. Mod. Phys. **74**, (2002) 1153. 80

[124] D. Budker and M. Romalis. *Optical magnetometry*. Nat. Phys. **3**, (2007) 227. 80

[125] G. Bison, N. Castagna, A. Hofer, P. Knowles, J.-L. Schenker, M. Kasprzak, H. Saudan, and A. Weis. *A room temperature 19-channel magnetic field mapping device for cardiac signals*. Appl. Phys. Lett. **95**(17), (2009) 173701. 80

[126] S. Taue, Y. Sugihara, T. Kobayashi, S. Ichihara, K. Ishikawa, and N. Mizutani. *Development of a Highly Sensitive Optically Pumped Atomic Magnetometer for Biomagnetic Field Measurements: A Phantom Study*. IEEE Trans. Magn. **46**(9), (2010) 3635. 80

[127] A. Sheinker, L. Frumkis, B. Ginzburg, N. Salomonski, and B. Kaplan. *Magnetic Anomaly Detection Using a Three-Axis Magnetometer*. IEEE Trans. Magn. **45**(1), (2009) 160. 80

[128] I. Bolshakova, I. Duran, R. Holyaka, E. Hristoforou, and A. Marusenkov. *Performance of Hall Sensor-Based Devices for Magnetic Field Diagnosis at Fusion Reactors*. Sens. Lett. **5**(1), (2007) 283. 80

[129] L. Weller, T. Dalton, P. Siddons, C. S. Adams, and I. G. Hughes. *Measuring the Stokes parameters for light transmitted by a high-density rubidium vapour in large magnetic fields*. J. Phys. B: At. Mol. Opt. Phys. **45**(5), (2012) 055001. 82, 94

[130] Q. Peng, S. McMurry, and J. Coey. *Axial magnetic field produced by axially and radially magnetized permanent rings*. J. Magn. Magn. Mater. **268**(1), (2004) 165. 89

[131] A. Sargsyan, A. Amiryan, S. Cartaleva, and D. Sarkisyan. *Nanocell with a pressure-controlled Rb atomic vapor column thickness: Critical influence of the thickness on optical processes*. J. Exper. Theor. Phys. **125**(1), (2017) 43. 91

[132] G.-W. Truong, J. D. Anstie, E. F. May, T. M. Stace, and A. N. Luiten. *Absolute absorption line-shape measurements at the shot-noise limit*. Phys. Rev. A **86**, (2012) 030501. 92

[133] A. Papoyan, S. Shmavonyan, A. Khanbekyan, K. Khanbekyan, C. Marinelli, and E. Mariotti. *Magnetic-field-compensation optical vector magnetometer*. Appl. Opt. **55**(4), (2016) 892. 92

[134] R. Folman, P. Kruger, J. Schmiedmayer, J. Denschlag, and C. Henkel. *Microscopic atom optics: from wires to an atom chip*. arXiv:0805.2613 (arXiv preprint), (2008) 1. 93

[135] J. Keaveney, F. S. Ponciano-Ojeda, S. M. Rieche, M. J. Raine, D. P. Hampshire, and I. G. Hughes. *Quantitative optical spectroscopy of 87Rb vapour in the Voigt geometry in DC magnetic fields up to 0.4 T*. J. Phys. B: At. Mol. Opt. Phys. **52**(5), (2019) 055003. 94

[136] M. T. Hummon, S. Kang, D. G. Bopp, Q. Li, D. A. Westly, S. Kim, C. Fredrick, S. A. Diddams, K. Srinivasan, V. Aksyuk, and J. E. Kitching. *Photonic chip for laser stabilization to an atomic vapor with* 10^{-11} *instability*. Optica **5**(4), (2018) 443. 94

[137] T. Peyrot, C. Beurthe, S. Coumar, M. Roulliay, K. Perronet, P. Bonnay, C. S. Adams, A. Browaeys, and Y. R. P. Sortais. *Fabrication and characterization of super-polished wedged borosilicate nano-cells*. Opt. Lett. **44**(8), (2019) 1940. 94

[138] C. Aslangul. *Mécanique quantique 2: Développements et application à basse énergie*. De Boeck Supérieur (2008). 100

[139] C. Cohen-Tannoudji, J. Dupont-Roc, and G. Grynberg. *Atom-photon interactions: basic processes and applications*. Wiley-VCH (1998). 101

[140] A. Messiah. *Quantum mechanics, volume II*. North-Holland Publishing Company, Amsterdam, 1969 (1962). 106, 107

[141] R. N. Zare. *Angular momentum: understanding spatial aspects in chemistry and physics*. Wiley-Interscience (1988). 106, 107

[142] A. Edmonds. *Angular momentum in quantum theory*. Princeton: Princeton University Press (1960). 107

[143] R. D. Cowan. *The theory of atomic structure and spectra*. 3rd Edition. Univ of California Press (1981). 107, 108

Selective Reflection Spectroscopy of Alkali Vapors Confined in Nanocells and Emerging Sensing Applications

Abstract

This thesis is aimed at studying the resonant interaction of a laser radiation with an atomic alkali vapor layer of wavelength-scale thickness confined in an optical nanocell; and emerging sensing applications.

We focus our attention on the selective reflection arising at the interface between a dielectric window and a resonant alkali vapor, and show that the derivative of selective reflection spectra exhibit narrow resonances whose maxima are located exactly at atomic resonance frequencies. These resonances are observed with a spectral linewidth up to fifteen times smaller than the Doppler linewidth of the medium and their amplitudes scale linearly with respect to the transitions ones. Owing to these properties and the possibility to probe thin atomic layers, we investigate atom-surface interaction and measure the C_3 coefficient of the van der Waals interaction.

We present a theoretical model describing the interaction of near-resonant laser light with alkali vapor-filled nanocell in the presence of an external static magnetic field. We show an excellent agreement between recorded and calculated spectra in a wide range of magnetic fields spanning from Zeeman to Paschen-Back regimes. Following these results, we propose a concept for a nanocell-based optical magnetometer. A proof of feasibility is presented and a performance analysis reveals a coefficient of variation for the magnetic field measurements less than 5% in the range 0.4 – 2 kG.

Keywords: *spectroscopy*; *nanocell*; *alkali vapor*; *magnetometry*; *selective reflection.*

Spectroscopie par Réflexion Sélective de Vapeurs Alcalines Confinées dans des Nanocellules et Applications de Détection Émergentes

Résumé

Cette thèse vise à étudier l'interaction résonante d'un rayonnement laser avec une couche mince d'épaisseur sub-longueur d'onde de vapeur alcaline atomique confinée en nanocellule ; et les applications de détection qui en émergent.

Nous nous concentrons sur la réflexion sélective se produisant à l'interface entre une fenêtre diélectrique et une vapeur résonante, et montrons que la dérivée des spectres de réflexion sélective est composée de résonances étroites dont les maxima correspondent aux positions des transitions atomiques. Ces résonances sont observées avec une largeur spectrale jusqu'à quinze fois plus fine que la largeur Doppler du milieu, et leurs amplitudes évoluent de façon linéaire avec celles des transitions. Grâce à ces propriétés et aux faibles épaisseurs de cellule pouvant être sondées, nous examinons les interactions atome-surface et mesurons le coefficient C_3 de l'interaction de van der Waals.

Nous présentons un modèle théorique décrivant l'interaction entre lumière quasi-résonante et nanocellule remplie d'une vapeur alcaline sous champ magnétique statique. Ce modèle se montre en excellent accord avec les résultats expérimentaux pour une large gamme de champs magnétiques depuis le régime Zeeman jusqu'au régime Paschen-Back. Au vu de ces résultats, nous proposons un concept de magnétomètre optique basé sur les nanocellules. Une preuve de faisabilité est présentée et une analyse en performance révèle un coefficient de variation des mesures de champs magnétiques inférieur à 5 % dans la gamme 0,4 – 2 kG.

Mots clefs : *spectroscopie*; *nanocellule*; *vapeurs alcalines*; *magnétométrie*; *réflexion sélective.*